
# THE UNIVERSITY OF BIRMINGHAM

## FLOW PATTERNS AND ENERGY DISSIPATION RATES IN BATCH ROTOR-STATOR MIXERS

By

**Adi Tjipto Utomo**

A thesis submitted to
The School of Engineering of
The University of Birmingham
for the degree of

**Doctor of Philosophy**

School of Engineering
Chemical Engineering
The University of Birmingham
Edgbaston
Birmingham B15 2TT
United Kingdom

**June 2009**

# ABSTRACT

The flow pattern and distribution of energy dissipation rate in a batch rotor-stator mixer fitted with disintegrating head have been numerically investigated. Standard k-ε turbulence model in conjunction with sliding mesh method was employed and the simulation results were verified by laser Doppler anemometry (LDA) measurements. The agreement between predicted and measured velocity profiles in the bulk and of jet emerging from stator hole was very good. Results showed that the interaction between stator and rotating blades generated periodic fluctuations of jet velocity, flowrate, torque and energy dissipation rate around the holes. The kinetic energy balance based on measured velocity distribution indicated that about 70% of energy supplied by the rotor was dissipated in close proximity to the mixing head, while the simulation predicted that about 60% of energy dissipated in the same control volume. Both simulations and measurements showed that jet velocity and total flowrate through holes were proportional to rotor speed, while the energy dissipation rate scaled with the cube of rotor speed.

The effect of stator geometry on the flow pattern and energy dissipation rate was also numerically investigated using standard k-ε model and sliding mesh method. The simulations showed that flow patterns in the holes were similar regardless of holes sizes and shapes, i.e. jets emerged in the proximity of the leading edge and they induced circulation flows behind them. The radial velocities

of jets emerging from various stators plotted against normalized tangential coordinate were practically the same, however, jets tangential velocities were affected by hole width-to-depth ratio. Jets emerging from holes with large width-to-depth ratio had negative tangential velocity component (the same as rotor rotation) while those from holes with small width-to-depth ratio had positive tangential velocity component (against rotor rotation). Jets emerging from stators with small hole spacing tended to merge and move tangentially, while those emerging from stators with large hole spacing tended to move radially as free jets. The power number correlated well with the total flowrate and the total flowrate correlated well with the total hole area. Both power number and flowrate were practically not affected by hole shape, hole spacing and stator thickness. For all stators investigated, high energy dissipation rate occurred in the regions around the leading and trailing edges due to stagnations in those regions. Stators with narrow holes generated more uniform energy dissipation rate profile around the holes than those with wide holes since the regions with high energy dissipation rate around the leading and trailing edges merged. The simulations also predicted that about 50 – 60% of total energy supplied by rotor was dissipated in the rotor swept volume regardless of stator geometries.

# ACKNOWLEDGEMENT

First of all, I would like to thank my supervisor, Prof. Dr. Andrzej W. Pacek, who has given invaluable suggestions, comments and consistent encouragement throughout this research. I would also like to thank him for his exceptional support and guidance during the writing of this thesis.

I would also like to thank Dr. Michael Baker from Unilever R&D Port Sunlight for his comments and invaluable information during this research.

I would also like to thank Unilever, Overseas Research Students Awards Scheme (ORSAS) and The Department of Chemical Engineering, University of Birmingham for their financial support which made it possible for me to undertake this study.

I would also like to thank to BlueBEAR who provided resources and facilities to perform computational work in this study and to Lynn Draper and Tom Eddleston (Chemical Engineering Department), Peter Hinton and Robert Sharpe (Workshop) and all my friends and colleagues for their helps and supports.

And finally, I would like to thank my family for their moral support, encouragement and understanding throughout this study.

# TABLE OF CONTENT

**CHAPTER IV**

**FLOW PATTERN, PERIODICITY AND ENERGY DISSIPATION IN A BATCH ROTOR-STATOR MIXER**



**CHAPTER V**

**THE EFFECT OF STATOR GEOMETRY ON THE FLOW PATTERN AND ENERGY DISSIPATION RATE IN A ROTOR-STATOR MIXER**



**CHAPTER VI**

**THE EFFECTS OF HOLE SPACING AND STATOR THICKNESS ON THE FLOW PATTERN AND ENERGY DISSIPATION RATE IN A BATCH ROTOR-STATOR MIXER**

# LIST OF FIGURES

## CHAPTER I



## CHAPTER III



## CHAPTER IV

## CHAPTER V

## CHAPTER VI

# LIST OF TABLES

# CHAPTER I

# INTRODUCTION AND LITERATURE REVIEW

## *1.1. Rotor-stator mixers*

Rotor-stator mixers are characterized by high speed rotors surrounded closely by stators. The rotors rotate at an order of magnitude higher speed than impellers in stirred tank with typical tip speeds range from 10 to 50 m/s (Atiemo-Obeng and Calabrese, 2004) while the gaps between the rotors and stators vary from 100 to 3000 μm (Karbstein and Schubert, 1995). They can generate high shear rate in the gap ranging from 20,000 to 100,000 $s^{-1}$ (Atiemo-Obeng and Calabrese, 2004) and therefore they are usually called high shear mixers. Rotor-stator mixers also generate high intensity of turbulence. High kinetic energy supplied by the rotor dissipates mainly inside the stator and therefore the local energy dissipation rate in a rotor-stator mixer can be three orders of magnitude higher than in a conventional stirred vessel (Atiemo-Obeng and Calabrese, 2004).

The assembly of the rotor and stator is often called the mixing head, working head or generator, but the stator itself is often called the head. There are various designs of rotor-stator mixers from different vendors (Silverson (www.silverson.com), Ross (www.highshearmixers.com), Ystral (www.ystral.de), Chemineer (www.chemineer.com), IKA Works (www.ikausa.com), Rayneri (www.vmi.fr), Siefer (www.siefer-trigonal.de), etc), however, according to

Atiemo-Obeng and Calabrese (2004), they can be classified into colloid mills (*Fig. 1.1(a)*) and toothed devices (*Fig. 1.1(b)* and *(c)*), axial discharge rotor-stator mixers where the rotors are axial impellers (*Fig. 1.2*) and radial discharge rotor-stator mixers where the rotors are radial impellers (*Fig. 1.3* and *Fig. 1.4*). Colloid mills usually operate as in-line mixers with external pumps due to their limited pumping ability while axial and radial discharge rotor-stator mixers can operate as batch or in-line mixers (*Fig. 1.5*) since they have a considerably pumping ability although significantly lower than open impellers (Myers et al., 1999).

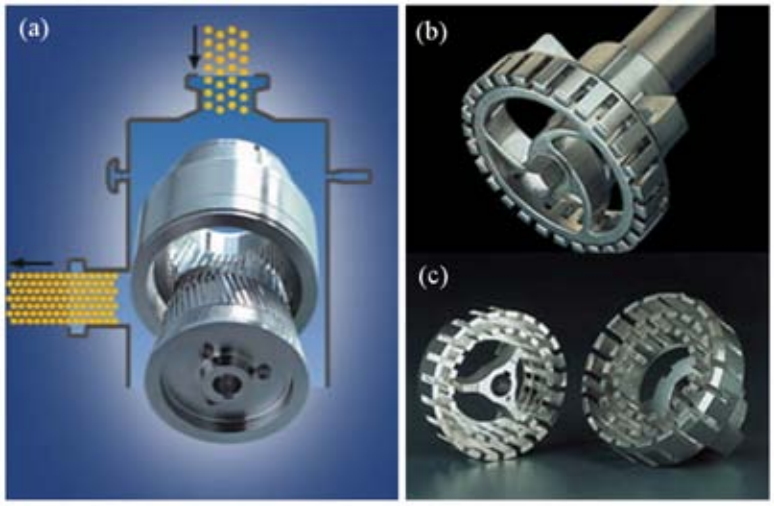


***Fig. 1.1.*** *(a) Colloid mill with grooved rotor and stator, (b) toothed device, (c) multi-stage toothed device (from www.ikausa.com/mk.htm and www.ikausa.com/highshear.htm).*

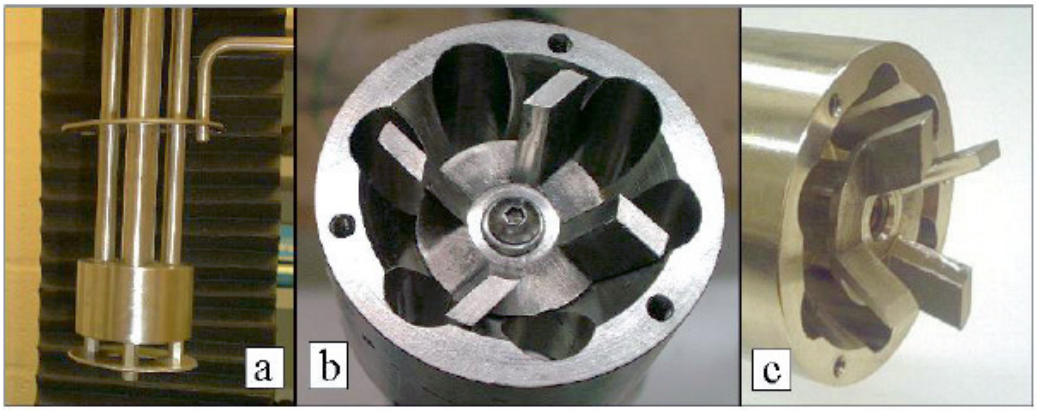


***Fig. 1.2.*** *Axial discharge rotor-stator mixer Greerco XLR Homomixer, (a) mixing head, (b) bottom view of the mixing head and (c) rotor poping out of stator (from Padron, 2001).*

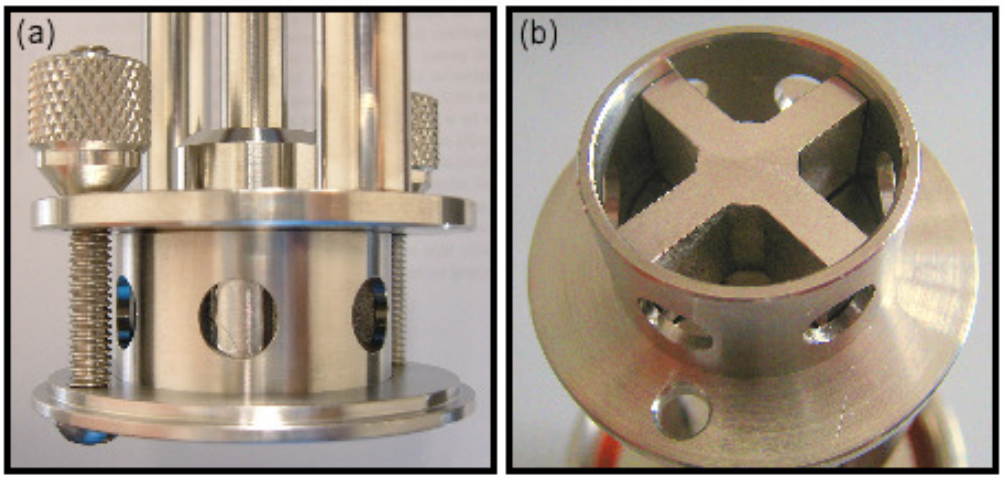


***Fig. 1.3.*** *Radial discharge rotor-stator mixer Silverson L4RT, (a) mixing head fitted with disintegrating head and (b) bottom view of the mixing head.*

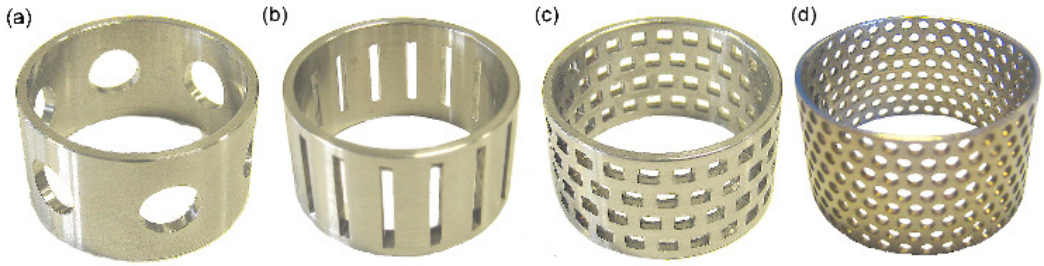


***Fig. 1.4.*** *Silverson stators (a) disintegrating head, (b) slotted head, (c) square hole head and (d) standard emulsor screen.*

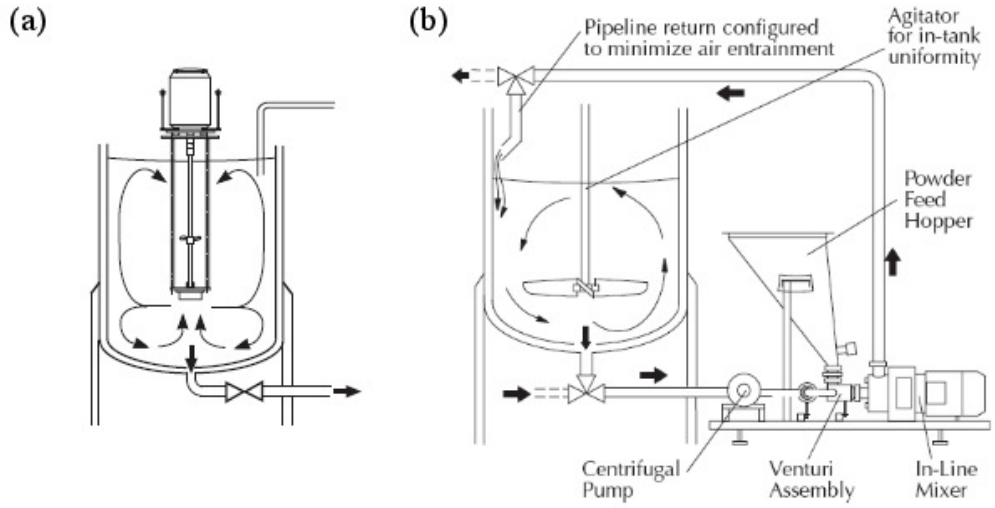


***Fig. 1.5.*** *(a) Batch and (b) in-line rotor-stator mixers (from www.silverson.com).*

Batch rotor-stator mixers can handle up to 30 $m^3$ low viscosity fluid like water, while in-line rotor-stator mixers can deliver up to 200 $m^3$/hr low viscosity fluid (www.silverson.com). They can be used to handle liquid with viscosity up to 100 Pa.s although the handling capacity is greatly reduced. When mixing viscous fluid, additional impeller such as anchor or helical ribbon impeller should be used in batch system to enhance bulk mixing, while in the in-line system, external pump could be used.

There are advantages and disadvantages of each operation mode. Batch mixer only requires simple control system, but spatial homogeneity may be an issue in a large vessel which could lead to a longer processing time. In-line mixer can provide more uniform shear and turbulent intensity to the processed materials which require only a single pass. However, usually the materials require several passes to achieve product specification. In this case, a tank with a close loop pump (*Fig. 1.5*) are required to circulate the processed materials which will require higher capital cost and a more sophisticated control system since both flowrate and rotor speed need to be controlled.

Typical industrial rotor-stator mixer has diameter around 0.1 m, operates at 3550 rpm (motor speed), transmits only 200 Nm of torque and therefore requires no gear box, while typical industrial impeller has diameter of over 1 m, operates below 100 rpm and tranmit up to 85,000 Nm of torque and require a gear box which must be capable of transmitting substantial amount of torque (Myers et al., 1999). Therefore, by operating at high speed, rotor-stator mixer can reduce processing time and capital investment (e.g. smaller tank, no gear box)

significantly. In term of energy consumption, rotor-stator mixers require high power input but operate at much shorter time while stirred vessel require low power input but operate at much longer time and therefore the power consumption could be about the same. However, they are not intended to replace conventional stirred vessel but processes which require high shear and high energy dissipation rate can be handled better by rotor-stator mixers.

Rotor-stator mixers have been used extensively to accomplish the most-demanding mixing tasks in food, cosmetics, chemicals and pharmaceuticals industries. Mostly they have been used to make emulsions or dispersions, but they are also used for blending liquids with high viscosity ratio, solubilizing solid and polymeric gum, cell disruption, deagglomeration, etc. (Myers et al., 1999, Atiemo-Obeng and Calabrese, 2004). Some typical applications of rotor-stator mixer in the production of consumer products are shown in *Table 1.1*. Some other applications of rotor-stator mixer are:

- Incorporation of SEBS (styrene-ethylene-butylene-styrene) copolymer into asphalt up to 25% by weight to increase its flexibility and durability. SEBS is solid or semi-solid at ambient temperature and melts at 65 – 260$^{o}$C. The mixing is accomplished using Siefer trigonal mill (*Fig. 1.6*) operated at 3000-4600 rpm. The process is carried out at 150-200 $^{o}$C and the troughput is about 100 gal/min. This process is essentially blending of two viscous fluids. The modified asphalt has viscosity of 50 – 350 cP at 200$^{o}$C (Fields, 1999).

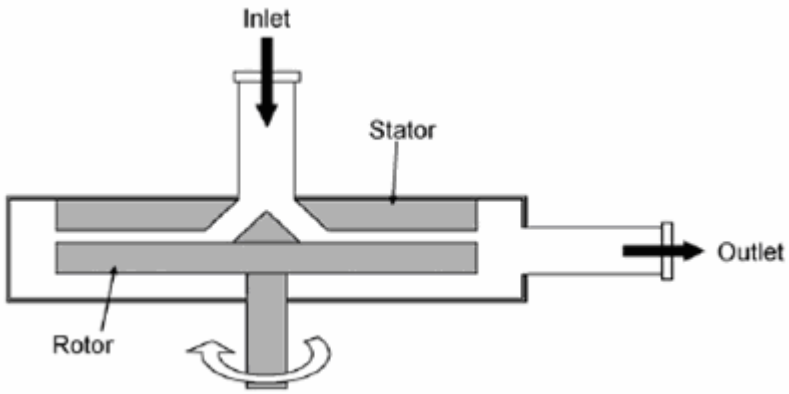


***Fig. 1.6.*** *Siefer trigonal mill. The diameter of the rotor and stator is 220 mm and the gap width is 0.1 mm (from Kowalski, 2009).*

- Deagglomeration of nanopowder

  The authors (see Pacek et al., 2007b) and Xie et al. (2007) used batch rotor-stator mixers (Silverson L4RT (*Fig. 1.3*) and Ultra Turrax T25 (*Fig. 1.1(b)*) respectively) to produce sub-micron aggregate of silica nanopowder (Aerosil 200V) suspended in water. They found that de-agglomeration occurred through the erosion of large agglomerates producing small size aggregates.

- Pigment dispersion for inks and paints

  The break up and attrition of the pigment aggregates occur due to impact against stator wall and against each other. Because the disintegration of large particles occurs due to impingement rather than shear, the formulation can be prepared by using low viscosity vehicles to enhance the penetration and melting properties of such vehicles. The vehicle solids can be added after the dispersion is complete to achieve its stabilization (Loebert and Sharangpani, 2000).

***Table 1.1.*** *Applications of rotor-stator mixers in the production of consumer products (internal communication)*

| Phases | Duty | Examples |
|---|---|---|
| Single phase | Accelerate dissolution | Dilution of sodium lauryl-ether-sulphate (SLES-70, a viscous liquid – lamellar phase) in water to make thin isotropic (say 25%) solution (spherical micelles) for shampoos and shower gels. |
| Liquid-liquid | Emulsifications | Creams and lotions, component in other products e.g. antiperspirant emulsion roll-ons, shower gels, hair conditioners, mayonnaise, ice cream, emulsion polymerization |
| | Surfactant mesophase | Lamellar phase dispersions behave in a similar manner to emulsions with droplet/particle size being a key parameter in controlling dispersion properties (including rheology), e.g. fabric conditioners, antiperspirant emulsion roll-ons, hair conditioners, body-washes. |
| Liquid-solid | Thickening polymer dispersion | Carbopol, Xanthan gum, sodium CMC thickening of shampoos, shower gels, toothpastes, dish-wash liquids. Starch and thickeners for low fat products. Rotor-stator used to achieve effective dispersion without limps (“fish-eyes”) |
| | Dispersion of thickening clay | Similar to above but inorganic thickening clays, e.g. laponite, bentone, can be use as per above but also in non-aqueous products e,g, antiperspirant aerosols as re-suspension aids |
| | Powder wetting | Calcite and silica in toothpastes (calcite always white paste, silica can be white or clear). |
| Liquid - gas | Creating foams / aerated products | Aerated shower gels with air bubbles for visual appearance. |

In the rotor-stator mixers, droplets can be disrupted by laminar shears, turbulent eddies, mechanical impact on the stator surfaces or combination of those factors (Myers et al., 1999). The laminar shears in the rotor-stator mixers can be divided into (Myers et al., 1999):

- Planar/simple shear which occurs when the velocity changes with respect to direction normal to the direction of flow. Very high planar shear is generated in the narrow gap between the rotor and stator, however, this type of shear is only effective to break droplets when the viscosity ratio between the dispersed and continuous phases is less than 4 (Walstra,

1993). Droplets with higher viscosity ratio tend to rotate in the planar shear rather than be broken up.

- Elongational shear which occurs when the fluid velocity changes with respect to the direction of flow. It occurs when the fluid is accelerated rapidly. It is more effective to break droplets and able to break droplets with high viscosity ratio. Although elongational shear is present in rotor-stator devices, it is difficult to estimate its magnitude.

In colloid mill, droplets are disrupted by laminar shear forces when the surfaces of rotor and stators are smooth but by turbulence when the surfaces are roughened or toothed (Schubert, 1997). In a radial discharge rotor-stator mixer, Calabrese et al. (2002) showed that slotted stator with enlarged gap ($\delta$ = 1 mm) produced smaller mean drop sizes in the turbulent flow regime than that with standard gap ($\delta$ = 0.5 mm). Therefore they concluded that shear in the gap was not the predominant droplets breakage mechanism in the rotor-stator mixer in the turbulence regime. They also suggested that in the turbulent regime droplets disrupted by impingement on the stator surfaces and turbulent eddies in the jets emanating from stator slots.

The energy dissipation rate in the rotor-stator dispersing volume was higher than those in the static mixers and stirred vessels but lower than those in the high pressure valve homogenizers and ultrasound devices (*Fig. 1.7*), consequently the droplets produced in the rotor-stator mixers are smaller than those produced in the static mixers and stirred vessels but larger than those produced in the high pressure valve homogenizer and ultrasound devices. The

droplets produced in the rotor-stator mixers typically range from 0.5 – 100 μm (Atiemo-Obeng and Calabrese, 2004).

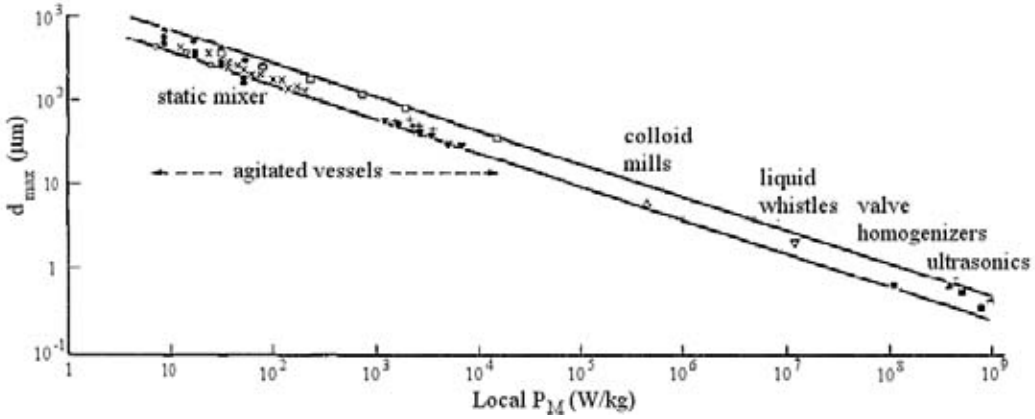


***Fig. 1.7.*** *Correlation between maximum drop size and local energy dissipation rate from various dispersing devices (from Davies, 1987).*

Although rotor-stator mixers have several advantages over stirred vessels or static mixers and have been used extensively in industries, there is very limited information available in the public domain. Some literature about rotor-stator mixer is summarized below.

## *1.2. Literature Review*

Most of literature about rotor-stator mixers is based on experimental works where the power draw in the rotor-stator mixers was investigated, either as batch mixers or in-line mixers. Some CFD simulations have also been carried out to investigate the details of the flow in the proximity of the mixing head and also in the bulk of the vessel.

### 1.2.1 Experimental works

The power draw in radial discharge rotor-stator mixers was studied by Padron (2001) and Doucet et al. (2005). Padron (2001) correlated the power number with different definitions of the Reynolds numbers based on various characteristic length available in the rotor-stator mixer, i.e. rotor diameter, gap width and total hydraulic radius of stator holes. He suggested that the definitions of the power and Reynolds numbers based on rotor diameter, hence the same as those in stirred vessel, can be used satisfactorily to describe the power draw in a batch rotor-stator. The power number in a batch rotor-stator mixer is similar to that in the stirred tank, i.e. it is inversely proportional to the Reynolds number in the laminar regime and relatively constant in the turbulent regime. The fully turbulent regime starts at *Re* above 10,000, however, the laminar regime extend up to *Re* = 100 instead of *Re* = 10 for the stirred tank (Padron, 2001; Doucet et al., 2005).

Padron (2001) found that the turbulent power draw scaled with the rotor speed to an exponent ranged from 2.84 to 3.45 depending on stator geometry. However, Bourne and Studer (1992) argued that the energy dissipation rate in the rotor-stator mixer approximately scaled with $N^{2.5}$ calculated from micromixing model. Padron (2001) found that the turbulent power numbers for Ross ME 100 LC varied from 2.4 for slotted head with 80 mesh screen to 3 for standard slotted head, while those for Silverson L4RT (*Fig. 1.3*) varied from 1.7 for disintegrating head to 2.3 for square hole head. Padron (2001) also suggested that energy dissipation was controlled by fluid impingement on stator slot surfaces or

turbulence in the jets emanating from stator slots. Doucet et al. (2005) found that the turbulent power number for VMI Rayneri turbotest was equal to 3 and observed the formation of cavern around the mixing head with either viscous Newtonian or non-Newtonian liquid.

Myers et al (2001) investigated the power draw in an axial discharge rotor-stator mixer (Greerco 1.5 HR, Chemineer) which can be operated in up-pumping or down-pumping mode. It generates axial flow when operated in up-pumping mode but it generates radial flow when operated in down-pumping mode due to the presence of bottom plate below the mixing head which divert axial flow into radial one. They found similar power curve to the one in the stirred tank when the power number was multiplied by $Fr^{0.1}$ where $Fr$ is the Froude number. The turbulent power number for up-pumping mode was about 2 and about 40% higher for down-pumping mode.

The power draw in in-line rotor-stator mixers has also been studied. Cooke et al. (2008) investigated the power draw in Silverson 150/250 MS which had double rotors and double stators (*Fig. 1.8*), while Kowalski (2009) investigated the power draw in Siefer trigonal mill (*Fig. 1.6*). They proposed that the power draw in an in-line rotor-stator mixer is a sum of

$$P = P_T + P_F + P_L = Po\rho N^3 D^5 + k_1 M N^2 D^2 + P_L \qquad \textbf{1-1}$$

where $P_T$ is the power due to the torque on the motor shaft to overcome fluid friction in the absence of any flow, $P_F$ is the power required to pump the liquid, $M$ is the mass flowrate and $P_L$ is the power loss.

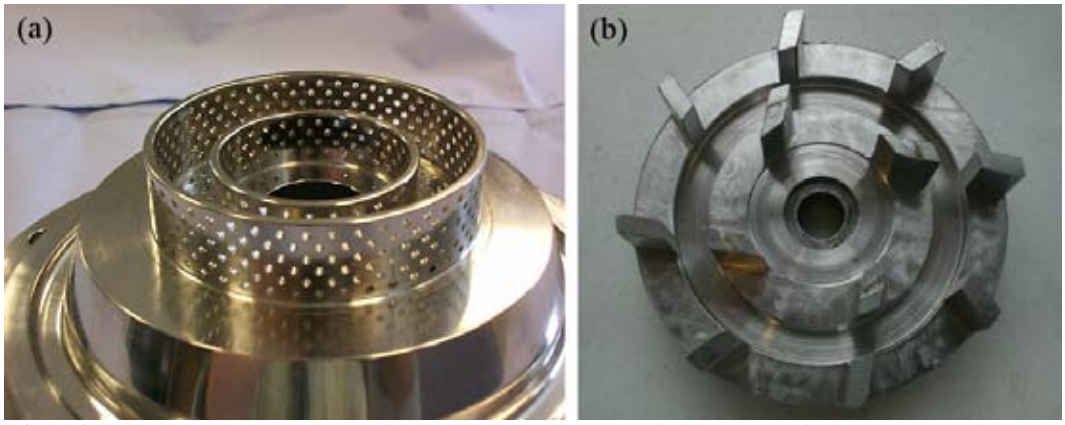


***Fig. 1.8.*** *Silverson 150/250 MS in-line mixer, (a) stators and (b) rotors. The outer rotors diameter are 38.2 mm and 63.4 mm. The diameter of stator holes is 1.59 mm (Adam Kowalski, private communication).*

For Silverson 150/250 MS in-line mixer, Cooke et al. (2008) found that flowrate was proportional to the rotor speed when the exit valve was fully open and power was a linear function of flowrate. The experiments were carried out at 3,000 – 12,000 rpm with rotor outer diameter as the characteristic length of the Reynolds and power numbers. The power draw was calculated from the measurement of torque on the shaft and from thermal energy. The values of *Po* and $k_1$ in *eq. 1-1* from both methods ranged from 0.2 – 0.24 and from 6.5 – 8.6 respectively (Cooke et al., 2008).

For Siefer trigonal mill, Kowalski (2009) defined *Re* as

$$Re = \rho N D \delta / \mu \qquad \textbf{1-2}$$

where $\delta$ is the gap width. According to this definition, the flow was laminar even at 4000 rpm and therefore the power number was defined as $k_0/Re$. The values of $k_0$ and $k_1$ in *eq. 1-1* were 0.15 and 48 respectively (Kowalski, 2009).

Khopkar et al. (2007) investigated the mixing time in a vessel stirred by a close clearance Paravisc impeller (Ekato, Germany) and a rotor-stator mixer

(VMI-Rayneri, France). The experiments were carried out in laminar flow in a 50 L vessel of diameter 0.4 m. The Paravisc impeller had a diameter of 0.374 m and was installed in the centre while the rotor-stator mixer (VMI-Rayneri) had a diameter of 0.09 m and was installed off-centre. They found that rotor-stator mixer could reduce the mixing time from about 400 s to about 100s when the rotor speed was increased from 0 to 750 rpm ($N_{paravisc}$ = 10 rpm). However, they suggested that Paravisc power draw should be larger than rotor-stator power draw to achieve the best mixing efficiency.

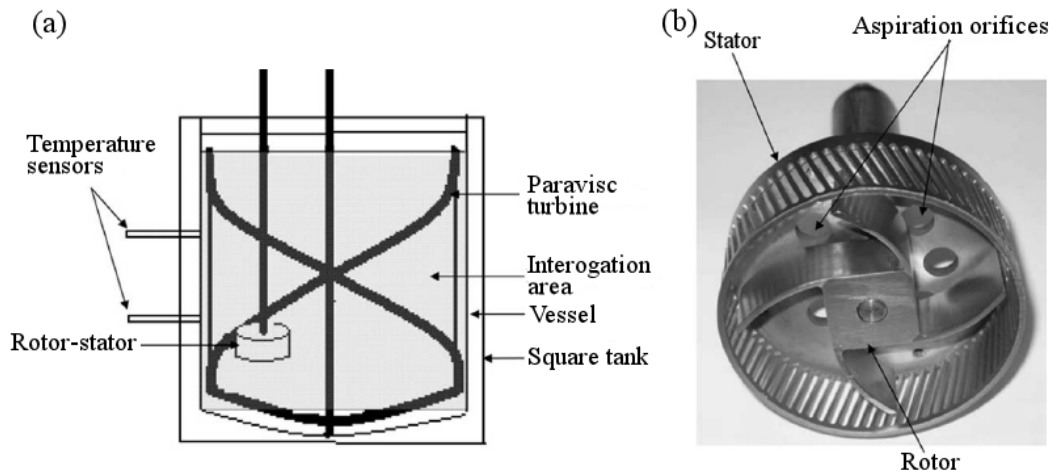


***Fig. 1.9.*** *(a) Experiment setup of Khopkar et al. (2007) and (b) rotor-stator mixer (VMI-Rayneri). The diameters of the tank and Paravisc turbine are 400 mm and 374 mm respectively. The diameter of the rotor is 90 mm and the gap width is 2 mm.*

### 1.2.2 CFD simulations

Calabrese et al. (2002) carried out 2D CFD simulations and LDA (Laser Doppler Anemometry) measurements of an in-line rotor-stator mixer (IKA Works). The outer rotor diameter was 154 mm and the gap width was 0.5 mm. The computational domain consisted of 322,000 computational cells with water as working fluid. The simulation was run in transient mode with standard k-ε

turbulence model for 15 rotor rotations and one time step corresponded to 1.07$^{o}$ of rotor movement. The rotor speed and flowrate were set to 30 rps and 2.86 L/s respectively.

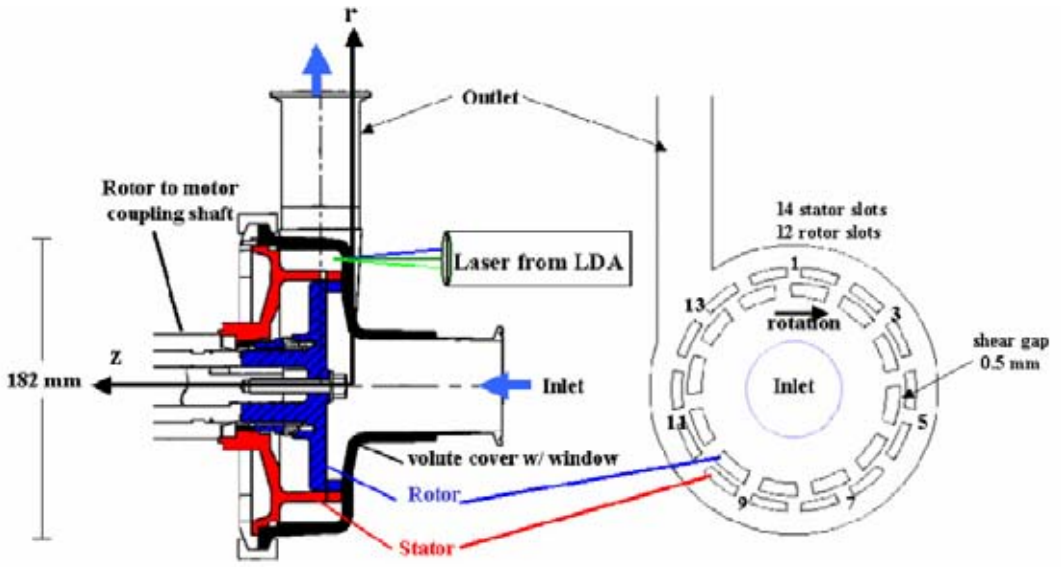


***Fig. 1.10.*** *Schematic diagram of IKA Work in-line rotor-stator mixer (from Calabrese et al., 2002).*

Both simulation and measurement showed that fluid was redirected radially as it impinges on the leading edge of the downstream stator tooth and each stator slot had a different circulation and re-entrainment pattern. However, the measurement showed a stronger jet and a more focus circulation flow than the simulation. The simulation also showed that the most intense turbulent kinetic energy (TKE), which provided a major energy field for emulsification and dispersion, occurred on the leading edge of downstream stator tooth when the stator slot was overlapped with the rotor tooth and flowrate began to fall. On the other hand, when the rotor and stator slots were aligned and flowrate was high, the TKE was low. Simulation carried out for enlarged gap, i.e. 4 mm instead of 0.5

mm for standard gap, showed that the TKE was much lower. Therefore they concluded that for emulsification or dispersion purposes it was necessary to have a narrow gap even if the shear in the gap was not a major contributor to the dispersion process.

Baldyga et al. (2007) carried out 2D CFD simulations to calculate the distributions of energy dissipation rate in a Silverson 150/250 MS in-line mixer (*Fig. 1.8*) and used the results to estimate the yield of second order competitive consecutive chemical reactions, i.e. diazo coupling between 1- and 2-naphtols and diazotized sulphanilic acid, using engulfment micromixing model. The CFD model was constructed with unstructured mesh consisted of 200,000 computational cells and the simulation was run with standard k-ε turbulence model and multiple reference frame model. The predictions of product distribution were compared with experimental data. The trend of variation of product distribution with changing the rotor speed and flowrate were well predicted, although the agreement was not very good. The CFD simulation also overpredicted the power number by as high as 50% at the lower flowrate, although the agreement was better at higher flowrate.

Baldyga et al. (2008) also employed 3D CFD simulation of Silverson 150/250 MS in-line mixer (*Fig. 1.8*) to calculate aggregate size distribution of silica nanoparticle. The rotor-stator mixer was fitted with disintegrating head for inner stator and square hole head for outer stator. The CFD model consisted of almost 4 million hexahedral cells and the simulation was run at various rotor speeds from 3,000 to 9,000 rpm. The momentum balance equation was solved

with standard k-ε model and multiple reference frames model. The aggregate size distribution was calculated using population balance equation with quadrature method of moments (QMOM) which was linked to the CFD code via user defined function. The CFD simulations predicted that the highest velocity occurred around the blades of outer rotor but the jets emerging from outer stator had very low velocity. The zone of high shear was localized in the region where both rotors operate and in jets emerging from the holes of disintegrating head. The energy dissipation rate could be as high as $10^5$ and $10^7$ $m^2/s^3$ at 3,000 and 9,000 rpm respectively. Unfortunately, the authors did not emphasise the details of hydrodynamics behavior in the rotor-stator mixer further. Furthermore, the details of transient flow due to periodic blade passing are lost when the multiple reference frame model is used to simulate rotor rotation. The agreement between calculated aggregate size distribution and experimental data was good at low rotor speed, but the discrepancy increased at higher rotor speed.

## *1.3. Objectives*

Although some works have been carried out to investigate the performance of the rotor-stator mixers, however, the information about rotor-stator mixers available in the public domain is still limited. A lot more work need to be carried out to understand the performance of this kind of mixer better considering that there are a lot of design variations in the market. In this study, the velocity profiles as well as energy dissipation rate in a batch rotor-stator mixer (Silverson L4RT) were investigated. There are two main objectives of this study as follows.

The first objective is to validate CFD predictions of flow pattern and distribution of energy in a batch rotor-stator mixer. Since most of interesting features in a rotor-stator mixer are concealed behind the stator, direct velocity measurement with LDA or PIV (Particle Image Velocimetry) is very difficult. Therefore, CFD was employed in this study to predict the flow patterns inside and around the mixing head as well as in the bulk region of the vessel. The results were verified by LDA measurements carried out in the close proximity of the mixing head and in the bulk region. The kinetic energy balance around the mixing head based on the measured velocity profiles was also carried out to calculate the amount of energy dissipated in the proximity of the mixing head. The result was then compared with CFD prediction.

The second objective is to investigate numerically the effect of stator geometry on the flow pattern and energy dissipation rate in a batch rotor-stator mixer. However, limited LDA measurement was also carried out to validate CFD simulations. Three standard stator geometries and some modified stators were simulated to investigate the effects of hole dimension, total hole area, stator thickness and hole spacing on the flow pattern, flowrate, torque, power number, energy dissipation rate profile and distribution of energy in a batch rotor-stator mixer.

## *1.4. Thesis outline and publications*

The layout of the thesis is as follows. The introduction, literature review and objectives were given in Chapter I. The basic theory of turbulence model used

in this work is given in Chapter II. Chapter III gives some overview of some flow measurement devices and explanation why LDA was selected for this work. Chapter IV discusses the velocity profile, effect of blade passing, energy dissipation rate and distribution of energy in a batch rotor-stator mixer fitted with disintegrating stator. The comparison between CFD prediction and LDA measurement will also be given in this chapter. Chapter V discusses the effect of stator geometry on the flow pattern and energy dissipation rate in a batch rotor-stator mixer fitted with standard stators supplied by Silverson. This work is extended in Chapter VI by using modifications of standard stator geometries to investigate the effects of hole shape, hole spacing, hole orientation and stator thickness on the flow pattern and energy dissipation rate. This thesis is finished with conclusions and recommended future works in Chapter VII.

Some supplementary information is also given in appendixes. Appendix A explains the techniques used to measure jet radial and tangential velocity profiles in disintegrating head. The control volume used to carry out mass and energy balances, discretization of its boundary and details mass and energy balances are also given in Appendix A. Appendix B compares the effects of turbulence models on the accuracy of CFD prediction. Two turbulence models are considered: the standard k-ε model and the more demanding anisotropic Reynolds stress model (RSM). Appendix C compares the predicted and measured jet radial velocity profiles and flowrates of slotted and square hole heads.

Parts of this work have been published and presented in international conferences as follows:

Published works:

- Utomo, A., Baker, M. and Pacek, A.W., 2008, "Flow pattern, periodicity and energy dissipation in a batch rotor-stator mixer". *Chem. Eng. Res. Des.*, **86**: 1397 – 1409.
- Utomo, A, Baker, M. and Pacek, A.W., 2009, "The effect of stator geometry on the flow pattern and energy dissipation rate in a rotor-stator mixer". *Chem. Eng. Res. Des.*, **87**: 533 – 542.

Presented works:

- Characterization of flow pattern in a rotor-stator mixer, presented as poster presentation in European Congress of Chemical Engineering (ECCE-6), Copenhagen, Denmark, 16 – 20 September 2007.
- Flow pattern, periodicity and energy dissipation in a batch rotor-stator mixer, presented as oral presentation in International Symposium on Mixing in Industrial Processes (ISMIP) VI, Niagara on the Lake, Canada, 17 – 21 August 2008.
- The effect of stator geometry on the flow pattern and energy dissipation rate in a rotor-stator mixer, presented as oral presentation in 13$^{th}$ European Conference on Mixing (ECM 13), London, UK, 14 – 17 April 2009.

# CHAPTER II

# COMPUTATIONAL FLUID DYNAMICS

## 2.1. Introduction

The flow of fluid, both laminar and turbulent, is governed by continuity and momentum balance equations. The continuity equation is basically the mass balance and can be written in Eulerian or stationary coordinate as (Versteg and Malalasekera, 1996)

$$\frac{\partial \rho}{\partial t} + \frac{\partial}{\partial x_i}(\rho u_i) = \frac{\partial \rho}{\partial t} + u_i \frac{\partial \rho}{\partial x_i} + \rho \frac{\partial u_i}{\partial x_i} = 0 \qquad \textbf{2-1}$$

where $\rho$ is the fluid density and $u_i$ is the instantaneous fluid velocity in $x_i$ direction. For incompressible fluid, *eq. 2-1* becomes

$$\frac{\partial u_i}{\partial x_i} = 0 \qquad \textbf{2-2}$$

The momentum balance is the Newton's second law of motion which states that the rate of change of momentum in a control volume is equal to the sum of all forces acting on the control volume (Versteg and Malalasekera, 1996). In the absence of body forces such as gravity, centrifugal, Coriolis and electromagnetic forces, the momentum balance can be written in Lagrangian or moving coordinate as (Davidson, 2004)

$$\frac{D(\rho \mathbf{u})}{Dt} = -\frac{\partial p}{\partial x_i} + \frac{\partial \tau_{ji}}{\partial x_j} \qquad \textbf{2-3}$$

where $\frac{D(\rho \mathbf{u})}{Dt}$ is the acceleration of the fluid in the control volume, $\frac{\partial p}{\partial x_i}$ is the normal stress due to pressure difference and $\frac{\partial \tau_{ji}}{\partial x_j}$ is the shear stress due to viscous forces. $\tau_{ij}$ indicates shear stress component acting in the *j*-direction on a surface normal to the *i*-axis.

For Newtonian fluids where shear stress is proportional to the strain rate tensor, $\tau_{ij}$ can be written as

$$\tau_{ij} = 2\mu s_{ij} \qquad \textbf{2-4}$$

where $\mu$ is the viscosity of the fluid and $s_{ij}$ is the strain rate tensor

$$s_{ij} = \frac{1}{2}\left( \frac{\partial u_i}{\partial x_j} + \frac{\partial u_j}{\partial x_i} \right) \qquad \textbf{2-5}$$

By substituting the shear stress term in *eq. 2-3* with *eq. 2-4* and *eq. 2-5* and assuming that the fluid is incompressible, the momentum balance can be written in Eulerian coordinate as (Davidson, 2004)

$$\frac{\partial u_i}{\partial t} + u_j \frac{\partial u_i}{\partial x_j} = -\frac{1}{\rho}\frac{\partial p}{\partial x_i} + \nu \frac{\partial^2 u_i}{\partial x_j \partial x_j} \qquad \textbf{2-6}$$

where $\nu$ is the kinematic viscosity of the fluid, $\nu = \mu/\rho$. *Eq. 2-6* is known as Navier-Stokes equation.

The solution of the momentum balance (*eq. 2-3*) together with the mass balance (*eq. 2-1*) depends on the flow geometry and boundary conditions (wall, inlet, outlet, symmetry, etc). However, its analytical solution is almost impossible, except for laminar flow in a very simple geometric, such as pipe, where the flow is practically one dimensional and assumption can be made to simplify the

equation. Computational Fluid Dynamics (CFD) is a numerical approach to solve the partial differential equations of mass, momentum and energy balances. To obtain numerical solution of those equations, the flow domain is divided into many control volumes or computational cells which can be quadrilaterals or triangles in 2D domain or tetrahedral, prisms, pyramids or hexahedra in 3D domain (Marshall and Bakker, 2004). The partial differential equations of mass and momentum balances are discretised into algebraic equations which can be solved numerically.

There are various techniques to discretised partial differential equations such as finite volume method (used by commercial CFD packages Fluent, CFX and StarCD), finite element method (used by POLY3D and Comsol), spectral method and lattice Boltzman method (Eggels and Somers, 1996; Derksen, 2001). In finite volume method, the values of all variables (such as velocity components, pressure and temperature) are stored in the center of computational cells, but they are evaluated at the cell faces. To obtain the values of these variables at cell faces as a function of those at cell centers, a discretization scheme is required (Marshall and Bakker, 2004).

In this section, the turbulent modelling and the comparison of turbulence models are discussed but the details of discretization schemes and methods of solving the discretised equations are discussed further elsewhere (Patankar, 1980; Versteeg and Malalasekera, 1995; Marshall and Bakker, 2004). And finally, this chapter recommends turbulence model suitable for rotor-stator mixer simulation.

## 2.2. Direct Numerical Simulation (DNS)

The Navier-Stokes equation (*eq. 2-6*) and mass balance (*eq. 2-2*) form a closed set of partial differential equations with four equations and four unknowns ($u_x$, $u_y$, $u_z$ and $p$). For laminar flow, the solution can be obtained directly with relatively coarse computational cells. For turbulent flow, however, very fine computational cells are required to resolve the entire scales of turbulence since the structure of turbulent flow is much more complex than laminar flow although they are governed by the same equations.

Turbulent flow is an irregular condition of flow in which various quantities show a random variation with time and space (Hinze, 1976). It is characterized by eddies of various scales. The largest eddies arise from the instability of main flow in the size of flow boundary condition such as pipe diameter. These large eddies break down into smaller eddies and then into even smaller eddies until finally viscous action dissipates them into heat (Mathieu and Scott, 2000). The scale where smallest eddies are dissipated by viscous force into heat is called Kolmogorov microscale ($\eta$) and can be related to integral scale ($\ell$) by (Davidson, 2004)

$$\eta \approx \ell \, Re_{\ell}^{-3/4} \qquad \textbf{2-7}$$

where $Re_{\ell}$ is the Reynolds number based on integral scale.

Therefore, to solve turbulent flow directly, the computational cells should be in the same order as Kolmogorov microscale. The number of computational cells required to do this simulation is in the order of $Re_{\ell}^{9/4}$ (Mathieu and Scott,

2000). Hence, for turbulent flow in the pipe with $Re_t$ = 4000, the number of computational cells is in the order of $10^8$. Moreover, the simulation must be carried out in unsteady mode with a very small time step in the order of Kolmogorov time scale which is the ratio of Kolmogorov microscale to Kolmogorov velocity scale. Therefore, the computational cost of DNS increases drastically with the Reynolds number and with current capabilities of computing power, it is not practical to do such simulation for a turbulent flow at high Reynolds number typically found in industry or engineering research.

However, DNS is a valuable tool to identify the structure of turbulence including the structure of homogeneous turbulence, understanding of the three-dimensional vortical structure in mixing layer and orientatation of the vorticity vector to the strain-rate tensor in turbulence (Baldyga and Bourne, 1999). DNS data can also be used to develop and verify new sub-grid scale (SGS) eddy viscosity model, such as dynamic SGS model (Germano et al., 1991), for large eddy simulation (LES).

With the advance of computational technology, it is possible to do DNS in stirred tank at low Reynolods number. Lavezzo et al. (2009) simulated the flow pattern and particles motion in a stirred tank using DNS. The total number of computational cells used was about 15 million. The tank had diameter of 0.1 m and the Reynolds number based on the impeller tip speed was only 1,636. The grid size was between 3.5 and 5 times the estimated Kolmogorov microscale. However, the computational time was not explained.

## 2.3. Reynolds Averaged Navier-Stokes (RANS) models

To overcome the limitation of computational resources, turbulence model is used. One class of turbulence models is Reynolds Averaged Navier-Stokes (RANS) turbulence model. It based on the Reynolds decomposition which divides turbulent flow into mean velocity and fluctuating component. The instantaneous velocity component in a point in turbulent flow, $u_i$, can be written as

$$u_i = U_i + u_i' \qquad \textbf{2-8}$$

where $U_i$ is the mean velocity component which is the time or ensemble average of $u_i$ and $u_i'$ is the fluctuating component of $u_i$. The time or ensemble average of $u_i'$ is zero, but the root mean square of $u_i'$ is not.

For incompressible Newtonian fluid and in the absence of any body forces, introducing Reynolds decomposition into continuity and Navier-Stokes equations (*eq. 2-2* and *eq. 2-6* respectively) gives

$$\frac{\partial U_i}{\partial x_i} = 0 \qquad \textbf{2-9}$$

$$\frac{\partial U_i}{\partial t} + U_j \frac{\partial U_i}{\partial x_j} = -\frac{1}{\rho}\frac{\partial P}{\partial x_i} + \nu \frac{\partial^2 U_i}{\partial x_j \partial x_j} - \frac{\partial \overline{u'_i u'_j}}{\partial x_j} \qquad \textbf{2-10}$$

The averaging procedure introduces new variables $\tau'_{ij} = \rho\overline{u'_i u'_j}$ called Reynolds stress tensor which represent the mean flux of momentum due to turbulent fluctuations. The introduction of Reynolds stress tensor means that the set of continuity and Navier-Stokes equations are no longer closed. Generally, the closure model for RANS equation can be divided into eddy viscosity model and shear stress transport model (Baldyga and Bourne, 1999).

### 2.3.1 Eddy viscosity model

The eddy viscosity concept is based on the Boussinesq approximation which states that Reynolds stresses can be expressed in terms of mean rate of strain of the mean velocity field (Bruun, 1995)

$$\overline{u_i' u_j'} = -\nu_t \left( \frac{\partial U_i}{\partial x_j} + \frac{\partial U_j}{\partial x_i} \right) + \frac{2}{3} k \delta_{ij} \qquad \textbf{2-11}$$

where $\nu_t$ is the turbulent viscosity, $k$ is the turbulent kinetic energy per unit mass and $\delta_{ij}$ is Kronecker delta ($\delta_{ij} = 1$ if $i = j$, otherwise $\delta_{ij} = 0$). This is analogue to the laminar shear stress. Substituting *eq. 2-11* into *eq. 2-10* gives

$$\frac{\partial U_i}{\partial t} + U_j \frac{\partial U_i}{\partial x_j} = -\frac{1}{\rho} \frac{\partial P}{\partial x_i} - \frac{2}{3} \frac{\partial k}{\partial x_i} + (\nu + \nu_t) \frac{\partial^2 U_i}{\partial x_j \partial x_j} \qquad \textbf{2-12}$$

where $k$ is the turbulent kinetic energy per unit mass. *Eq. 2-12* shows that based on the eddy viscosity model, the turbulence increases viscosity by turbulent viscosity, where turbulent viscosity can be much higher than viscosity (Davidson, 2004). However, unlike $\nu$ which is the property of fluid, $\nu_t$ is determined by the structure of the flow and is not the property of fluid. Hence, another closure model is required to quantify $\nu_t$. Based on the number of partial differential equations, the closure model can be a zero-equation (algebraic) model, one-equation model or two-equation model (Versteeg and Malalasekera, 1995).

#### 2.3.1.1 Zero-equation model

The zero-equation model is also known as Prandtl mixing length model. It was developed to describe the flow in thin shear layer including wakes, jets and

ducted flows, where strain field is dominated by a single shear strain, $\frac{\partial U_x}{\partial y}$, and the only significant Reynolds stress is $\tau'_{xy} = \tau'_{yx} = \rho\overline{u'_x u'_y}$ (Bruun, 1995). The relation between the length scale ($\ell$) and velocity scale ($V$) can be written as

$$V = c\ell\left|\frac{\partial U_i}{\partial t}\right| \qquad \textbf{2-13}$$

where $c$ is a constant. Based on the dimensional analysis, turbulent viscosity ($\nu_t$), which has dimensions $m^2s^{-1}$, can be expressed as a product of a turbulent velocity scale and a length scale as follows (Versteeg and Malalasekera, 1995)

$$\nu_t = cV\ell \qquad \textbf{2-14}$$

Combining *eq. 2-13* and *eq. 2-14* gives

$$\nu_t = \ell_m^2\left|\frac{\partial U_i}{\partial t}\right| \qquad \textbf{2-15}$$

where $\ell_m$ is the mixing length which value depend on the flow. Some value of $\ell_m$ in various two-dimensional turbulent flows as listed in *Table 2.1*.

***Table 2.1.*** *Mixing Lengths for two-dimensional turbulent flows (from Versteeg and Malalasekera, 1995)*

| **Type of flow** | **Mixing length ($\ell_m$)** | ***L*** |
|---|---|---|
| Mixing layer | 0.07 *L* | Layer width |
| Jet | 0.09 *L* | Jet half width |
| Wake | 0.16 *L* | Wake half width |
| Axisymmetric jet | 0.075 *L* | Jet half width |
| Boundary layer | | |
| Viscous sub layer and Log-law layer | $\kappa y[1-\exp(-y^+/26)]$ | Boundary layer thickness |
| Outer layer | 0.09 *L* | |
| Pipes and channels (fully developed flow) | $L[0.14-0.08(1-y/L)^2-0.06(1-y/L)^4]$ | Pipe radius or channel half width |

$\kappa$ is the von Karman constant ≈ 0.41
$y$ is the normal distance from wall
$y^+$ is the dimensionless $y$ ($y^+ = yu_\tau/\nu$, where $u_\tau$ is the friction velocity)

#### 2.3.1.2 One-equation model

In this model, turbulent viscosity is related to the root mean square of turbulent kinetic energy, *k*, which gives

$$\nu_t = \ell\sqrt{k} \qquad \textbf{2-16}$$

For two-dimensional boundary layer flows, *k* can be approximated by using the following transport equation (Baldyga and Bourne, 1999)

$$\underset{convection}{U_1 \frac{\partial k}{\partial x_1}} + \underset{}{U_2 \frac{\partial k}{\partial x_2}} = \underset{diffusion}{\frac{\partial}{\partial x_2}\left(\frac{\nu_t}{\sigma_k}\frac{\partial k}{\partial x_2}\right)} + \underset{productio\ n}{\nu_t\left(\frac{\partial U_1}{\partial x_2}\right)} - \underset{dissipatio\ n}{C_D \frac{k^{3/2}}{\ell}} \qquad \textbf{2-17}$$

where $C_D$ and $\sigma_k$ are the model constants with values of 0.08 and 1 respectively. The length scale, $\ell$, should be specified algebraically as in the case of zero equation model.

The main drawback of this model is the same as zero equation model, that is the length-scale must be prescribed algebraically.

#### 2.3.1.3 Two-equation model

The most popular of two-equation models is k-ε model and therefore only this model will be discussed in here. In this model, the length scale and turbulent viscosity are expressed in *k* and $\varepsilon$ as follows

$$l = \frac{k^{3/2}}{\varepsilon} \qquad \textbf{2-18}$$

$$\nu_t = C_\mu \frac{k^2}{\varepsilon} \qquad \textbf{2-19}$$

The transport equations for $k$ and $\varepsilon$ are given by *eq. 2-22* and *eq. 2-23* in *Table 2.2*.

The Reynolds stress tensor in k-ε model is calculated using Boussinesq relationship (*eq. 2-11*). The complete set of momentum balance including standard k-ε model is given in *Table 2.2*. The k-ε model has been the standard turbulent model for the engineering purposes due to its stability and fairly good performance in simulation of many industrial flows. Other versions, such as re-normalized group (RNG) k-ε model and realizable k-ε model, have been developed for the flows which include strong swirl such as the flow in the stirred tank. The other two-equation models are k-ω model and k-τ model. Their details are given elsewhere (Wilcox, 1993 and Speziale et al., 1990 respectively).

***Table 2.2.*** *Complete set of continuity and RANS equations with standard k-$\varepsilon$ closure model (from Fluent User Manual)*

| | |
|---|---|
| $\frac{\partial U_i}{\partial x_j} = 0$ | **2-20** |
| $\frac{\partial U_i}{\partial t} + U_j \frac{\partial U_i}{\partial x_j} = -\frac{1}{\rho}\frac{\partial P}{\partial x_i} - \frac{2}{3}\frac{\partial k}{\partial x_i} + (\nu + \nu_t)\frac{\partial}{\partial x_j}\left(\frac{\partial U_i}{\partial x_j} + \frac{\partial U_j}{\partial x_i}\right)$ | **2-21** |
| $\frac{\partial k}{\partial t} + U_j \frac{\partial k}{\partial x_j} = \frac{\partial}{\partial x_j}\left(\nu + \frac{\nu_t}{\sigma_k}\frac{\partial k}{\partial x_j}\right) + \nu_t\left[\left(\frac{\partial U_i}{\partial x_j} + \frac{\partial U_j}{\partial x_i}\right)\frac{\partial U_i}{\partial x_j}\right] - \varepsilon$ | **2-22** |
| $\frac{\partial \varepsilon}{\partial t} + U_j \frac{\partial \varepsilon}{\partial x_j} = \frac{\partial}{\partial x_j}\left(\nu + \frac{\nu_t}{\sigma_\varepsilon}\frac{\partial \varepsilon}{\partial x_j}\right) + C_{\varepsilon 1}\nu_t \frac{\varepsilon}{k}\left[\left(\frac{\partial U_i}{\partial x_j} + \frac{\partial U_j}{\partial x_i}\right)\frac{\partial U_i}{\partial x_j}\right] - C_{\varepsilon 2}\frac{\varepsilon^2}{k}$ | **2-23** |
| $\nu_t = C_\mu \frac{k^2}{\varepsilon}$ | **2-24** |
| $C_\mu = 0.09, \sigma_k = 1, \sigma_\varepsilon = 1.3, C_{\varepsilon 1} = 1.44, C_{\varepsilon 2} = 1.92$ | |

## 2.3.2 Shear stress transport model

The main shortcoming of two-equation model originates from the linearity of the Boussinesq hypothesis which results in a poor description of rotational

mean flows and effects of streamline curvature (Hallback et al., 1995). Alternatively, Reynolds stress tensor can be calculated by using shear stress transport equations. However, it requires a lot of computing effort as there is six additional equations to calculate six independent Reynolds stresses.

The differential equations governing the transport of Reynolds stresses, $\overline{u_i' u_j'}$, can be written as (Launder et al., 1975)

$$\underbrace{\frac{D\overline{u_i' u_j'}}{Dt}}_{\text{total change}} = \underbrace{-\left[\overline{u_j' u_k'}\frac{\partial U_i}{\partial x_k} + \overline{u_i' u_k'}\frac{\partial U_j}{\partial x_k}\right]}_{\text{generation } (G_{ij})} + \underbrace{2\nu\overline{\frac{\partial u_i'}{\partial x_k}\frac{\partial u_j'}{\partial x_k}}}_{\text{dissipation } (\varepsilon_{ij})} - \underbrace{\overline{\frac{p'}{\rho}\left(\frac{\partial u_i'}{\partial x_j} + \frac{\partial u_j'}{\partial x_i}\right)}}_{\text{pressure strain } (\phi_{ij})}$$

$$\underbrace{-\frac{\partial}{\partial x_k}\left[\overline{u_i' u_j' u_k'} - \nu\overline{\frac{\partial u_i' u_j'}{\partial x_k}} + \overline{\frac{p'}{\rho}\left(\delta_{jk}u_i + \delta_{ik}u_j\right)}\right]}_{\text{turbulent diffusion } (D_{Tij})} \qquad \textbf{2-25}$$

This model is very complex and details of this model are given elsewhere (Launder et al., 1975, Speziale et al., 1991). In Fluent, the scalar dissipation rate, $\varepsilon$, and turbulent kinetic energy, $k$, are calculated by using the same transport equations used to calculate $k$ and $\varepsilon$ in standard k-ε model respectively (*Table 2.2*). The turbulent viscosity, $\nu_t$, is also expressed in the same way as in the standard $k$-$\varepsilon$ model (Fluent User's Manual).

## 2.4. Large Eddy Simulation (LES)

In DNS, 99.99 % of computational resources are used to simulate the behaviour of small to intermediate scale eddies, and only 0.01 % are used to simulate large scale eddies which are responsible for the transport of momentum, mass, energy, and components are more interesting than small eddies (Davidson,

2004). Large eddy simulation (LES) is an intermediate technique between DNS and RANS. It solves three-dimensional, time dependent continuity and momentum balance equations for large scale eddies and models the effect of small scale eddies. Since small scale eddies are geometric independent, isotropic, and therefore more universal than large scale eddies, there is hope that LES can be simpler and require fewer adjustments when applied to different flows than similar models based on the RANS equations (Hallback et al., 1995). The computational resources required by LES are 10 to 1000 time less than DNS, but 10 to 100 times more than RANS based model (Bakker and Oshinowo, 2004).

The governing equations for LES are obtained by spatially filtering continuity and momentum equations so that eddies smaller than filter width are removed. The filtering process can be described as follows (Davidson, 2004)

$$\tilde{u}_i(x) = \int_{-\infty}^{\infty} u_i(x-r)G(r)dr \qquad \textbf{2-26}$$

where $\tilde{u}_i(x)$ is the local average of $u_i$ in the neighborhood of $x$ over the filter width, $\Delta$, which represents the motion of large eddies. The most commonly-used filter functions are shown in *Table 2.3*. The filtered continuity and Navier-Stokes equations are analogues to the RANS equations. The instantaneous velocity is written as

$$u_i = \tilde{u}_i + u_i^R \qquad \textbf{2-27}$$

where $u_i^R$ is the residual velocity. The difference between the filtered and the averaged Navier-Stokes equations is that $\overline{\tilde{u}}_i \neq \tilde{u}_i$ and hence $\overline{u_i^R} \neq 0$ (Davidson, 2004, Rousinova et al., 2003).

***Table 2.3.*** *The commonly used filter in the LES filtering operation (from Davidson, 2004)*

| Filter | Definition |
|---|---|
| Top-hat filter / box filter (used in Fluent) | $G(r) = 1/\Delta$ if $\lvert r \rvert \le \Delta/2$<br>0 otherwise |
| Gaussian filter | $G(r) = \dfrac{\exp\left(-r^2/\Delta^2\right)}{\sqrt{\pi}\Delta}$ |
| Fourier cut-off filter (expressed in wave space) | $G(r) = \dfrac{\sin(\pi r/\Delta)}{\pi r}$ |

Where Δ is the filter width

The filtering of Navier-Stokes equations introduces the subgrid-scale stresses, $\tilde{\tau}_{ij}$, which are unknown and have to be modelled. The most popular method to model subgrid-scale stresses is employing an eddy-viscosity model or Boussinesq hypothesis (Davidson, 2004)

$$\tilde{\tau}_{ij} = 2\rho\nu_R\tilde{S}_{ij} + \frac{1}{3}\tilde{\tau}_{kk}\delta_{ij} \qquad \textbf{2-28}$$

where $\nu_R$ is the residual kinematics viscosity and $\tilde{S}_{ij}$ is the strain rate tensor for the resolved scale defined by

$$\tilde{S}_{ij} = \frac{1}{2}\left(\frac{\partial\tilde{u}_i}{\partial x_j} + \frac{\partial\tilde{u}_j}{\partial x_i}\right) \qquad \textbf{2-29}$$

The residual kinematics viscosity, $\nu_R$, needs to be modelled to close the filtered Navier-Stokes equations by using subgrid-scale (SGS) model. The most widely used SGS model is Smagorinsky model where $\nu_R$ is expressed as (Davidson, 2004)

$$\nu_R = C_S^2\Delta^2\left(2\tilde{S}_{ij}\tilde{S}_{ij}\right)^{1/2} \qquad \textbf{2-30}$$

where $C_S$ is Smagorinsky coefficient which is usually given a value of 0.1.

The value of $C_S$ depends on the type of turbulent flow. For isotropic turbulence with cutoff in the inertial subrange and filter width equals to the grid size, $C_S$ is approximately 0.17 (Lilly, 1966). However, in the presence of mean shear, this value was found to cause excessive damping of large-scale fluctuation (Germano et al., 1991). In the shear flow, Deardorf (1970) and Moin and Kim (1982) suggested $C_S = 0.1$ also with filter width equals to the grid size, while in the mixing layer flow, $C_S = 0.12 – 0.14$ (Yoshizawa, 1991).

Despite varying value of $C_S$, some simulations of stirred tanks using LES have been successfully performed using constant $C_S$ value of 0.1 (*Table 2.5*). However, Delafosse et al. (2008) showed that the mean flow and kinetic energy were not sensitive to $C_S$ but the energy dissipation rate was. To overcome this problem, a dynamic SGS model (Germano et al., 1991) where $C_S$ is dynamically computed from the local flow or dynamic kinetic energy SGS model (Kim and Mennon, 1997) have been proposed.

## 2.5. Comparison between RANS simulation and LES

During the last few years, the advance in computer technology has made LES more affordable than before. LES resolves the time dependent motion of large eddies and models only the more isotropic small eddies, therefore, it can provide the information about transient behaviour of a process, such as trailing vortices and macro instability, which can not be provided by RANS simulation, in the expense of computational cost. This section presents the comparison between RANS simulation and LES in terms of computational cost and performance of

each model. However, since CFD simulations of rotor-stator mixer is very hard to find in the literature, the comparison is made based on stirred tank simulations.

***Table 2.4.*** *Previous RANS simulations of stirred tanks*

| **Author** | **Tank geometry** | **Grid size** | **Grid density** |
|---|---|---|---|
| **Impeller** | **Impeller speed** | | **Time step** |
| Jaworski et al., 1998 | H = T = 0.22 | 9,639 | 4.6 cells/cm$^3$ |
| APV – B2 | D = 0.45 T, C = T/3 | (1/4 tank) | Steady state |
| | N = 200 rpm | | |
| Ng et al., 1998 | H = T = 0.1 m | 46,000 – | 117 – 611 cells/ cm$^3$ |
| Rushton turbine | D = T/3, C = T/3 | 240,000 | 7.7 x 10$^{-5}$ s |
| | N = 2165 rpm | (1/2 tank) | |
| Jaworski et al., 2000 | H = 2T = 1.44m | 69,972 | 0.24 cells/cm$^3$ |
| Dual Rushton turbines | D = T/2 | (1/2 tank) | Steady state |
| | Various N | | |
| Montante et al., 2001 | H = T = 0.29 m | 51,900 – | 2.4 – 15.1 cells/cm$^3$ |
| Rushton turbine | D = T/3, various C/T | 189,696 | 2.2 – 6.7 x 10$^{-3}$ s |
| | N = 250 rpm | (1/2 tank) | |
| Jaworski et al., 2002 | H = T = 0.202 | 31,744 | 9.8 cells/cm$^3$ |
| 45$^o$ PBT, up and down | D = T/3 – T/2 | (1/2 tank) | Steady state |
| pumping modes | N = 200 – 300 rpm | | |
| Bujalski et al., 2002 | H = T = 0.22 m | 130,680 | 15.6 cells/cm$^3$ |
| Rushton turbine | D = 0.46 T, C = T/3 | (full tank) | 1.36 x 10$^{-2}$ s |
| | N = 50 rpm | | |
| Aubin et al., 2004 | H = T = 0.19 m | 76,000 – | 14.1 – 65 cells/cm$^3$ |
| PBT, up and down | D = T/2, C = T/3 | 350,000 | Steady state |
| pumping mode | N = 300 rpm | (full tank) | |
| Yeoh et al., 2004 | H = T = 0.1 m | 250,000 | 636.6 cells/cm$^3$ |
| Rushton turbine | D = T/3, C = T/3 | (1/2 tank) | Steady state |
| | N = 2165 rpm | | |
| Deglon and Meyer, 2006 | H = T = 0.15 m | 33,000 – | 14.9 – 1434 cells/cm$^3$ |
| Rushton turbine | D = T/3, C = T/3 | 1,900,000 | Steady state |
| | Various N | (1/2 tank) | |
| Murthy and Joshi, 2008 | H = T = 0.3 m | 575,000 | 27.1 cells/cm$^3$ |
| Various impellers | D = T/3, C = T/3 | (full tank) | Initially at 10$^{-4}$ s, then |
| | N = 270 rpm | | increased to 10$^{-2}$ s |
| Delafosse et al., 2008 | H = T = 0.45m | 1,000,000 | 13.97 cells/cm$^3$ |
| Rushton turbine | D = T/3, C = T/3 | (full tank) | 5.56 x 10$^{-4}$ s |
| | N = 150 rpm | | |
| Gimbun et al., 2009 | H = T = 0.222 m | 225,000 | 54.8 cells/cm3 |
| Rushton turbine, CD-6 | D = T/3, C = T/2 | (1/2 tank) | |
| Gas – liquid system | N = 513 rpm | | |

*Table 2.4* summarizes the previous studies of stirred tanks using RANS simulations (most of them using standard $k$-$\varepsilon$ model). The simulations were usually carried out in half or quarter tank domains using periodic boundary condition to save computational resources. The number of computational cells

ranged from about $10^4$ to about $10^6$ and simulations can be carried out in either steady or transient mode. With the increasing computational power, there is tendency to increase the minimum grid size in the order of $10^5$.

***Table 2.5.*** *Previous large eddy simulations (LES) of stirred tanks*

| **Author**<br>**Impeller** | **Tank geometry**<br>**Impeller speed** | **Grid size**<br>**SGS model** | **Grid density**<br>**Time step and remarks** |
|---|---|---|---|
| Baker and Oshinowo, 2000<br>Various impellers | T = 0.202 – 0.292 m<br>Various tank configuration<br>Various N | 500,000 – 763,000 (1/4 tank)<br>RNG SGS model | 25.6 – 117.9 cells/cm$^3$<br>3.45 – 10 x $10^{-3}$ s<br>22 - 178 impeller revolutions (various initial conditions) |
| Roussinova et al., 2003<br>45$^o$ PBT down pumping mode | H = T = 0.24 m<br>D = T/2, C = T/2<br>N = 200 rpm | 500,000<br>Smagorinsky SGS model , $C_s$ = 0.1 | 46 cells/ cm$^3$<br>0.01 s<br>78 impeller revolutions<br>Started from zero velocity field |
| Yeoh et al., 2004<br>Rushton turbine | H = T = 0.1 m<br>D = T/3, C = T/3<br>N = 2165 rpm | 490,000<br>Smagorinsky SGS model, $C_s$ = 0.1 | 623.9 cells/cm$^3$<br>1.28 x $10^{-4}$ s<br>45 impeller revolutions |
| Alcamo et al., 2005<br>Rushton turbine | H = T = 0.19 m<br>D = T/2, C = T/3<br>N = 200 rpm | 761,760<br>Smagorinsky SGS model, $C_s$ = 0.1 | 141.4 cells/cm$^3$<br>1.28 x $10^{-4}$ s |
| Murthy and Joshi, 2008<br>Various impellers | H = T = 0.3 m<br>D = T/3, C = T/3<br>N = 270 rpm | 1,275,567<br>Dynamic kinetic energy SGS model | 60.2 cells/cm$^3$<br>Initially at $10^{-4}$ s, then increased to $10^{-3}$ s<br>440 impeller revolutions, initiallized by k-ε prediciton |
| Delafosse et al., 2008<br>Rushton turbine | H = T = 0.45m<br>D = T/3, C = T/3<br>N = 150 rpm | 1,000,000<br>Smagorinsky SGS model, $C_s$ = 0.1 and 0.2 | 13.97 cells/cm$^3$<br>5.56 x $10^{-4}$ s<br>60 impeller revolutions |

*Table 2.5* summarizes previous large eddy simulations performed in finite volume method. The number of computational cells used in LES varied from about 500,000 to more than 1 million. Some large eddy simulations were carried out using lattice Boltzmann method with significantly higher number of computational cells (up to more than 10 millions computational cells) than those in finite volume method (Eggels and Somers, 1996; Derksen and Van den Akker,

1999; Derksen, 2001). LES needs to be performed in full tank domain since the instantaneous velocity profile of large eddies is not symmetrical. LES also requires transient simulation with small time step, about an order of magnitude lower than that in transient RANS simulation, to capture the dynamics of large eddies.

The filter size (Δ) in LES, which is proportional to or the same as grid size, should lie in the inertial subrange so that the bulk of the energy containing eddies can be resolved (Davidson, 2004). Yeoh et al. (2004) employed grid size which was smaller than the integral scale determined by LDA experiment. Murthy and Joshi (2008) suggested that the grid size in LES should lie between the Kolmogorov microscale and Taylor microscale. Both microscales can be estimated by using RANS turbulence model, such as k-ε model. The Kolmogorov microscale ($\eta$) can be calculated by using

$$\eta=\left(\nu^3/\varepsilon\right)^{0.25} \qquad \textbf{2-31}$$

and the Taylor microscale ($\lambda$) can be calculated by using (Escudie and Line, 2003)

$$\lambda=\sqrt{\frac{10\nu k}{\varepsilon}} \qquad \textbf{2-32}$$

Alternatively, the Kolmogorov microscale can be estimated from average energy dissipation rate ($\bar{\varepsilon}$), i.e. $\eta=\left(\nu^3/\bar{\varepsilon}\right)^{0.25}$ and the Taylor microscale can be related to $\eta$ and *Re*, i.e. $\lambda \approx \sqrt{10}\eta Re^{0.25}$ (Davidson, 2004).

Another problem associated with LES is the near wall treatment of turbulence. The grid near the wall should be small enough so that LES effectively becomes a DNS or, alternatively, the flow near the wall is calculated by using

boundary layer model while the outer flow is calculated by using LES (Davidson, 2004). The later approach is termed Detached Eddy Simulation (DES) in Fluent (Fluent Users' Manuals).

Murthy and Joshi (2008) compared the flow patterns in vessels fitted with different impellers (Rushton turbine, pitched blade turbine $30^o$, $45^o$, $60^o$ and hydrofoil impeller) predicted by LES with RANS turbulence models, i.e. standard $k$-$\varepsilon$ model which assumes isotropic turbulence and Reynolds Stress Model (RSM) which take into account anisotropic turbulence. The predicted velocity profiles were compared in a vertical plane between two baffles. In terms of mean velocity profiles, standard k-ε model generally gave reasonably good predictions although the predictions were rather poor in some parts of the tank, while RSM and LES gave better predictions in the proximity of the impellers and in the bulk regions. Yeoh et al. (2004) also found that LES predictions on mean velocity components were generally better than standard k-ε model but not in all cases. In terms of turbulent kinetic energy, both RANS turbulence models gave reasonably good predictions of turbulent kinetic energy in the bulk regions, but perform poorly in the impeller regions. On the other hand, LES can provide good predictions in both regions (Yeoh et al., 2004 and Murthy and Joshi, 2008).

Yeoh et al. (2004) reported that the power number (calculated from the integral of energy dissipation rate over the whole vessel) predicted by LES with Smagorinsky SGS model ($C_s$ = 0.1) was about 15% higher than the experimental value, while standard k-ε model (simulated in half tank domain) underpredicted the power number by 45%. Murthy and Joshi (2008) reported that the LES (using

dynamic kinetic energy SGS model) predictions of power numbers were about 10% lower than the experimental values, while both RANS turbulence models (simulated in full tank domain) underpredicted the power number of Rushton turbine by 25%, but only underpredicted the power numbers of pitched blade turbines ($30^o$, $45^o$ and $60^o$) and hydrofoil impeller about 15%.

## 2.6. Conclusions

LES is a very good turbulence model, however, it is not only more computationally demanding than RANS turbulence model, but it also more complicated. Previous experimental and simulation results are required to determine the grid size in the critical regions. Unfortunately, for rotor-stator mixer, both experimental and simulation results are very limited and not well established.

On the other hand, standard k-ε model which assumes isotropic turbulence can provide reasonably good predictions of mean velocity components in the stirred tanks although it underestimates turbulent kinetic energy and energy dissipation rate. Based on this data, we decided to use standard k-ε model in this work. Moreover LES is usually started from convergent solution of RANS simulation to speed up its convergence.

Rotor-stator simulation using RSM was also performed and the comparison between standard k-ε model and RSM is given in Appendix B. However, since its predictions of velocity profiles were practically the same as

standard k-ε model but it required more computational resources and stringent grid quality, we decided to abandon this model.

# CHAPTER III

# FLOW MEASUREMENT DEVICES

## 3.1. Introduction

This chapter gives brief descriptions about various measurement devices which are widely used to measure fluid velocity, i.e. hot wire anemometer (HWA), laser Doppler anemometry (LDA) and particle image velocimetry (PIV). Those devices are compared and the most suitable device to characterize the flow in a batch rotor-stator mixer is selected for this work. Details of the selected instrument are given subsequently.

## 3.2. Hot wire anemometry (HWA)

HWA is a single point measurement technique based on convective heat transfer from a heated sensor (Bruun, 1995). The sensor can be a thin platinum coated tungsten wire of about 5 μm in diameter and about 1 mm in length for velocity measurement in clean gas or a thin film of platinum or nickel deposited on aerodynamically shaped quartz substrate (wedge, cone or flat plate) for velocity measurement in liquid since the thin wire is susceptible to contamination. One, two or three sensors are used to measure one, two or three velocity components respectively. HWA can operate in constant current mode or constant temperature mode. However, the constant temperature anemometer (CTA) is much simpler to use and control than the constant current one and most velocity

measurements are now carried out with constant temperature system (Bruun, 1995). Therefore, only CTA is discussed in this section.

Typical CTA arrangement is illustrated in *Fig. 3.1*. The sensor is connected to one arm of a Wheatstone bridge and heated by an electric current. The fluid flow cools the sensor and creates error voltage in the Wheatstone bridge since the wire resistivity and hence wire resistance changes with temperature. A servo amplifier generates an electric current based on this error voltage and feeds it back to the bridge to restore sensor temperature and hence sensor resistance. The bridge voltage represents the heat transferred to the liquid and can be related to fluid velocity (Bruun, 1995).

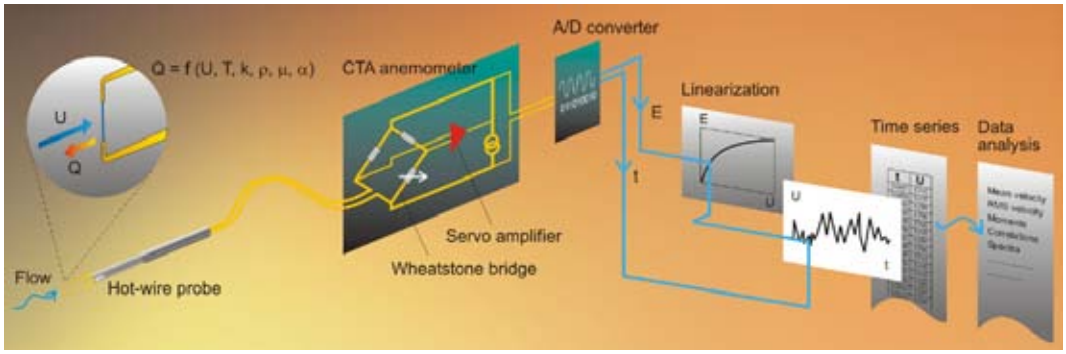


***Fig. 3.1.*** *Typical CTA arrangement (from www.dantecdynamics.com).*

The relationship between the output voltage, $E$, and instantaneous velocity can be expressed in exponential function (King, 1914)

$$E^2 = A + Bu_e^n \qquad \textbf{3-1}$$

or in the more straight forward polynomial function (George et al., 1989)

$$u_e = C_0 + C_1 E + C_2 E^2 + C_3 E^3 + \ldots \qquad \textbf{3-2}$$

where $u_e$ is the effective instantaneous velocity. The sensor has different responses to normal ($u_N$), tangential ($u_T$) and binormal ($u_B$) velocity components relative to the sensor coordinate system (*Fig. 3.2*) and hence $u_e$ is expressed as

$$u_e^2 = u_N^2 + k^2 u_T^2 + h^2 u_B^2 \qquad \textbf{3-3}$$

Where $k$ and $h$ are often referred to as sensor yaw and pitch coefficients respectively. Typical values for $k$ and $h$ for a standard hot wire probe are 0.2 and 1.05 respectively (Bruun, 1995). The constants in eq. *3-1* and *3-2* can be found from calibration.

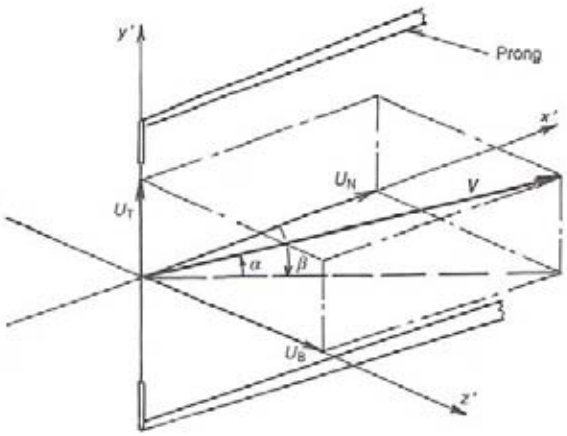


***Fig. 3.2.*** *Decomposition of velocity vector* ***V*** *into normal ($u_N$), tangential ($u_T$) and binormal ($u_B$) velocity components relative to the sensor coordinate system (from Bruun, 1995).*

CTA provide velocity time series with sampling rate up to several hundred kHz which then can be processed to give mean velocity, turbulence intensity and higher order moments such as skewness (third moment) and flatness factor (fourth moment). Since it provides data with uniform sampling interval, the auto-correlation and power spectra can be obtained directly using fast Fourier transform (FFT).

## 3.3. Laser Doppler Anemometry (LDA)

LDA is a non-intrusive optical technique to measure instantaneous velocity at a specific point. It measures the velocity of seeding particles moving with fluid instead of the velocity of the fluid itself. The seeding particles (usually between 1 and 10 μm) should be small enough to follow fluid motion but should be large enough to scatter the laser light so that the signal can be captured by a photo detector.

LDA employs two coherent and linearly polarized laser beams which intersect at their waists (*Fig. 3.3*). According to the principle of superposition of oscillations, this intersection creates regions with maxima and minima intensity which are referred to as bright and dark fringes respectively. Those fringes are perpendicular to the plane where both beams lie and the intersection volume is called the measurement volume which is an ellipsoid with typical diameter about 0.1 mm or less and length about 1 mm or less. The fringe spacing, $d_f$, is constant and is defined by the wavelength of the laser, $\lambda$, and the intersection angle between the beams, $\theta$, as follows

$$d_f = \frac{\lambda}{2\sin(\theta/2)} \qquad \textbf{3-4}$$

When a particle crosses these oscillating dark and bright fringes, it generates oscillating signal which is captured by a photo detector. The signal is then sent to a signal processor to remove noise and extract the Doppler frequency. The velocity component perpendicular to the fringes, $u_p$, can be calculated from the Doppler frequency, $f_D$, as follows

$$u_p = d_f \times f_D \qquad \textbf{3-5}$$

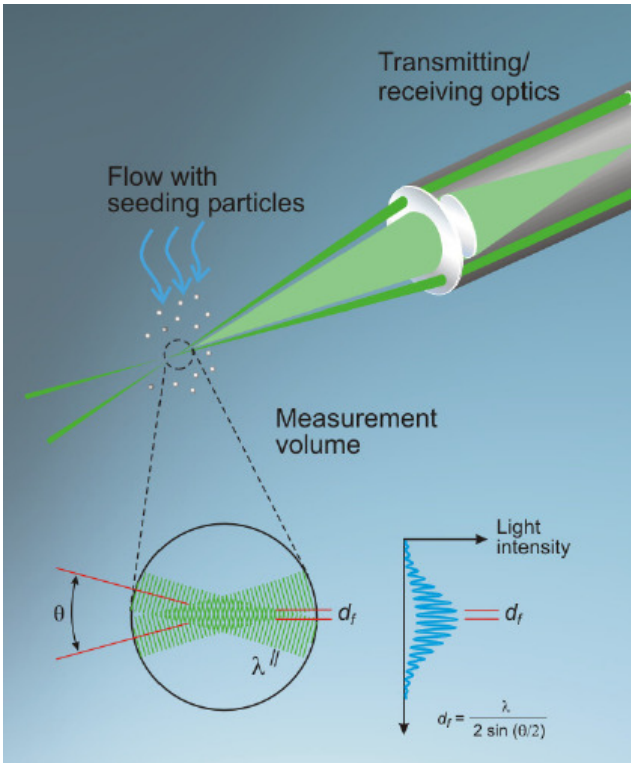


***Fig. 3.3.*** *Formation of bright and dark fringes from two coherent laser beams (from www.dantecdynamics.com).*

LDA requires no calibration since the fringe spacing, $d_f$, is set by the wavelength of laser beam and the angle between the two laser beams (*eq. 3.4*). However, LDA provides velocity time series with non-uniform time interval since the particle arrival into the measurement volume is random. Therefore, time autocorrelation and power spectra density can not be obtained directly from FFT because it requires uniform time interval. However, various methods have been developed to obtain the autocorrelation and power spectra density such as slotting method (Mayo et al., 1974; Nobach 2002) or sample and hold method (Adrian and Yao, 1987).

To differentiate the flow direction, one of the beams is given frequency shift, $f_s$, so that the fringe moves at constant velocity in the direction from shifted to unshifted beams. Using this technique, a stagnant particle generates signal with frequency equals to $f_s$, particle moves against the fringe generates signal with frequency higher than $f_s$, while particle moves in the same direction as fringe generate signal with frequency lower than $f_s$. The signal processor will then subtract the frequency shift from the received signal and the Doppler frequency is obtained.

## 3.4. Particle image velocimetry (PIV)

PIV is also a non-intrusive optical method to measure fluid velocity. Similar to LDA, it measures the velocity of seeding particles instead of the fluid itself. However, instead of using laser beams, it uses laser sheet and provide instantaneous velocity vector map in a measurement plane.

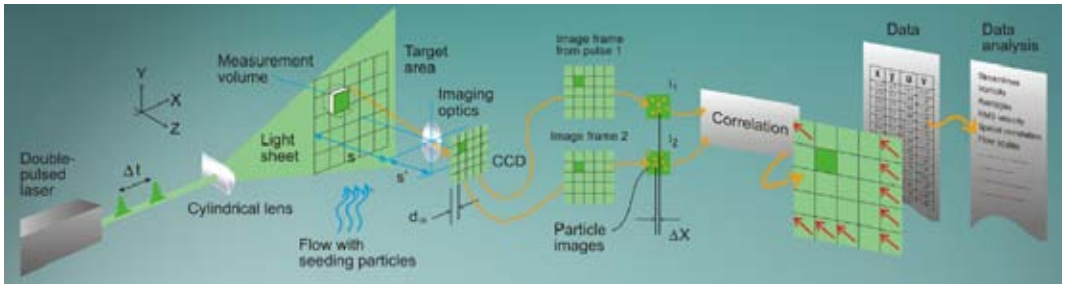


***Fig. 3.4.*** *Schematic diagram of 2D PIV (from www.dantecdynamic.com).*

The schematic diagram of 2D PIV is illustrated in *Fig. 3.4*. The light source (often dual-cavity Nd:Yag laser) emits two consecutive laser pulses in a very short time (of the order of μs) which illuminate a plane in the flow seeded by particle. The images of particles are captured by a digital camera in two separate

frames. Each image is divided into a large number of small subsections called interrogation areas. The interrogation areas in one image are cross-correlated with the corresponding interrogation areas in second image. The cross-correlation produces a signal peak indicating the average particle displacement ($\Delta x$ and $\Delta y$) expressed in pixel. The velocity components in each interrogation area can be calculated by

$$U = \frac{\Delta x}{M \Delta t} \quad \textbf{3-6}$$

$$V = \frac{\Delta y}{M \Delta t} \quad \textbf{3-7}$$

where $M$ is the image magnification expressed in pixel/m and $\Delta t$ is the time interval between two laser pulses. Therefore, one image pair produces an instantaneous velocity vector map and the time averaged velocity vectors map is obtained by averaging instantaneous velocity vectors maps from many image pairs taken over certain period of time.

To obtain a good signal peak in cross-correlation, the number of particle images in each interrogation area should be between 10 and 25 (Sheng et al., 2000). To avoid losing correlation between image pair (loss of velocity information), the particles within each interrogation area should travel less than a quarter of the length of the interrogation area within two consecutive laser pulses, i.e.

$$\frac{M U_{\max} \Delta t}{L_{IA}} < 0.25 \quad \textbf{3-8}$$

where $U_{max}$ is the maximum velocity in the investigated system and $L_{IA}$ is the length of the interrogation area. For stirred tank, the $U_{max}$ can be taken as impeller tip speed. The resolution of PIV depends on the scale of the interrogation area. The velocity vector obtained within each interrogation area is a spatial average and therefore the interrogation area acts as a filter since only length scales greater than the scale of the interrogation area are resolved (Gabriele et al., 2008).

## 3.5. Comparison between measurement devices

The measurement of velocity profile in a rotor-stator mixer is a challenging task. The rotor in a rotor-stator mixer rotates at an order of magnitude higher speed than an impeller in a stirred tank and the mixing head (the assembly of the rotor and stator) has a complicated geometry (*Fig. 1.3*). Therefore, the suitable measurement device should have high sampling rate, flexible to deal with complex geometry and not intrude the flow.

Among the measurement devices that have been discussed, CTA has the highest sampling rate but it intrudes the flow and requires calibration. Therefore it is not suitable for this experiment. Both LDA and PIV are non-intrusive, however, LDA has higher sampling rate than PIV and therefore it is more suitable to measure the flow in the proximity of the mixing head where the flow is strongly affected by rotor rotation. The sampling rate of PIV is determined by the type of digital camera used to capture the particle images. CMOS (complimentary metal oxide semiconductor) camera can capture up to thousands images per second but the image quality is rather poor and therefore can affect the cross-correlation

procedure (Li et al., 2008). However, the PIV system in the University of Birmingham uses frame-straddling CCD (charge coupled device) camera which can only capture 15 good quality image pairs per second (Gabriele et al., 2008). To overcome low sampling rate (frame rate), angle resolved measurement technique can be used, but it is very time consuming. Moreover, the reflection of laser sheet used in PIV measurement from the solid part of rotor-stator mixer creates more problem than that of laser beams used in LDA measurement. Therefore, LDA is more suitable for this work.

LDA which is a point by point measurement also gives more flexibility than PIV to measure the velocity in specific points to carry out mass and energy balances to verify CFD prediction. The flow around the mixing head is not axis-symmetric and therefore to carry out mass and energy balances, the boundaries of the control volume around the mixing head have to be discretised into small sections and the velocity is measured in the middle of each section (see Appendix A). Moreover, the energy balance requires the information regarding fluctuating component (Wu and Patterson, 1989; Zhou and Kresta, 1996) which can only be provided by LDA. From the energy balance, the average energy dissipation rate inside the mixing head can be estimated.

## 3.6. Details of LDA system

A 2D LDA system operated in a back scattered mode was used in this work. The arrangement of the LDA system is shown in *Fig. 3.5*. It consists of a

laser source, a beam separator, a laser probe, a signal receiver and a signal processor. Details of each component are explained as follows:

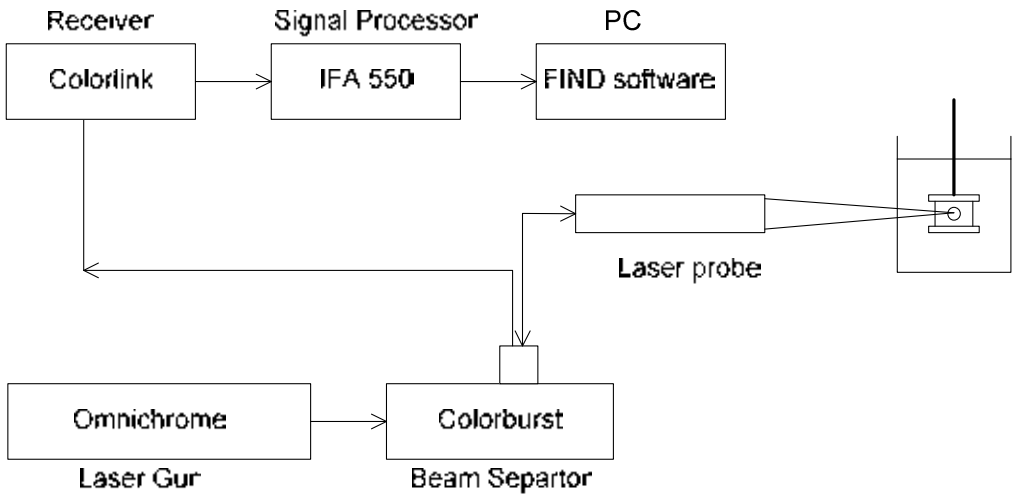


***Fig. 3.5.*** *Arrangement of 2D back scatter LDA system (TSI) used in this work.*

*Laser source*

The laser source is a 490 mW air cooled Ar-ion laser (Omnichrome, Melles Griot) which emits coherence and linearly polarized polychromatic laser beam in the visible and ultraviolet spectrum. The wave lengths range from 454 – 514.5 nm with peaks at 514.5 nm (green), 488 nm (blue) and 476.5 nm (violet).

*Beam separator*

The beam separator (TSI Colorburst 9020) consists of an accousto-optic Bragg cell and a set of prisms and mirrors. The functions of Bragg cell, which is made of SiO2 or other mineral oxides, are to divide the polychromatic laser beam into two beams with approximately the same intensity (zeroth order and first order beams) by using electronically generated ultrasonic wave (40 MHz) and to provide 40 MHz frequency shift to the first order beam (*Fig. 3.6*).

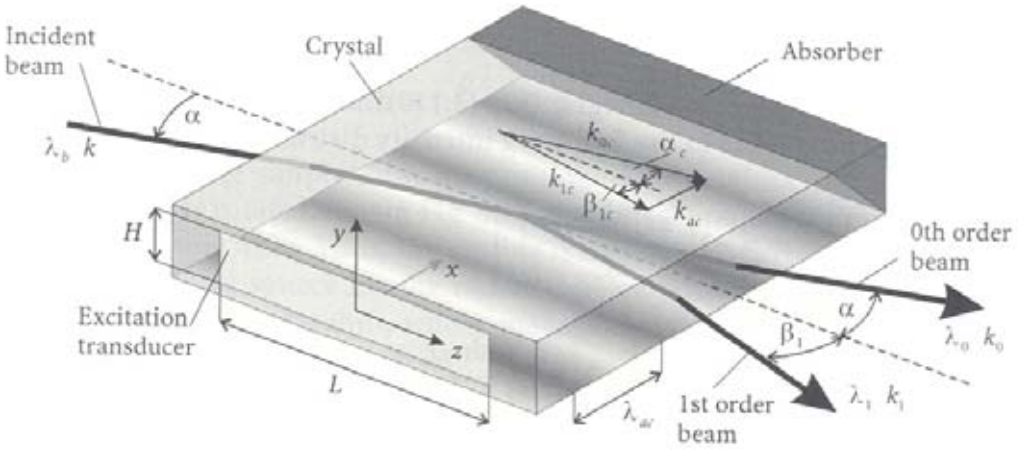


***Fig. 3.6.*** *Acousto-optic Bragg cell splits the incident beam into 0th and 1st order beams using acoustic wave and provide frequency shift to the 1st order beam (from Albredcht et al., 2003).*

A set of prisms and mirrors then separates these polychromatic beams according to their wavelengths into monochromatic beams. Three pairs of monochromatic beams with the strongest intensities (514.5 nm (green), 488 nm (blue) and 476.5 nm (violet)) are focused to optical fibers and transmitted to a fiberoptic probe. However, in this 2D LDA system, only green and blue laser beams are used.

*Fiberoptic probe*

Since the LDA system operates in a back scattered mode, the fiberoptic probe contains transmitting lens to focus the beams to form the measurement volume and also receiving lens to collect the light scattered by particles passing through the measurement volume (*Fig. 3.7*). The fiberoptic probe is mounted on a 3D computer controlled traverse which can travel in the x, y and z directions with an accuracy of 0.01 mm in each direction.

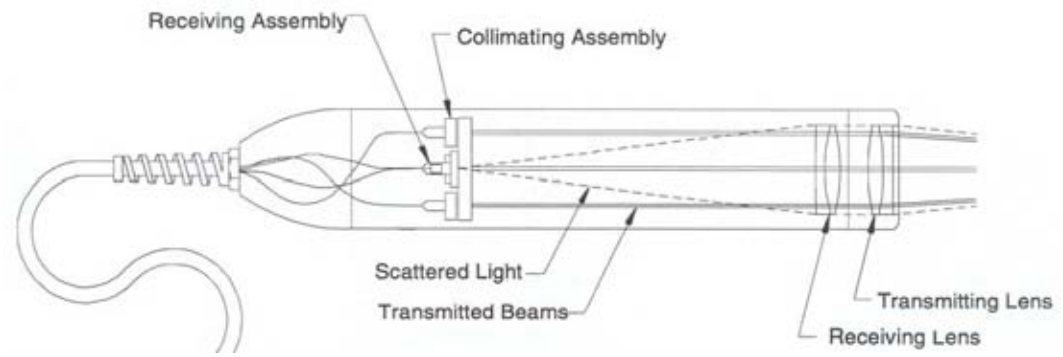


***Fig. 3.7.*** *Cross-section of a fibreoptic probe (from TSI Instruction Manual, Model 9800 Series Fiberoptic Probes).*

Two pairs of laser beams from beam separator are sent to the collimating assembly in the fiberoptic probe by using optical fibers which are able to preserve beam polarization. One pair of green laser beams lying in the horizontal plane is used to measure radial or tangential velocity component, while the other pair of blue laser beams lying in the vertical plane is used to measure axial velocity component. Those laser beams are passed to transmitting lens (F = 0.122 m) which are responsible to focus them in their waists where the wavefront is flat to form fringes with uniform spacing.

The laser beams used in LDA have a Gaussian intensity distribution. The width of the beam is usually defined by the edge where the intensity is $1/e^2$ (≈13%) of the core intensity. At one point, the Gaussian laser beam attains smallest diameter ($d_0$) and this position is called the beam waist. The wavefront is flat at the waist but spherical elsewhere with radius R as a function of the distance from the waist (*Fig. 3.8*). Therefore, when the beams intersect at their waists, they produce equally spaced fringes perpendicular to the plane where both beams lie,

but when they intersect in another place, the distances between fringes are not the same.

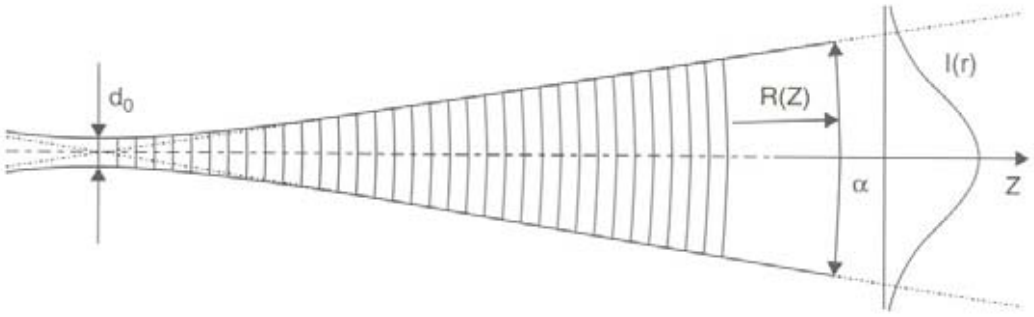


***Fig. 3.8.*** *Laser beam with Gaussian intensity distribution. The beam has smallest diameter at its waist ($d_0$) and expands with expansion degree $\alpha$ (from Papadopoulos and Arik, 2004).*

The volume where the beams intersect is called the measurement volume. Since the beams has Gaussian intensity distribution, the measurement volume has an ellipsoidal shape (*Fig. 3.9*) with dimension as follows

$$Length : \delta_z = \frac{4F\lambda}{\pi ED_L \sin(\theta/2)} \quad \textbf{3-9}$$

$$Width : \delta_y = \frac{4F\lambda}{\pi ED_L} \quad \textbf{3-10}$$

$$Height : \delta_x = \frac{4F\lambda}{\pi ED_L \cos(\theta/2)} \quad \textbf{3-11}$$

where $F$ is the focal length of the lens, $E$ is the beam expansion, $D_L$ is the initial beam thickness, $\lambda$ is the wavelength and $\theta$ is the angle between two beams. In this work, beam expander is not used and therefore E = 1.

The fringe spacing can be calculated by using *eq. 3-4* and the number of fringes, $N_f$, in the measurement volume is given by

$$N_f = \frac{8F\tan(\theta/2)}{\pi E D_L} \qquad \textbf{3-12}$$

The number of fringes in a measurement volume typically varies between 10 and 100. In this experiment, for green laser beam ($\lambda$ = 514.5 nm), the length, width and height of the measurement volume are 159.8 μm, 32 μm and 32.7 μm respectively. The number of fringe in the measurement volume is 25. The properties of the measurement volume and laser beams are summarized in Chapter IV (see *Table 1*).

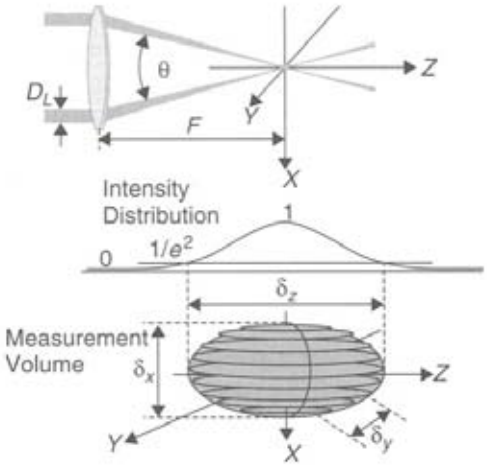


***Fig. 3.9.*** *LDA measurement volume (from Papadopoulos and Arik, 2004).*

*Signal receiver*

The light scattered by particle passing through the measurement volume, often called signal burst, is collected by receiving lens in the fiberoptic probe and sent to receiving assembly (*Fig. 3.7*). This signal is next sent to signal receiver (TSI Colorlink 9200) through optical fibre. The signal receiver separated the scattered light according to its wavelength using dichroic mirrors and notch filters into green (514.5 nm) and blue (488 nm). A photo multiplier tube converted this

light into electric signal which was then amplified and high-pass filtered (25 MHz) to remove low frequency pedestal signal which arise due to Gaussian nature of the laser beam. This signal which contained optical frequency shift (40 MHz) and Doppler frequency is then sent to frequency mixer board to be mixed with the electronically generated signal to obtain suitable frequency shift since 40 MHz frequency shift is usually too high for velocity range in this work. The signal is then low-pass filtered to remove high frequency noise and then sent to the signal processor.

*Signal Processor*

The main task of signal processor (IFA 550) is to validate the signal from signal receiver (accepted or rejected) and to extract Doppler signal from the accepted signal. The validation is based on the coherence and signal-to-noise ratio. Each zero crossing of the input signal generates a zero-crossing pulse. The validation algorithm will determine if these zero crossings are caused by a coherent signal or by random noise. The Doppler signal is determined by measuring the time for 8 Doppler cycles (TSI Instruction Manual, Model IFA 550 Signal Processor, 1988).

In this work, the velocity in each point was represented as an ensemble average of instantaneous velocity data. The number of data collected in each point was set to 30,000 in the bulk region and 40,000 in the vicinity of stator for both axial and radial velocity. The maximum acquisition time was set to 180 seconds

and the actual acquisition time varied from 40 seconds to 120 seconds. The minimal number of data collected for each velocity component was generally above 10,000. The reproducibility tests of the LDA measurements are shown in Appendix A. Zhou and Kresta (1996) suggested that minimum number of data should be greater than 6,000 to obtain good reproducibility. The error in this LDA measurement was estimated to be 3-5% of the tip velocity (Mishra et al., 1998).

Calculating mean velocity using ensemble average may introduce velocity bias or velocity broadening. When the measurement volume is located in a flow with high velocity gradient, more high speed particles pass trough the measurement volume per unit time than low speed particles. Consequently, this will introduce higher ensemble average velocity than the actual average velocity across the measurement volume. This problem can be solved by using transit time weighting (Durst et al., 1981)

$$U = \frac{\sum u_i \Delta t_i}{\sum \Delta t_i} \qquad \textbf{3-13}$$

where $\Delta t_i$ is the transit time for $i^{th}$ particle. High speed particle has shorter transit time than low speed particle. Unfortunately, IFA 550 does not record particle transit time. However, the measurement volume in this experiment is very small (about 0.16 mm in length) compared to those of Wu and Patterson (1989) and Rossinova et al. (2004) which are about 1 mm in length. It is expected that the velocity broadening can be minimized by using such small measurement volume.

# CHAPTER IV

## FLOW PATTERN, PERIODICITY AND ENERGY DISSIPATION IN A BATCH ROTOR-STATOR MIXER

This chapter has been published in Chemical Engineering Research and Design volume 86 (2008), page 1397 – 1409 and orally presented in International Symposium on Mixing in Industrial Processes (ISMIP) VI, Niagara on the Lake, Canada (17 – 21 August 2008). Some supplementary information regarding this chapter is also given in Appendix A and Appendix B.

CHEMICAL ENGINEERING RESEARCH AND DESIGN 86 (2008) 1397–1409

Contents lists available at ScienceDirect

Chemical Engineering Research and Design

journal homepage: www.elsevier.com/locate/cherd

# Flow pattern, periodicity and energy dissipation in a batch rotor–stator mixer

Adi T. Utomo[a], Michael Baker[b], Andrzej W. Pacek[a,*]

[a] Department of Chemical Engineering, University of Birmingham, B15 2TT Birmingham, UK
[b] Unilever R&D Port Sunlight, Quarry Road East, CH63 3JW Bebington, Wirral, UK

ABSTRACT

The flow pattern and the distribution of energy dissipation rate in a batch rotor–stator mixer have been investigated. Sliding mesh and standard $k$–$\varepsilon$ turbulence model were employed to predict velocity and energy dissipation rate distributions verified experimentally by the Laser Doppler Anemometry measurements. The agreement between predicted and measured bulk flow field as well as the flow pattern of jets emerging from the stator holes was very good. Results showed that the periodicity of the jet can be related to the rotor's velocity and number of blades. The energy balance based on measured velocity distribution indicated that about 70% of energy is dissipated in close proximity to the mixing head. Both simulation and measurement showed that the jet velocity and flowrate through the holes were proportional to $N$ while the energy dissipation rate scaled with $N^3$.



*Keywords:* Rotor–stator mixer; CFD; LDA; Flow field; Energy dissipation rate

## 1. Introduction

Rotor–stator mixers have been used extensively in processes requiring high energy dissipation rate per unit volume usually encountered in food, cosmetics, chemicals and pharmaceuticals industries. The typical features of these mixers are narrow gap between the rotor and stator, from 100 to 3000 μm (Karbstein and Schubert, 1995), and high rotor speed (10–50 m/s) creating a very high shear rate in the gap ranging from 20,000 to 100,000 $s^{-1}$ (Atiemo-Obeng and Calabrese, 2004). Therefore, these devices are also called high shear mixers and cover different geometries from various designs of colloid mills and toothed-devices to axial-discharge and radial-discharge rotor–stator mixers which can be operated as batch or in-line mixers (Atiemo-Obeng and Calabrese, 2004).

The performance of batch rotor–stator mixer can be related to the Reynolds number ($Re = ND^2\rho/\mu$) and the power number ($Po = P/\rho N^3 D^5$) with rotor diameter as a characteristic dimension despite the fact that there are some other length scales (gap width or hydraulic radius of the stator hole) that can be used to define those numbers (Padron, 2001).

The power curves of batch rotor–stator mixers have similar shape to that of stirred tank with the power number inversely proportional to the Reynolds number in the laminar flow regime and practically constant in the turbulent flow regime (Myers et al., 1999; Padron, 2001; Doucet et al., 2005). The laminar flow regime, indicated by the constant slope of $1/Re$ of the power curve, extends up to $Re = 100$ instead of $Re = 10$ as in the case of stirred tank. In the turbulent flow regime ($Re > 10^4$) the power number varies from 1 to 3 depending on the geometry of the rotor and stator. According to Padron (2001), the turbulent power number is not controlled by the energy dissipation in the gap, but by the fluid impingement on the stator slot surfaces or turbulence in the jets emerging from the stator slots.

2D numerical simulations of in-line rotor–stator mixer (IKA Works) were carried out by Calabrese et al. (2002) for standard ($\delta = 0.5$ mm) and enlarged ($\delta = 4$ mm) gaps with water as the working fluid. In the case of standard gap, jets were emerging from the stator slot as the fluid impinged on the leading edge of stator teeth with circulation and re-entrainments in stator slots. In the case of enlarged gap, the impingement on the leading edge of stator teeth was much weaker resulting

* Corresponding author. Tel.: +44 121 414 5308; fax: +44 121 414 5324.
E-mail address: A.W.Pacek@bham.ac.uk (A.W. Pacek).
Received 29 July 2008; Accepted 30 July 2008
0263-8762/$ – see front matter © 2008 The Institution of Chemical Engineers. Published by Elsevier B.V. All rights reserved.
doi:10.1016/j.cherd.2008.07.012

**Nomenclature**

| | |
|---|---|
| $D$ | rotor diameter (m) |
| $d_m$ | measurement volume diameter (μm) |
| $d_f$ | fringe spacing (μm) |
| $f$ | focal distance (m) |
| $Fl$ | flow number ($Q/ND^3$) |
| $l_m$ | measurement volume length (μm) |
| $N$ | rotation speed (1/s) |
| $Po$ | power number ($P/\rho N^3D^5$) |
| $P$ | power (W) |
| $Q$ | flowrate ($m^3/s$) |
| $r$ | radial direction (m) |
| $Re$ | Reynolds number ($\rho ND^2/\mu$) |
| $T$ | torque (N m) |
| $U_{rad}$ | radial velocity (m/s) |
| $U_{tan}$ | tangential velocity (m/s) |
| $U_{tip}$ | tip velocity (m/s) |
| $z$ | axial direction (m) |

*Greek letters*

| | |
|---|---|
| $\delta$ | gap spacing (mm) |
| $\varepsilon$ | turbulent energy dissipation rate per unit mass ($m^2/s^3$) |
| $\theta$ | tangential direction (°) |
| $\varphi$ | blade position relative to $\theta = 0$ (°) |
| $\kappa$ | half angle between two beams (°) |
| $\lambda$ | wave length (nm) |
| $\mu$ | viscosity (kg/m s) |
| $\rho$ | fluid density ($kg/m^3$) |

in a much lower turbulent kinetic energy. Therefore, for efficient mixing/dispersion it is necessary to have a narrow gap even if the shear in the gap is not a major contributor to the dispersion process (Calabrese et al., 2002).

In this study, a full 3D simulation verified by Laser Doppler Anemometry measurement was carried out to investigate flow pattern, pumping capacity and the distribution of energy dissipation rate in a batch radial-discharge rotor–stator mixer. The simulation was performed in the transient mode to investigate the periodic nature of the rotor–stator interaction. The prediction of the distribution of energy dissipation rate in the tank especially in the proximity of mixing head can give a better understanding on the scale-up and designs procedures.

## 2. Experimental

The rotor–stator mixer investigated in this work was a 4 LRT (Silverson) with a built-in tachometer. The rotor was a four blade impeller of diameter 28.2 mm, height 12.8 mm and thickness 5 mm. The standard disintegrating mixing head (6 holes of diameter 8 mm, gap width = 0.175 mm), was placed in the middle of an unbaffled, flat-bottom, free-surface glass beaker of diameter 150 mm. The liquid height was equal to the tank diameter and the clearance was half of the liquid height (Fig. 1). The working fluid was water, kept at 20 ± 1 °C, and the vessel was placed in a rectangular glass box also filled with water to minimize the refraction of laser beams due to the curvature of vessel wall. The rotor speed was varied from 2000 to 4000 rpm ($Re$ = 26,000–52,000).

A 2D LDA system operated in back scattered mode (TSI) was used to measure the axial and radial velocity components.

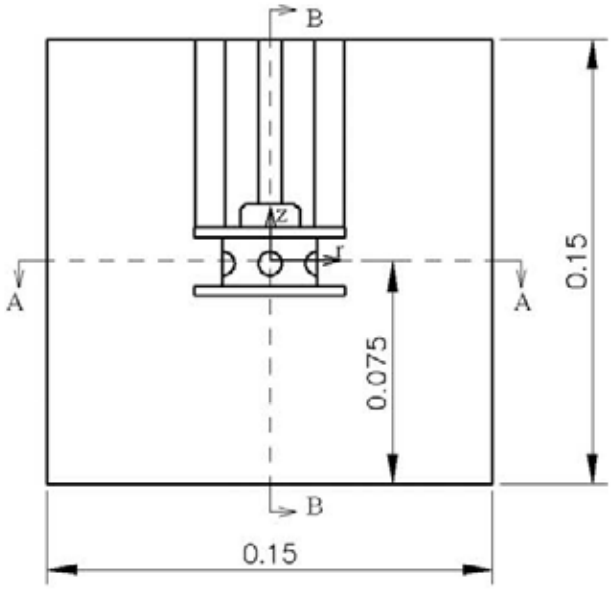


**Fig. 1 – Position of the mixing head in the vessel (dimension in m).**

The properties of laser beams and measurement volumes are given in Table 1. The laser probe was mounted on a 3D computer-controlled traverse with minimum displacement of 0.01 mm in each direction. The seeding particle was 10 μm silver coated, hollow glass sphere (Dantec). The number of data collected in each point was at least 30,000 for both axial and radial velocities and the acquisition time was from 40 to 120 s. The velocity in each point was presented as an ensemble average of instantaneous velocities.

Cylindrical coordinate system was used to describe the flow and geometry. The z-axis coincides with the vertical axis of the vessel and origin of the coordinate system is located at the midpoint between the upper and lower plates of the mixing head (Fig. 1). The angular coordinate ($\theta$) is positive in an anti-clockwise direction as viewed from above, while the rotor rotates in a clockwise direction (negative $\theta$ direction) as shown in Fig. 2. The blade position is expressed in term $\varphi$, the angle between $\theta = 0$ and the vertical plane through the middle of the blade, which is positive in the clockwise direction. The horizontal centreline of the stator hole is located slightly below the zero of z-axis at $z = 0.8$ mm.

## 3. Simulation

The computational model was a full 3D geometry consisted of about 600,000 non-uniformly distributed hybrid cells (tetrahedral and hexahedral) in the bulk tank region and about 400,000

**Table 1 – Properties of laser beams and measurement volumes**

| | | |
|---|---|---|
| Laser beam | | |
| Wavelength ($\lambda$) | 514.5 nm (green) | 488 nm (blue) |
| Half angle ($\kappa$) | 11.563° | 11.563° |
| Focal distance ($f$) | 0.122 m | 0.122 m |
| Measurement volume | | |
| Fringe spacing ($d_f$) | 1.283 μm | 1.213 μm |
| Diameter ($d_m$) | 32.70 μm | 31.01 μm |
| Length ($l_m$) | 159.81 μm | 157.91 μm |

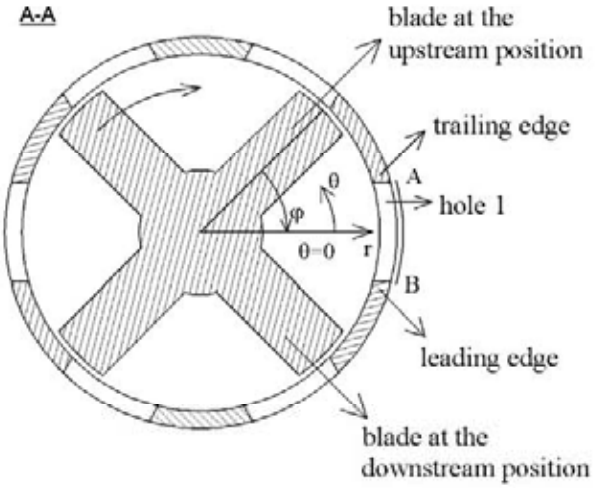


**Fig. 2 – Horizontal cross section of mixing head (plane A–A in Fig. 1, $z = -8 \times 10^{-4}$ m) which also shows the coordinate system and terms used in this discussion.**

hybrid cells inside the rotor–stator region (Fig. 3(a)). The presence of pins holing top and bottom plates of the mixing head together was also accounted for. The gap between rotor and stator was divided into 5 hexahedral cells and the interface

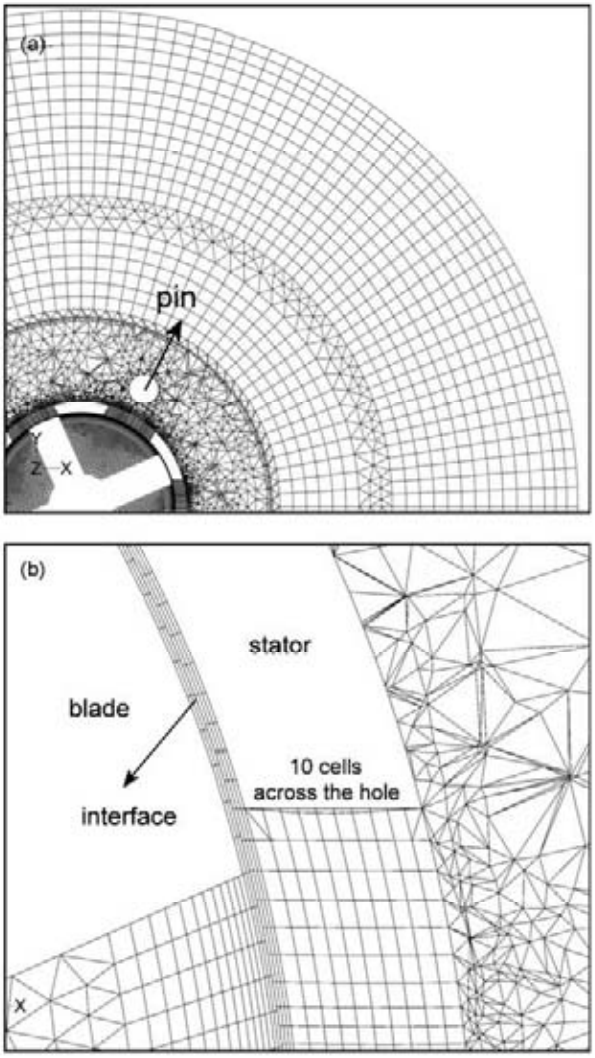


**Fig. 3 – (a) Grids used in the simulation and (b) detail of the grids around the mixing head.**

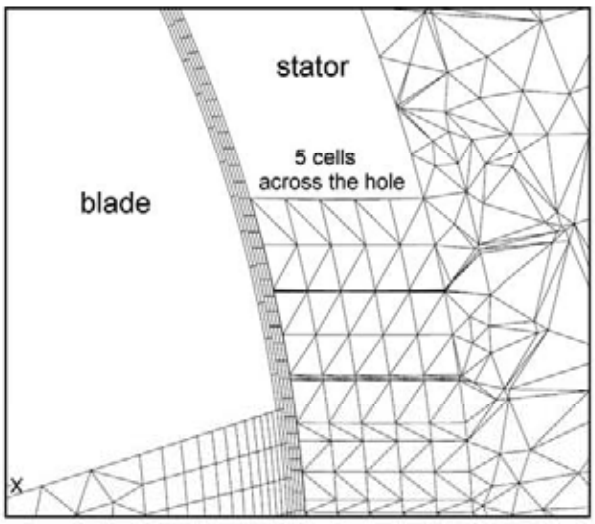


**Fig. 4 – Previous CFD model with 5 prism cells across the hole (from Pacek et al., 2007).**

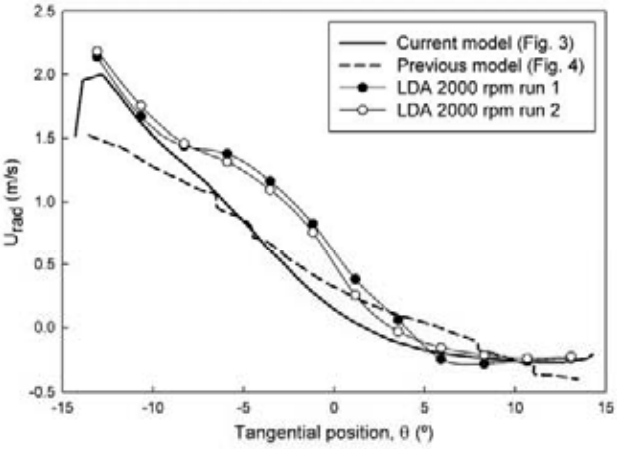


**Fig. 5 – Comparison of prediction of time averaged jet radial velocity (line AB Fig. 2, 2000 rpm) between current and previous CFD models.**

between rotating and stationary frames is located at the middle of the gap (Fig. 3(b)).

The density of computational cells (number of computational cells per tank volume) in the bulk region is approximately the same as Roussinova et al. (2003) and Bakker and Oshinowo (2004) (500–600 thousand computational cells) in simulation of the flow in stirred tanks of diameters between 0.2–0.29 m using large eddy simulation (LES).

The simulation was run in Fluent 6.2, started with steady state multiple reference frames and then continued with transient sliding mesh. Standard $k$–$\varepsilon$ model was used to model the turbulence and enhanced wall function, which can describe the flow in viscous sublayer, buffer region and fully turbulent outer region of boundary layer, was applied at the wall boundary condition (Fluent User's Guide, 2004). QUICK differencing scheme was used to discretized the convection terms while second order implicit scheme was used for time advancing. The pressure and convection terms were coupled using SIMPLE algorithm. The time step in the transient sliding mesh simulation was 1/60 of the rotor revolution time. In each time step, the solution converged with residuals below $10^{-3}$ which

took about 15 min CPU time. The simulation was run until there was no further change in bulk flow pattern which took 50 revolutions. For transient simulation in stirred tanks, Ng and Yianneskis (2000) and Roussinova et al. (2003) reported that converged solutions were usually obtained around 10 and 20 impeller revolutions for RANS simulation and LES respectively.

Compared to previous work (Pacek et al., 2007), the number of computational cells in the stator holes (where the jets emerge and hence where the largest velocity gradient occurs) in this work has been doubled (Figs. 3 and 4) and the time step has been refined from 1/30 to 1/60 of rotor revolution time. However, this only gives slightly better prediction in terms of time averaged jet radial velocity (Fig. 5) and practically gives no improvement in terms of flowrate. Therefore, the number of computational cells and the time step were not refined further.

## 4. Results and discussions

### 4.1. Flow pattern in the tank

The velocity vectors around the disintegrating mixing head and bulk region at plane $z = -8 \times 10^{-4}$ m (cross section A–A in Fig. 1) are shown in Fig. 6(a) and (b) respectively. The flow pattern is rather complex due to the presence of high velocity jets and recirculation loops induced by those jets. The jets result from the change of direction in momentum flux from tangential to radial as fluid impinges on the surface of the stator. They extend up to the tank wall where they are converted back into tangential flux creating circulation in the tank.

In contrast to the flow pattern around the mixing head, the velocity profiles at horizontal planes above and below the mixing head are dominated by circulation flow typical for unbaffled vessels as illustrated in Fig. 7(a) and (b). There are small circulation loops near the tank wall which are induced by the jets.

Calculated (CFD) and measured (LDA) radial-axial velocity vectors at plane $\theta = 0$ (cross section B–B in Fig. 1) are compared in Fig. 8. The qualitative agreement between simulation and measurement is very good and in both cases circulation loops at the regions above and below the mixing head are very similar. The simulation shows the centers of circulations loops are located at $z = 0.045$ m and $z = -0.05$ m for upper and lower loops respectively (points A and B in Fig. 8(a)), while the measurement shows that the centers of loops are at $z = 0.045$ m and $z = -0.045$ m for upper and lower loops respectively (points A* and B* in Fig. 8(b)).

In the middle of the tank two streams of liquid flow in the opposite direction, one flows toward the stator hole and the other flows toward the wall. At the plane $\theta = 0$ (middle of the hole) the velocity vectors toward the stator hole shown in Fig. 8 represent the circulation flow behind the jet and the velocity vectors of the jet itself are not captured. The magnitudes of velocity vectors towards the stator are well predicted, however, the magnitudes of velocity vectors towards the wall are underpredicted.

The time averaged radial velocity profiles of the jet (normalized by tip speed) at different rotor speeds shown in Fig. 9 indicate that the maximum jet radial velocity occurs at the leading edge ($\theta = -14°$) and decreases gradually with the distance from the leading edge. At some point the radial velocity takes negative value indicating a recirculation region where the liquid flows into the hole (Fig. 6(a)). The measurement data was taken along line AB (Fig. 2) which was located 0.3 mm off the stator.

Fig. 9 also shows simulation results at 2000 and 4000 rpm. The jet radial velocity was averaged over 90° blade rotation (15 time steps). The simulation results give similar trend to the measurement data. The time averaged radial velocity around the leading and trailing edges are very well predicted, but in the middle of the hole where jet and recirculation flow may

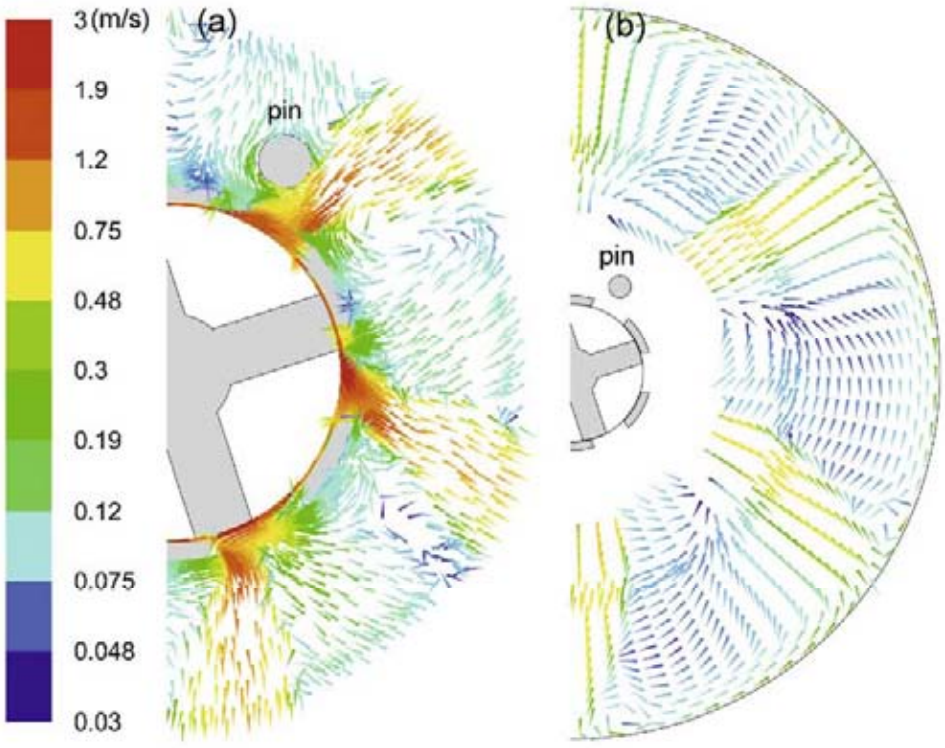


**Fig. 6 – Prediction of radial–tangential velocity vectors at plane $z = -8 \times 10^{-4}$ m (cross section A–A in Fig. 1) at 2000 rpm, (a) around the mixing head and (b) in bulk region. Vectors are plotted in constant length.**

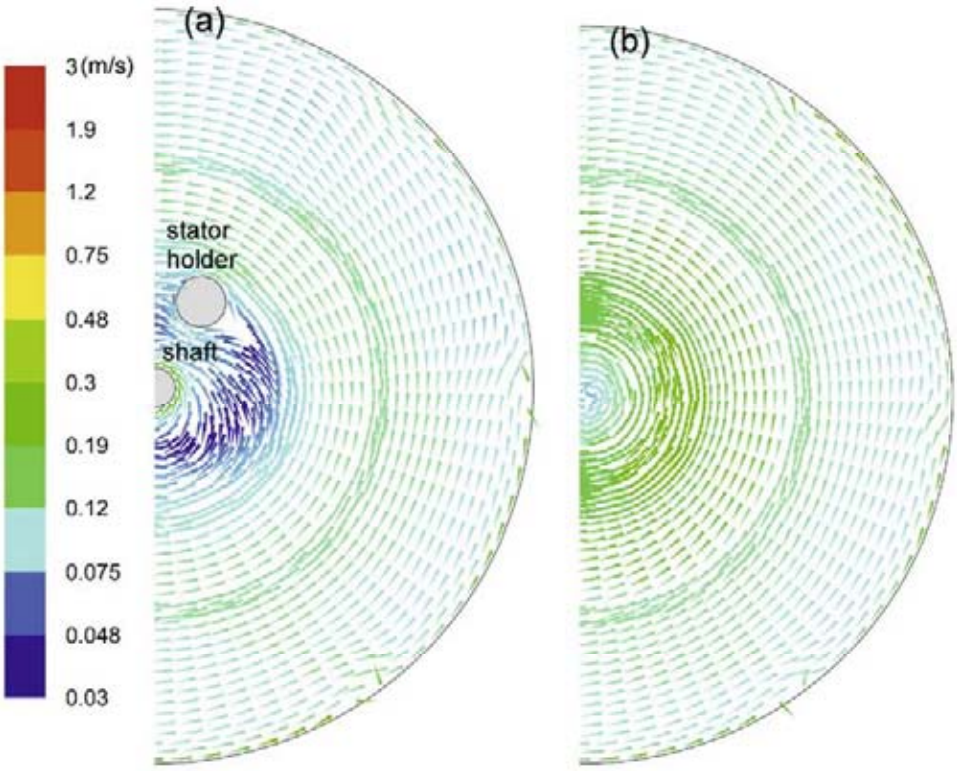


**Fig. 7 – Prediction of radial–tangential velocity vectors at (a) above the mixing head (z = 0.04 m) and (b) below the mixing head (z = −0.040 m). Vectors are plotted in constant length.**

occur together, the velocity is underpredicted. Both measurement and simulation results show that the time averaged radial velocity of the jet is proportional to rotor tip speed as the normalized radial velocities at various rotor speed collapse into single line.

The time averaged tangential velocity of the jet (normalized to tip speed) is shown in Fig. 10. Similar to the radial velocity, it is also proportional to the rotor speed and reaches maximum (absolute), which is only one third of the maximum of radial velocity component, at about 10° before the leading edge. At

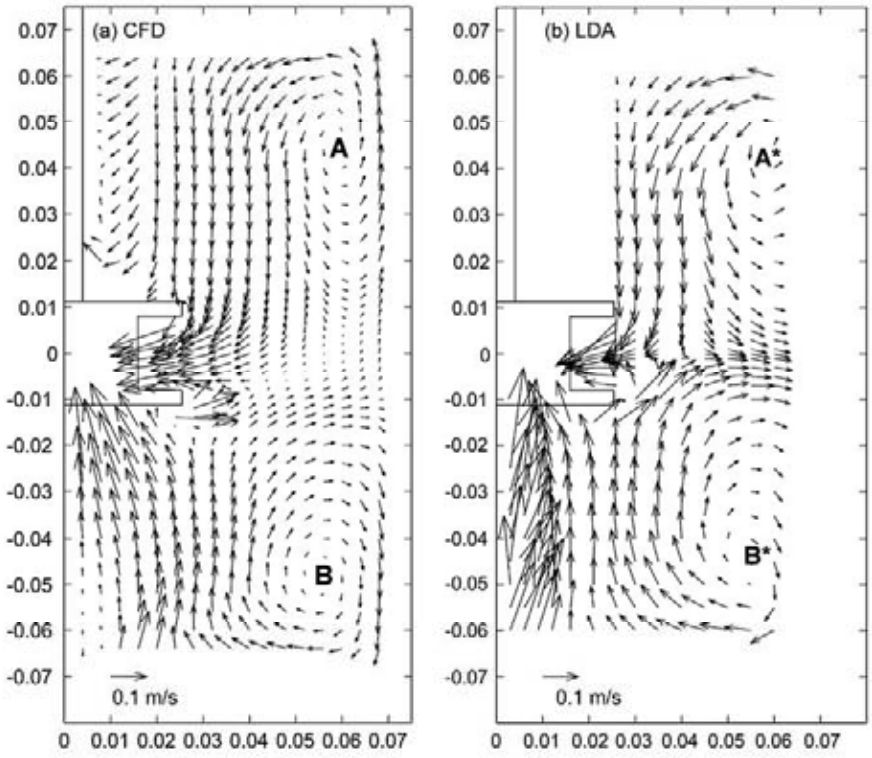


**Fig. 8 – Axial-radial velocity vectors at plane $\theta = 0$ (cross section B–B in Fig. 1) at 2000 rpm, (a) standard $k$–$\varepsilon$ model and (b) LDA measurements (dimensions in m). Points A and B represent the centers of upper and lower circulation loops of CFD prediction respectively while points A* and B* represent those of LDA measurement.**

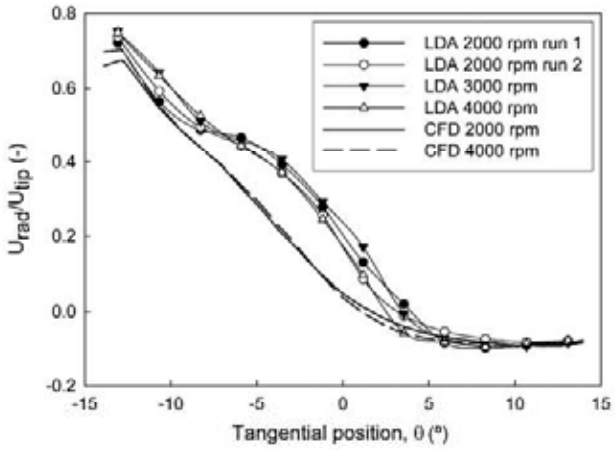


**Fig. 9 – Normalized (by tip speed) time averaged radial velocity profiles along line AB (Fig. 2) at various rotor speeds. The leading edge is at $\theta = -14°$ and trailing edge is at $\theta = 14°$.**

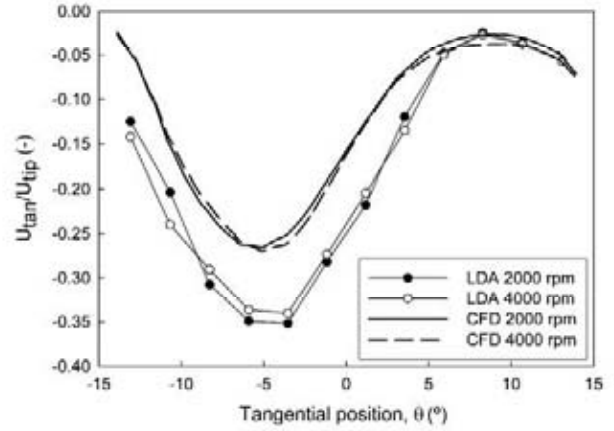


**Fig. 10 – Normalized (by tip speed) time averaged tangential velocity profiles along line AB (Fig. 2) at various rotor speeds. The rotor moves in negative $\theta$ direction.**

the leading edge the tangential velocity is practically zero as most of tangential momentum flux is converted into radial momentum flux as the fluid impinges on the surface of the leading edge.

### 4.2. *Autocorrelation and power spectrum density of LDA data*

As the blades move periodically across the holes, the flow patterns around the holes also exhibit a periodic behavior which is confirmed by LDA data. The time autocorrelation function (ACF) of the LDA data taken at a point in the proximity of the leading edge of hole 1 (point B in line AB Fig. 2, 2000 rpm) shows a periodic fluctuation (Fig. 11) and the Fourier transform of the ACF, i.e. the power spectral density (PSD), indicates that this periodic behavior has a dominant frequency at 137 Hz which is practically the same as the blade passing frequency which is 133.3 Hz at 2000 rpm (Fig. 12). This confirms that the jets emerges from the stator holes have a periodic nature with the same frequency as blade passing frequency.

The ACF and the PSD of the LDA data were obtained by using a code provided by Nobach (http://www.nambis.de). The ACF was calculated by using fuzzy slotting technique with local time estimation (Nobach, 2002) while the PSD was

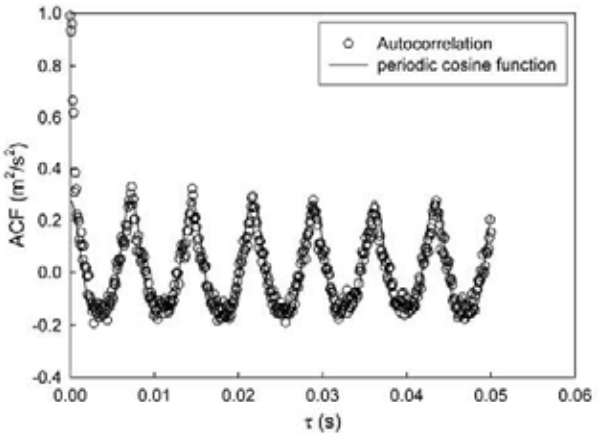


**Fig. 11 – The time autocorrelation function (ACF) of the LDA data (radial velocity component, 2000 rpm) taken at point B (Fig. 2).**

obtained from the ACF by using continuous Fourier transform and variable windowing (Tummers and Passchier, 1996; Nobach, 2002).

### 4.3. *Periodicity of velocity and flowrate around the hole*

The flow pattern of the jet depends on the blade position relative to the hole as shown in Fig. 13. Regardless the blade position, the jet always generated at the leading edge, while the circulation takes place at the trailing edge. Fig. 14 shows the radial velocity along line AB in Fig. 2 at various blade positions. As the blade approaching the leading edge, the jet radial velocity at the leading edge increases and the circulation area widens as the blade blocks the liquid in the rotor swept volume to pass through the hole.

The radial velocity at the leading edge fluctuates from 1.6 to 2.3 m/s at 2000 rpm as the blade moves across the hole as shown in Fig. 15. The radial velocity increases as the rotor approaches the leading edge and reaches maximum just before the blade touches the leading edge, recovers when they overlap, and finally decreases when the blade moves away from the leading edge.

Fig. 15 also shows the fluctuation of mass flowrate through hole 1 (Fig. 2) at 2000 rpm as a function of the blade position.

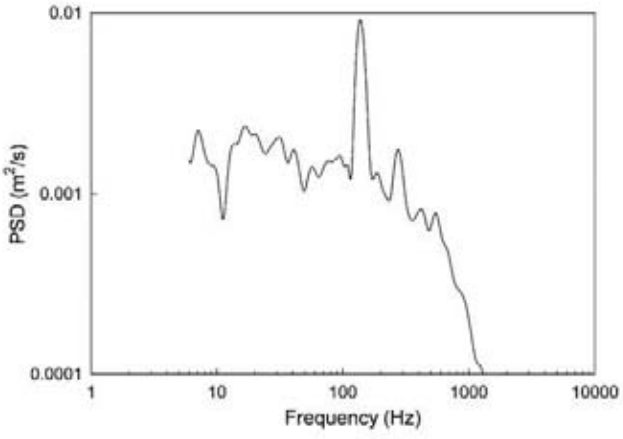


**Fig. 12 – The power spectra density (PSD) of the LDA data (radial velocity component, 2000 rpm) taken at point B (Fig. 2).**

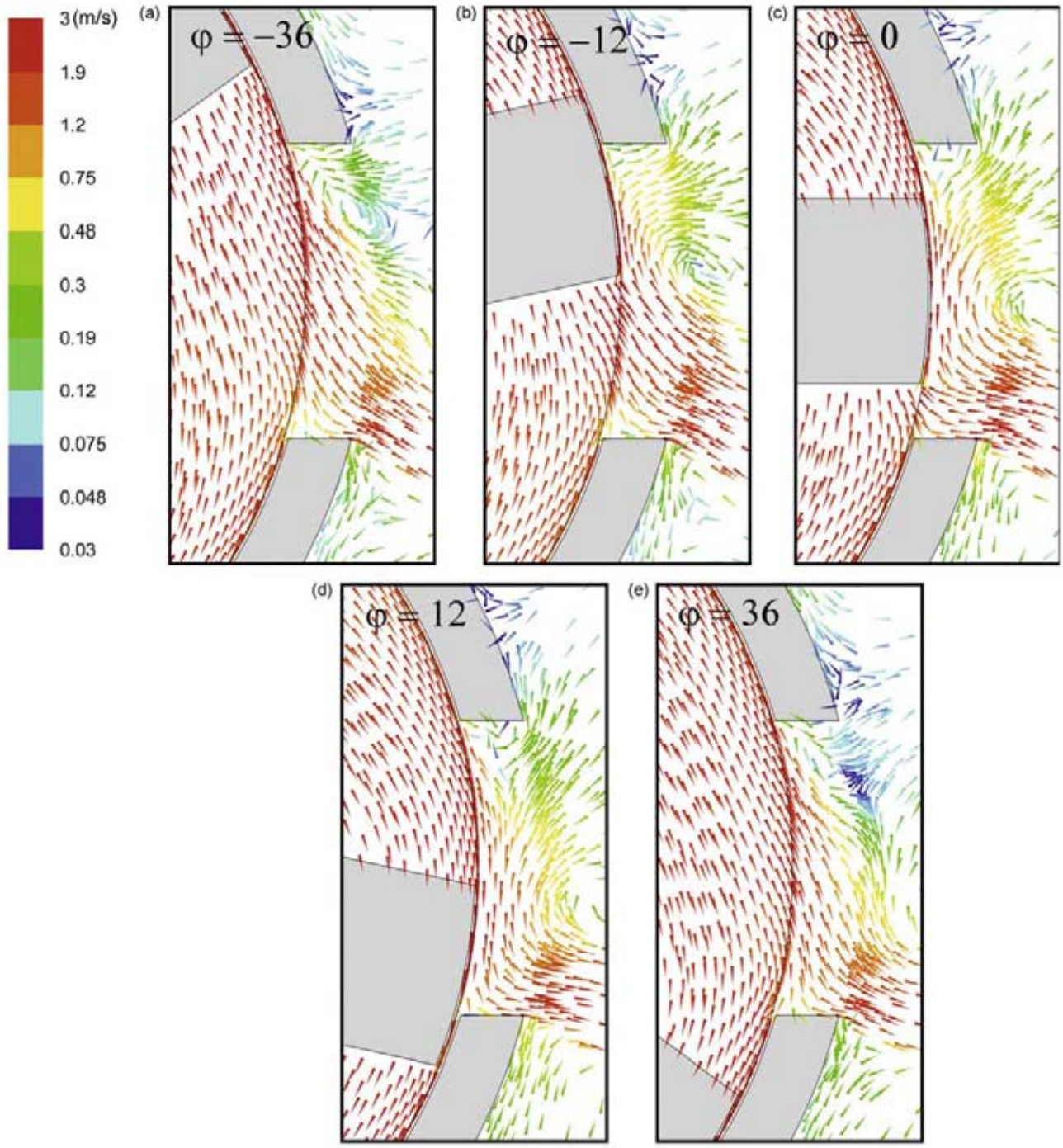


**Fig. 13 – Prediction of velocity vectors around the stator hole at various blade positions (2000 rpm).**

The maximum mass flowrate, 0.031 kg/s, occurs when the blade does not overlap with the hole and the minimum, 0.008 kg/s, occurs when the blade is near the leading edge, as it blocks the liquid from the rotor swept volume to pass through the hole (Fig. 13). Hence, the maximum mass flowrate occurs when the jet radial velocity is low, and on the other hand, when the jet radial velocity reaches its maximum value, the mass flowrate reaches its minimum value.

### 4.4. *Flowrate and the flow number*

The predicted time averaged mass flowrates through hole 1 (Fig. 2) at 2000 and 4000 rpm are 0.0212 kg/s and 0.0411 kg/s, while the flowrates based on LDA data are 0.027 kg/s and 0.053 kg/s for 2000 and 4000 rpm respectively. These predicted values are about 20% lower than the measured values which are in line with lower jet radial velocity in the middle of the hole predicted by simulation.

Fig. 16 shows that the flowrate through stator holes is proportional to the rotor speed as is the velocity. Since *Re* and *Po* in the batch rotor–stator mixer can be defined as those in the stirred vessel (Padron, 2001), it is reasonable to define the flow number (*Fl*) in a batch rotor–stator mixer in same way as that in the stirred vessel (Dyster et al., 1993)

$$Fl = \frac{Q}{ND^3} \tag{1}$$

where Q is the volume flowrate through stator holes and *D* is the rotor diameter. Fig. 17 shows the flow number in a

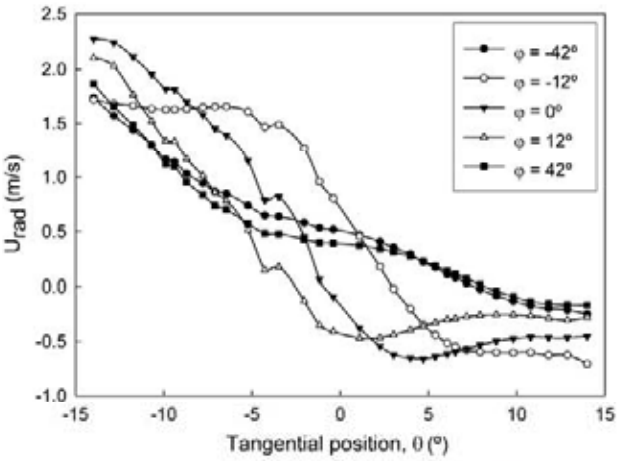


**Fig. 14 – Radial velocity profile along line AB in Fig. 2 at various blade positions at 2000 rpm ($\theta = -14$ and $\theta = 14$ correspond to points B and A respectively).**

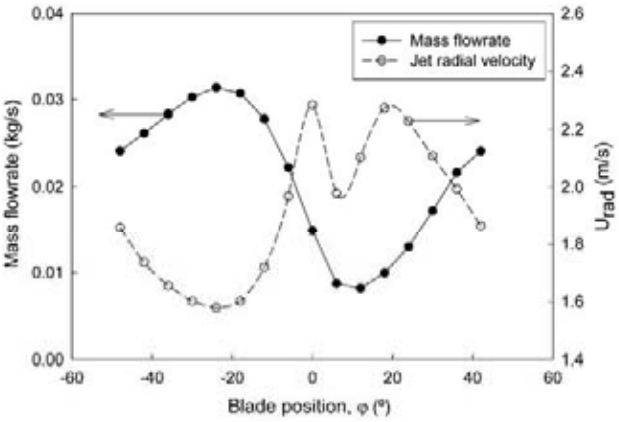


**Fig. 15 – Fluctuation of radial velocity at the leading edge (point B) and mass flowrate through hole 1 (Fig. 2) as a function of blade position. The blade overlaps with the leading edge between $\varphi = 6°$ and 26°.**

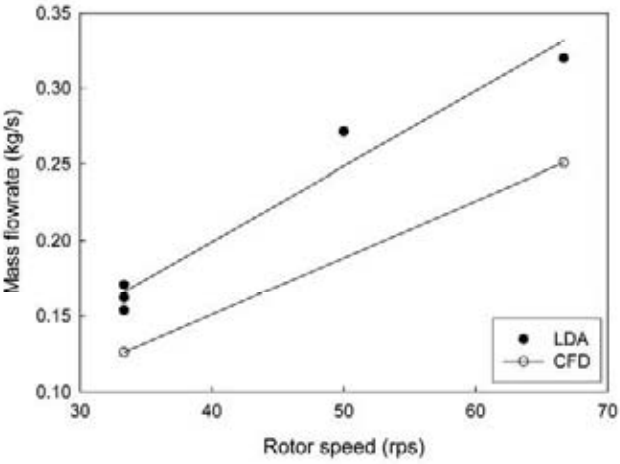


**Fig. 16 – Time averaged mass flowrate through stator holes.**

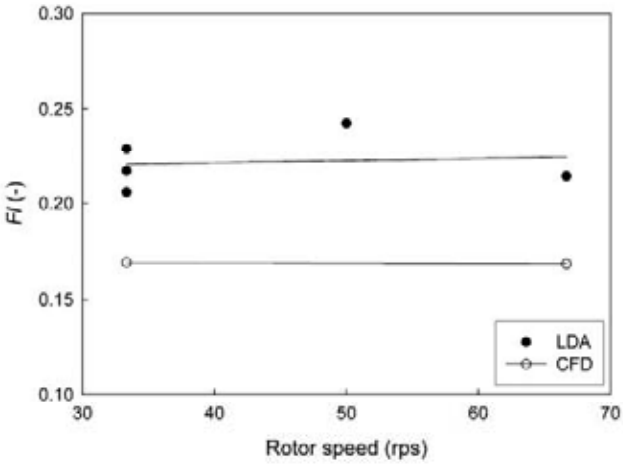


**Fig. 17 – The flow number (Fl).**

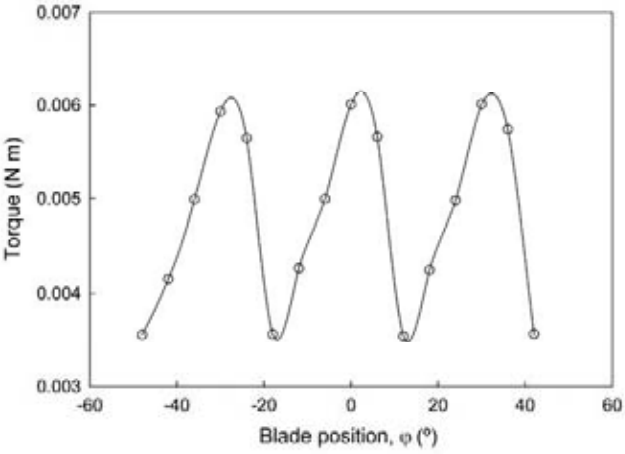


**Fig. 18 – Fluctuation of the torque as a function of blade position at 2000 rpm (CFD simulation).**

batch rotor–stator mixer is constant at 0.217 in the range of 2000–4000 rpm, while the predicted Fl is 0.176. This flow number is less than 30% of that for the Rushton turbine e.g. 0.78 (Dyster et al., 1993).

### 4.5. *Torque and the power number*

The simulation indicates that the torque in the rotor–stator mixer fluctuates as the blade rotates as shown in Fig. 18. This torque fluctuation can be related to the flowrate fluctuation (Fig. 15). When the blade moves toward the hole (the hole is fully open), it pushes more liquid through the hole then when it moves toward the stator wall (the hole is partially blocked). As a consequence, more torque is required when the blade moves toward the hole than when it moves toward the wall.

The cycle of torque fluctuation is approximately 30°, the same as the cycle of blade passing the hole as shown in Fig. 19 and the amplitude of torque varies from 0.00356 to 0.00601 N m at 2000 rpm. The time averaged torques are 0.00489 N m and 0.0198 N m at 2000 and 4000 rpm respectively. The power, P, required to turn the rotor:

$$P = 2\pi NT \quad (2)$$

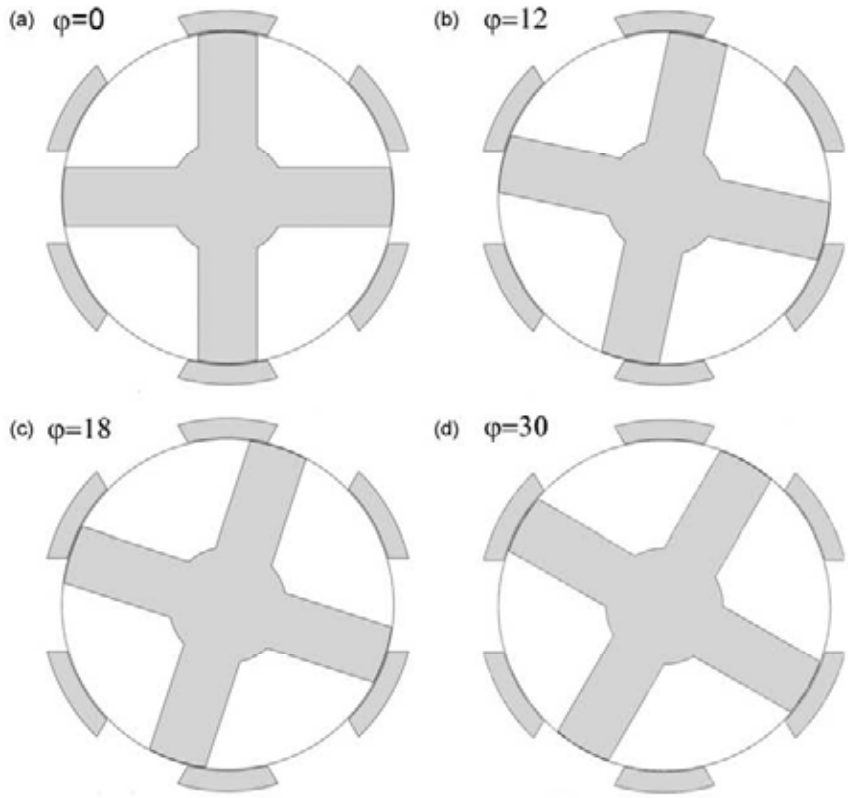


**Fig. 19 – Position of the blades relatives to the holes repeats every 30°.**

and the power number, Po, can then be calculated from (Shekkar and Jayanti, 2002)

$$Po = \frac{P}{(\rho N^3 D^5)} \quad (3)$$

The predicted power numbers based on the above equations are 1.55 and 1.57 for 2000 and 4000 rpm respectively, and they are in very good agreement with experimental Po = 1.7 (Padron, 2001).

### 4.6. *Distribution of the energy dissipation rate*

The contours of normalized energy dissipation rate (simulation) at a horizontal plane through the centre of the hole ($z = -8 \times 10^{-4}$ m) are shown in Fig. 20(a) and (b) for 2000 and 4000 rpm respectively. The similarity of normalized energy dissipation rate profiles between 2000 and 4000 rpm suggests that the energy dissipation rate in the rotor–stator mixer is proportional to $N^3D^2$, similar to that in the mixing tank.

Fig. 20 also shows that the energy dissipation rate in the rotor swept volume is only at a moderate intensity. An order

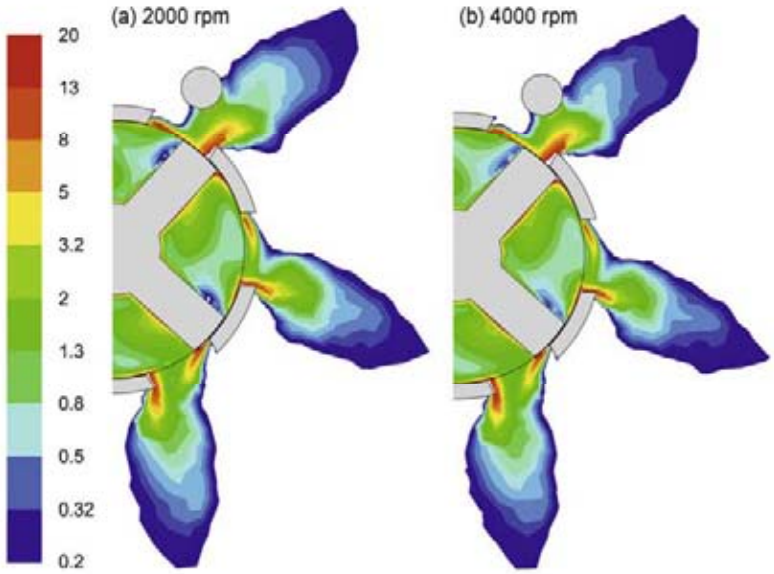


**Fig. 20 – Prediction of normalized energy dissipation rate (by $N^3D^2$) around the mixing head at (a) 2000 rpm and (b) 4000 rpm.**

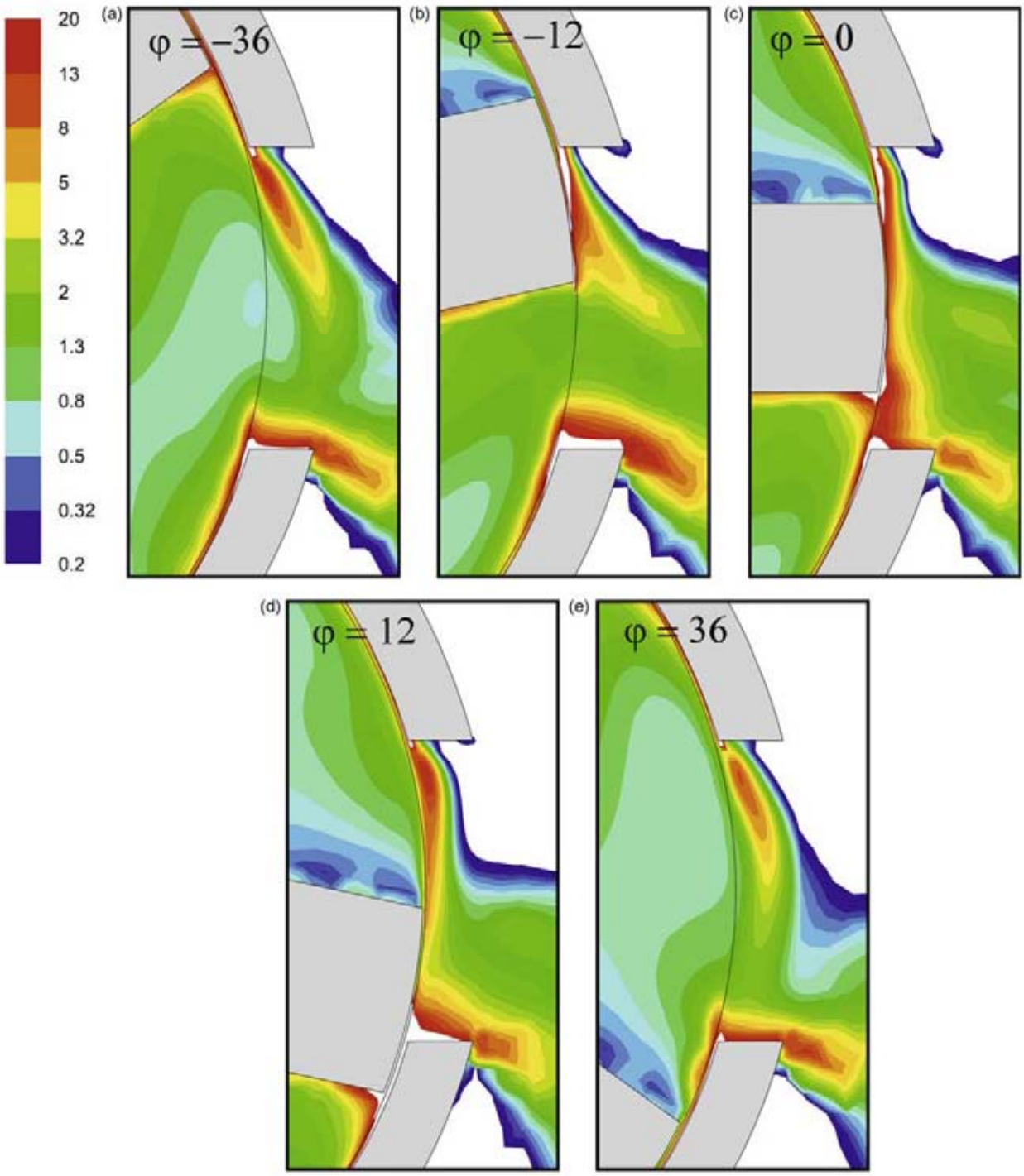


**Fig. 21 – Prediction of energy dissipation rate (normalized by $N^3D^2$) around the hole at 4000 rpm. The white areas represent energy dissipation rate (normalized) lower than 0.2 or higher than 20.**

of magnitude higher energy dissipation rate occurs around the leading and trailing edges of the holes due to stagnation of fluid on those edges. However, this high energy dissipation rate is confined to the part of jet close to the stator.

Since the energy dissipation rate around the holes edges is related to the fluid velocity, its magnitude is also affected by the blade position relative to those edges, although its order of magnitude is practically constant regardless the blade position (Fig. 21). The highest energy dissipation rate occurs in relatively small volume of fluid when the blade overlaps with the leading edges Fig. 21, $\varphi = 12^\circ$). This could lead to a longer processing time when homogenously dispersed product is required.

High energy dissipation rate is also predicted on the stator wall which also can be related to the stagnation of fluid (Figs. 22 and 23). The normalized energy dissipation rate on the stator wall is slightly higher when the blade overlaps with the stator wall and it is also slightly higher at 4000 rpm than at 2000 rpm.

The calculated tangential velocity profiles in the proximity of stator wall (normalized to tip speed) at 2000 and

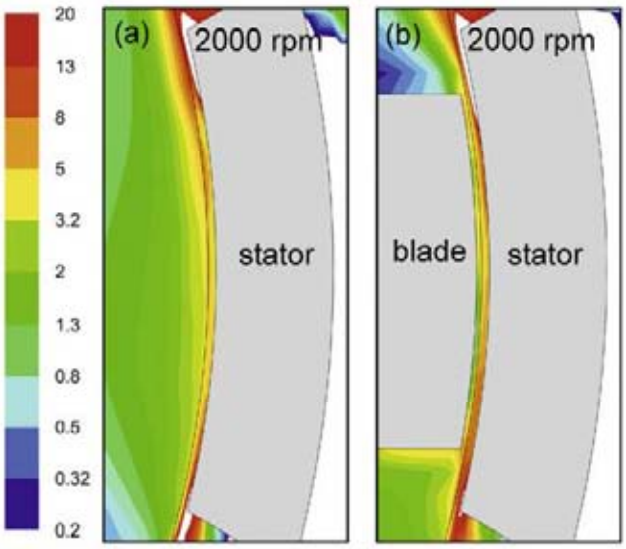


**Fig. 22 – Prediction of normalized energy dissipation rate on the stator wall at 2000 rpm (a) in the absence and (b) in the presence of blade. The white areas represent energy dissipation rate (normalized) lower than 0.2 or higher than 20.**

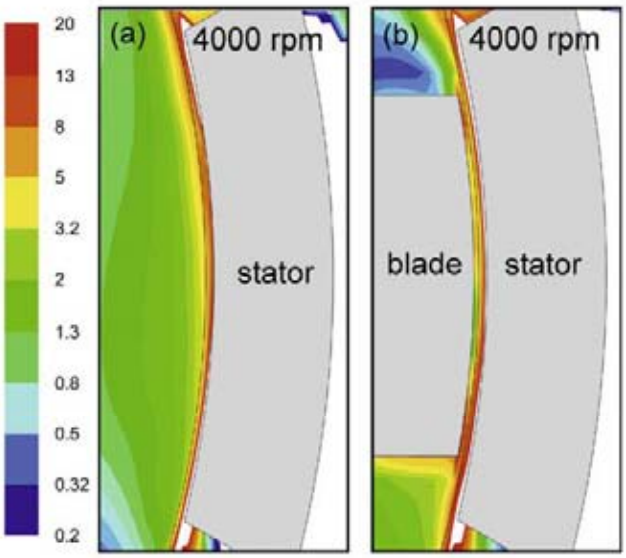


**Fig. 23 – Prediction of normalized energy dissipation rate on the stator wall at 4000 rpm (a) in the absence and (b) in the presence of blade. The white areas represent energy dissipation rate (normalized) lower than 0.2 or higher than 20.**

4000 rpm indicate the presence of boundary layer near the wall (Fig. 24). The simulation suggests that the flow in the gap, i.e. when the blade overlaps with the stator wall, is turbulent since the velocity profiles in the proximity of the wall are not affected by blade passage. However, further work with refined mesh and different location of grid interface (between rotating and stationary meshes) is required to see if the velocity profile in the gap is sensitive to the location of the grid interface or not. The tangential velocity profile near the wall at 4000 rpm, either in the presence or absence of the blade, has a slightly steeper slope than that at 2000 rpm leading to slightly higher energy dissipation rate near the wall (Figs. 22 and 23).

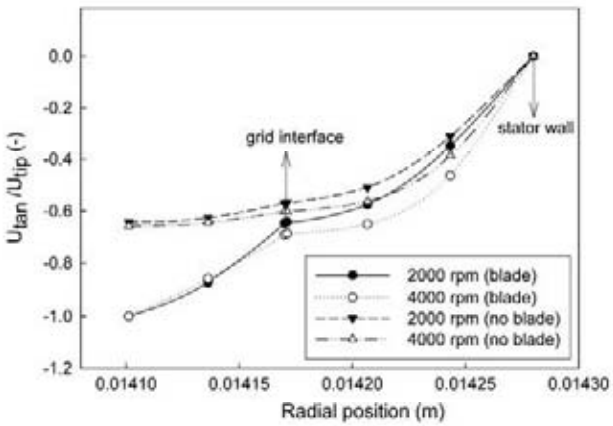


**Fig. 24 – Normalized (by tip speed) tangential velocity profiles in the proximity of stator wall ($\theta = 90°$, $z = -8 \times 10^{-4}$ m) at 2000 and 4000 rpm, in the presence or absence of the blade. The rotor moves in negative $\theta$ direction and the impeller tip is at $r = 0.0141$ m.**

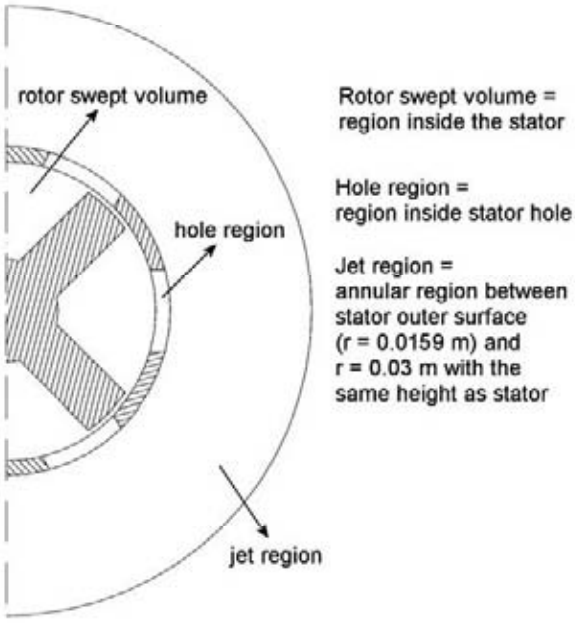


**Fig. 25 – Definition of regions in the rotor–stator mixer.**

Prediction of the amount of energy dissipated in various regions in the tank (Fig. 25) is shown in Table 2 which indicates that most of the energy (48.5%) is dissipated in the rotor swept volume and only a small fraction of energy is dissipated

**Table 2 – Predictions of distributions of energy dissipated in the tank at 2000 and 4000 rpm**

| Region | 2000 rpm | 4000 rpm |
|---|---|---|
| Rotor swept volume | 0.368 W (48.5%) | 3.037 W (48.5%) |
| Hole region | 0.058 W (7.6%) | 0.488 W (7.8%) |
| Jet region | 0.157 W (20.7%) | 1.317 W (21.0%) |
| Rest of the tank | 0.176 W (23.1%) | 1.426 W (22.8%) |
| Total energy dissipated | 0.759 W (100%) | 6.268 W (100%) |
| Total energy dissipated/$Po\rho N^3D^5$ [a] | 67.8% | 69.9% |

[a] $Po\rho N^3D^5$ is the actual power input into the system, $Po = 1.7$ (Padron, 2001).

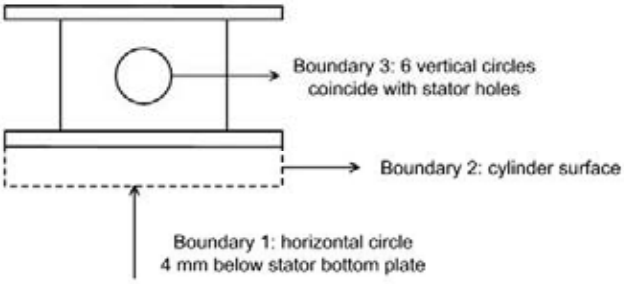


**Fig. 26 – Control volume around the mixing head for mass and energy balances.**

in the hole region (7.6%). It has been reported that $k$–$\varepsilon$ model underpredicts energy dissipated in the stirred tank by as much as 50% (Ng and Yianneskis, 2000; Yeoh et al., 2004) but Ng and Yianneskis (2000) found that calculated distribution of energy dissipated in the mixing tank using $k$–$\varepsilon$ model is similar to the experimental data by Zhou and Kresta (1996).

The amount of energy dissipated around the mixing head can be determined experimentally from energy balance over a control volume shown in Fig. 26. The boundaries of control volume were discretized into small elements (Pacek et al., 2007) and the liquid velocity in the center of each element was measured allowing calculation of kinetic energy balance (Wu and Patterson, 1989; Zhou and Kresta, 1996).

The kinetic energy balances based on LDA data at 2000 and 4000 rpm show that about 70% of energy is dissipated in the control volume compared to about 60% predicted by the simulation. The energy balances also show that the amount of energy dissipated in the control volume increase by a factor of eight when the rotor speed is doubled from 2000 to 4000 rpm suggesting that the energy dissipation rate is proportional to $N^3$.

## 5. Conclusions

The flow field in a batch rotor–stator mixer has been analyzed theoretically and experimentally with very good agreement between theory and experiment. Both simulation and measurement indicated that the jet radial and tangential velocities as well as flowrate are proportional to $N$ and the energy dissipation rate scales with $N^3$, similar to those in stirred vessels.

The periodicity in the rotor–stator mixer is related to the blade passing frequency and jet velocity profile, flowrate, torque and energy dissipation rate are affected by the blade position relative to the stator edges.

The highest energy dissipation rate occurs around the holes edges. However, the energy dissipated in the hole region is only 7.6% of the total energy supplied by rotor. Most of energy is dissipated in the rotor swept volume. The energy dissipation rate in the bulk region is several orders of magnitude lower than that in the hole region what, in conjunction with periodicity and poor bulk mixing, can lead to a longer processing time to achieve product homogeneity.

The simulation predicts that the flow in the gap is turbulent rather than laminar since the tangential velocity profile in the gap is non-linear indicating the presence of boundary layer at the stator wall. This boundary layer is practically not affected by blade rotation and the energy dissipation rate in the gap practically scales with $N^3D^2$. Therefore, this study suggests that in the turbulent regime, scale-up procedure should be based on the constant energy dissipation rate per unit mass ($N^3D^2$) and geometry similarities rather than constant tip speed ($ND$) and constant gap width (Atiemo-Obeng and Calabrese, 2004). The rotor speeds scale-up with $D^{-1}$ and $D^{-2/3}$ based on constant tip speed and constant energy dissipation rate procedures respectively. Hence, scale-up procedure based on constant tip speed gives lower rotor speed compared to that based on $N^3D^2$ which could lead to lower energy dissipation rate per unit mass in the large scale.

## Acknowledgements

The financial supports from Unilever Research and Development Port Sunlight (UK), ORSAS and Department of Chemical Engineering, The University of Birmingham are gratefully acknowledged. The authors would also like to acknowledge Dr. H. Nobach for providing the codes for calculating the ACF and PSD from LDA data.

## References

Atiemo-Obeng, V.A. and Calabrese, R.V., 2004, in Paul, E.L., Atiemo-Obeng, V.A., & Kresta, S.M. (eds). (John Wiley & Sons, Hoboken, NJ, USA)

Bakker, A. and Oshinowo, L.M., 2004, Modelling of turbulence in stirred vessels using large eddy simulation. Trans. IChemE Part A, 82: 1169–1178.

Calabrese, R.V., Francis, M.K., Kevala, K.R., Mishra, V.P., Padron, G.A. and Phongikaroon, S., 2002, Fluid dynamics and emulsification in high shear mixers, In *Proc. 3rd World Congress on Emulsions*

Doucet, L., Ascanio, G. and Tanguy, P.A., 2005, Hydrodynamics characterization of rotor–stator mixer with viscous fluids. Trans. IChemE Part A, 83: 1186–1195.

Dyster, K.N., Koutsakos, E., Jaworski, Z. and Nienow, A.W., 1993, An LDA study of the radial discharge velocities generated by a Rushton turbine: Newtonian fluids, $Re \geq 5$. Trans. IChemE Part A, 71: 11–23.

Fluent., (2004). *User's Guide, Release 6.2*. (Fluent Inc).

Karbstein, H. and Schubert, H., 1995, Development in continuous mechanical production of oil-in-water macro emulsions. Chem. Eng. Process., 34: 205–211.

Myers, K.J., Reeder, M.F., Ryan, D. and Daly, G., 1999, Get fix on high-shear mixing. Chem. Eng. Prog., 95: 33–42.

Ng, K. and Yianneskis, M., 2000, Observations on the distribution of turbulence energy dissipation in stirred vessel. Trans. IChemE Part A, 78: 334–341.

Nobach, H., 2002, Local time estimation for the slotted correlation function of randomly sampled LDA data. Exp. Fluids, 32: 337–345.

Pacek, A.W., Baker, M. and Utomo, A.T., 2007, Characterisation of flow pattern in a rotor–stator high shear mixer, in Proc. 6th European Congress on Chemical Engineering, Gani, R. and Johansen, K.D., Johansen, K.D. (eds)

Padron, G.A., 2001, Measurement and comparison of power draw in rotor–stator mixer, M.Sc. Thesis, University of Maryland, College Park, MD, USA.

Roussinova, V., Kresta, S.M. and Weetman, R., 2003, Low frequency macroinstabilities in a stirred tank: scale-up and prediction based on large eddy simulations. Chem. Eng. Sci., 58: 2297–2311.

Shekkar, S.M. and Jayanti, S., 2002, CFD study of power and mixing time for paddle mixing in unbaffled vessels. Trans. IChemE Part A, 80: 482–498.

Tummers, M.J. and Passchier, D.M., 1996, Spectral estimation using a variable window and the slotting technique with local normalization. Meas. Sci. Technol., 7: 1541–1546.

Wu, H. and Patterson, G.K., 1989, Laser-Doppler measurement of turbulent flow parameters in a stirred vessel. Chem. Eng. Sci., 44: 2207–2221.

Yeoh, S.L., Papadakis, G. and Yianneskis, M., 2004, Numerical simulation of turbulent flow characteristics in a stirred vessel using the LES and RANS approaches with the sliding/deforming mesh methodology. Trans. IChemE Part A, 82: 834–848.

Zhou, G. and Kresta, S.M., 1996, Distribution of energy between convective and turbulent flow for three frequently used impellers. Trans. IChemE Part A, 74: 379–389.

# CHAPTER V

## THE EFFECT OF STATOR GEOMETRY ON THE FLOW PATTERN AND ENERGY DISSIPATION RATE IN A ROTOR-STATOR MIXER

This chapter has been published in Chemical Engineering Research and Design volume 87 (2009), page 533 – 542 and orally presented in European Conference on Mixing (ECM) XIII, London, UK (14 – 17 April 2009). Some supplementary information regarding this chapter is also given in Appendix C.

CHEMICAL ENGINEERING RESEARCH AND DESIGN 87 (2009) 533–542

Contents lists available at ScienceDirect

Chemical Engineering Research and Design

journal homepage: www.elsevier.com/locate/cherd

# The effect of stator geometry on the flow pattern and energy dissipation rate in a rotor–stator mixer

A. Utomo[a], M. Baker[b], A.W. Pacek[a,*]

[a] Department of Chemical Engineering, University of Birmingham, Edgbaston, Birmingham B15 2TT, UK
[b] Unilever R&D Port Sunlight, Quarry Road East, Bebington, Wirral CH63 3JW, UK

ABSTRACT

The effect of stator geometry on the flow pattern and energy dissipation rate in a batch rotor–stator mixer has been investigated using sliding mesh method with standard k–ε turbulence model. It has been found that for the stators with narrow openings (small width-to-depth ratio) the liquid at certain distance from stator rotated in the opposite direction to the rotor rotation. This opposite rotation was induced by the strong circulation flows behind the jets. The predicted power numbers for the stators with circular and square openings were about 10% lower than experimental data and the power number for stator with slot openings was about 20% lower. The simulation results showed that the power number was proportional to the total flowrate. For all stators, about 50–60% of energy supplied by the rotor dissipated in the rotor swept region and approximately 25% in the jet region. The fraction of energy dissipated in the hole region was 12–15% for stators with narrow opening and only 8% for stator with wide opening. The order of magnitude of energy dissipation rate in each region (rotor swept region, holes and jets) was practically the same for all stators; however, the distribution of energy dissipation rate in the hole was more uniform in stator with narrow openings.



*Keywords:* Rotor–stator mixer; CFD; Sliding mesh; Stator design; Energy dissipation

## 1. Introduction

Rotor–stator mixers are characterized by small gap between the rotor and the stator, from 100 to 3000 μm (Karbstein and Schubert, 1995), and high rotor tip speed, between 10 and 50 m/s, creating very high shear rate in the gap (Atiemo-Obeng and Calabrese, 2004). The kinetic energy generated by the rotor dissipates mainly inside the stator what leads to very high-energy dissipation rate in stator region. Therefore, this type of mixers is used to handle energy intensive processes such as de-agglomeration, emulsification and homogenization (Myers et al., 1999).

The assembly of rotor and stator is often called the mixing head but also the stator itself is often called the head. Commercial rotor–stator mixers are usually supplied with fixed rotor and interchangeable stators of various designs to fit different process requirements. The selection of the best type of stator for a particular process is often done by trial and error supported by simple calculation of average energy dissipation rate based on the power number (Po) but the understanding of the hydrodynamics of different stators is rather limited.

Padron (2001) measured power numbers (Po) of radial-discharge rotor–stator mixers fitted with different stators. Using standard definition of Po and Re, he reported that in laminar flow, the power number was inversely proportional to the Reynolds number and independent of stator geometry. In turbulent flow, the power numbers were relatively constant and depended on stator geometry. The power number of Ross mixer varied from 2.4 for slotted head with 80 mesh screen to 3 for standard slotted head. The power number of Silverson mixer varied from 1.7 for standard disintegrating head to 2.3 for square hole and fine emulsor heads. He concluded that in laminar flow, Po was controlled by viscous dissipation in the gap, while in turbulent flow, Po was controlled by fluid impingement on the stator slots surfaces and the jets emerging from the holes.

* Corresponding author. Tel.: +44 121 414 5308; fax: +44 121 414 5324.
E-mail address: A.W.Pacek@bham.ac.uk (A.W. Pacek).
Received 15 October 2008; Received in revised form 3 December 2008; Accepted 5 December 2008
0263-8762/$ – see front matter © 2008 The Institution of Chemical Engineers. Published by Elsevier B.V. All rights reserved.
doi:10.1016/j.cherd.2008.12.011

**Nomenclature**

| | |
|---|---|
| $D$ | rotor diameter (m) |
| $d$ | hole diameter (mm) |
| $k$ | constant |
| $Fl$ | the flow number, $Fl = Q/ND^3$ |
| $N$ | rotor speed (1/s) |
| $P$ | power (W) |
| $r$ | radial direction (mm) |
| $Po$ | the power number, $Po = P/(\rho N^3 D^5)$ |
| $Re$ | the Reynolds number, $Re = \rho ND^2/\mu$ |
| $U_{rad}$ | radial velocity (m/s) |
| $U_{tan}$ | tangential velocity (m/s) |
| $U_{tip}$ | tip velocity (m/s) |
| $z$ | axial direction (mm) |

*Greek letters*

| | |
|---|---|
| $\beta$ | the angle between the leading and trailing edges (°) |
| $\Delta$ | the deviation of flowrate or torque from its time averaged value (kg/s) or (Nm) |
| $\varepsilon$ | energy dissipation rate ($m^2/s^3$) |
| $\varphi$ | blade position relative to $\theta = 0$ (°) |
| $\mu$ | viscosity (Pa s) |
| $\rho$ | density ($kg/m^3$) |
| $\theta$ | tangential direction (°) |

Utomo et al. (2008) investigated the flow pattern and distribution of energy dissipation rates in Silverson mixer fitted with disintegrating head in the turbulent regime ($Re = 26{,}000$–$52{,}000$). They found that the agreement between CFD simulation (using standard k–$\varepsilon$ model) and LDA measurement in terms of velocity profiles in the bulk and of the jets emerging from the holes was generally very good. Both simulation and measurement showed that the jets velocity and flowrate through stator holes were proportional to the rotor speed while the energy dissipation rate scaled with $N^3$. The calculated power number was 1.55, close to the experimental value of 1.7 (Padron, 2001). The kinetic energy balance based on LDA measurements showed that about 70% of energy was dissipated inside the mixing head compared to 60% predicted by CFD. The simulation also showed that the highest energy dissipation rate occurred close to stagnation points at the leading and trailing edges of the stator holes.

Besides disintegrating head, Silverson mixers are also supplied with slotted head and/or square hole head. In this work, full three-dimensional CFD simulations were employed to investigate the flow patterns and distribution of energy dissipation rates for each head. The assessment of CFD prediction of the rotor–stator mixer has been carried out in the previous works (Pacek et al., 2007; Utomo et al., 2008) and therefore only simulation data is presented in this work.

## 2. Methodology

### 2.1. Geometry

The flow in a Silverson L4RT rotor–stator mixer was analyzed. The vertical and horizontal cross sections of the mixing head are shown in Fig. 1(a) and (b), respectively.

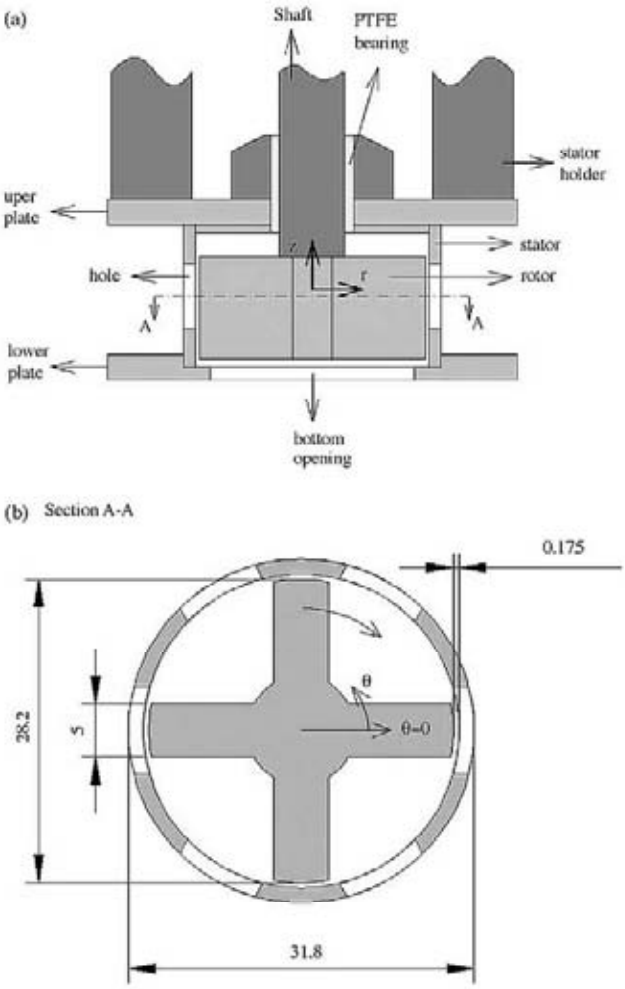


**Fig. 1 – (a) Vertical and (b) horizontal cross sections of the mixing head (fitted with disintegrating head). Pins connecting upper and lower plates are not shown. Dimensions in mm.**

A four blade impeller of diameter 28.2 mm and height 12.8 mm (Fig. 1) was used as a rotor and the interchangeable stator was held by two horizontal plates connected by pins.

Cylindrical coordinate system with the origin located in the middle of the vessel and z-axis coinciding with the vertical axis of the vessel was used in this work. The angular coordinate ($\theta$) was positive in an anti-clockwise direction as viewed from above, while the rotor rotates in a clockwise direction (negative $\theta$) as shown in Fig. 1(b). The mixing head was placed symmetrically in the middle of an un-baffled, flat bottom vessel of diameter 150 mm. The midpoint between the upper and lower plate was at $z = 0$, while the center of the rotor was at $z = -2.8$ mm.

Three stator geometries from Silverson were investigated in this work, i.e. disintegrating head (Fig. 2(a)), slotted head (Fig. 2(b)) and square hole head (Fig. 2(c)). The outer diameters and thicknesses of these stators varied slightly from 31.58 to 31.8 mm and 1.51 to 1.66 mm, respectively. The gaps between the rotor and stators also varied from 0.15 to 0.19 mm. CFD models assumed that all stators had the same outer diameter of 31.8 mm, the same thickness of 1.625 mm and the same gap width of 0.175 mm. The details of each stator are given in Table 1.

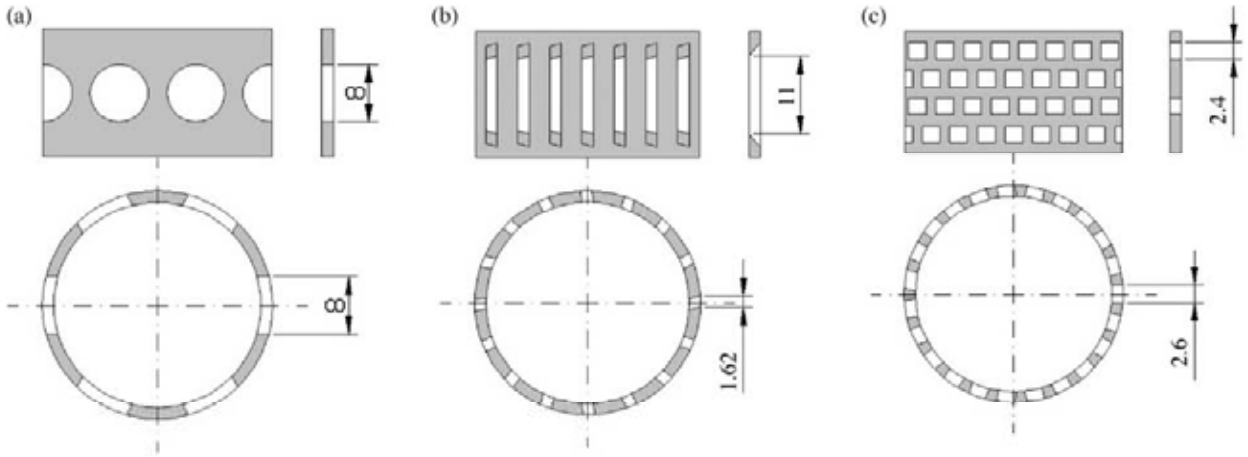


**Fig. 2 – Stator geometries investigated in this work: (a) disintegrating head, (b) slotted head and (c) square hole head.**

### 2.2. Simulation

The simulations were carried out using Fluent 6.3 with transient sliding mesh and standard k–ε turbulent model. It is well known that this model underestimates turbulent kinetic energy but it gives reasonably good prediction of mean flow and has been widely used to predict the flow pattern and energy dissipation rates in stirred tanks (Ng et al., 1998; Yeoh et al., 2004; Jaworski and Zakrzewska, 2002). The tendency to underpredict turbulent kinetic energy is typical for all RANS (Reynolds averaged Navier–Stokes) based turbulence models, including anisotropic Reynolds stress model (RSM) which is considerably more demanding in terms of computational cost and less stable than standard k–ε model (Murthy and Joshi, 2008). Large eddies simulation (LES) can give better prediction of turbulent kinetic energy (Yeoh et al., 2004; Murthy and Joshi, 2008); however, this model is computationally very expensive. Standard k–ε model is robust and computationally economic (Marshall and Bakker, 2004), therefore it seems to be fit for comparison between different stator geometries.

The working fluid was water at 20 °C and the rotor speed was kept constant at 4000 rpm ($Re = 52{,}000$). For the disintegrating head, the simulation was started with steady state multiple reference frame and then continued with the transient sliding mesh simulation with 60 time steps per rotor revolution for 50 revolutions (Utomo et al., 2008). For other geometries, the simulations were started directly with the sliding mesh method with 120 time steps per rotor revolutions and the simulations were run for 100 rotations. The results, including that from the disintegrating head, were then refined with 300 time steps per rotor revolution for 6 revolutions before they were analyzed. For the coarse time steps, 6° per time step for disintegrating head and 3° per time step for other heads, the solutions were converged at residuals below $10^{-3}$ and below $10^{-4}$ for the fine time step. Each simulation was run on a single node of computer cluster consisting of 64-bit AMD 2.6 GHz processors each with 5 GB RAM. One time step took about 7–12 min CPU time.

The effect of number of grid cells and time step on the accuracy of simulation (disintegrating head) has been recently investigated by the authors (Utomo et al., 2008) who reported that once the number of cells exceeds one million, further increase has negligible effect on the prediction of jet velocity profile and flow pattern in the bulk. In this work, the number of computational cells varied from 1.1 to 1.4 millions and about 500 thousands of them were located in the rotor swept volume as the rotating mesh. The free surface was modeled with symmetry (Jaworski et al., 2000) and other solid surfaces were set as no-slip wall with enhanced wall treatment which is capable to describe the flow in the laminar, transition and turbulent regimes of boundary layer (Fluent's User Guide, 2004). The time and space were discretized using second order implicit and QUICK schemes, respectively. The pressure and momentum equations were coupled using SIMPLE algorithm

Typical computational mesh used in this work is shown in Fig. 3(a) and (b). The mesh inside the stator, including the holes, is very fine (around 0.3–0.5 mm) and consists of prism and hexahedral cells. The mesh in the bulk region is much coarser (around 1–3 mm) and consists of mainly hexahedral cells. Between these two regions, just outside the stator, tetrahedral mesh is used to connect the fine and coarse regions so that the total number of computational cells can be minimized. The number of computational cells in the bulk region (including the tetrahedral mesh) is comparable to that of Roussinova et al. (2003) and Bakker and Oshinowo (2004) who used LES to simulate the flow in stirred vessels of diameters from 0.2 to 0.29 m and therefore should be fine enough for the RANS simulation in smaller vessel (0.15 m). The gap between the rotor and the stator was divided into five hexagonal cells and the interface between the stationary and the rotating meshes was located in the middle of the gap. The shapes of computational cells on the stator holes are shown in Fig. 4.

**Table 1 – Summary of stator geometries simulated in this work.**

| Head | No. of hole | Dimension (mm) | Area/hole (mm²) | Total hole area (mm²) |
|---|---|---|---|---|
| Disintegrating head | 6 | $d = 8$ | 50.24 | 301.44 |
| Slotted head | 16 | $1.62 \times 11$ | 17.3 | 276.8 |
| Square hole head | 92 | $2.6 \times 2.4$ | 6.24 | 574.08 |

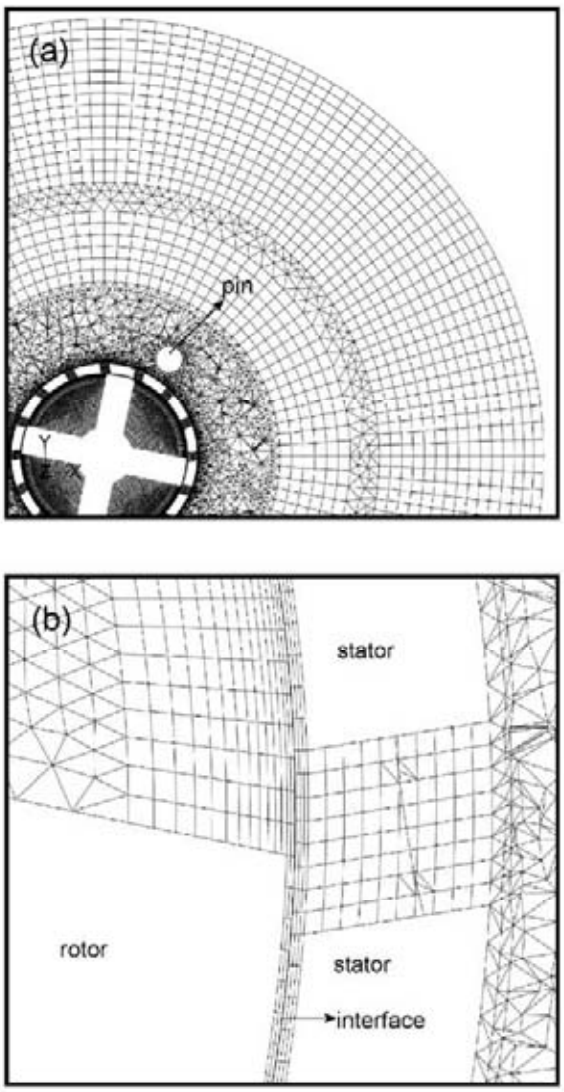


**Fig. 3 – (a) Computational mesh of the slotted head and (b) detail of the mesh around the hole.**

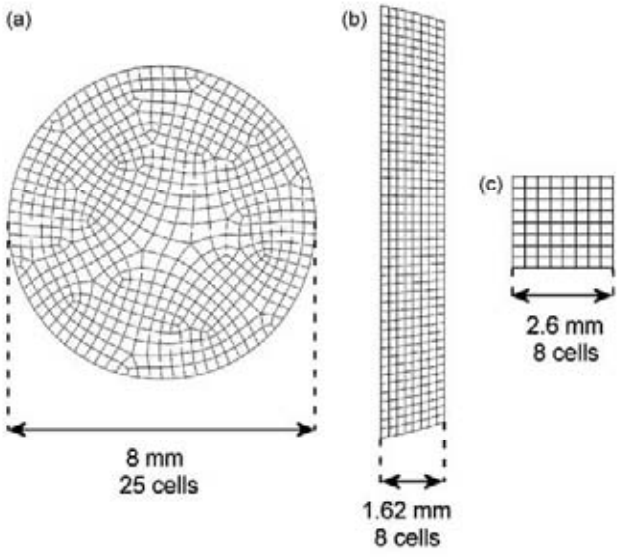


**Fig. 4 – Computational cells on the stator holes: (a) disintegrating head, (b) slotted head and (c) square hole head.**

## 3. Results and discussions

### 3.1. *Flow patterns of the jets*

The flow inside the head is predominantly tangential. Once the fluid passes the hole, it starts moving in radial direction and finally when it hit the surface of the leading edge of the hole practically all the tangential momentum is converted into radial momentum and the jet emerges from the hole. The flow patterns inside the stators and of the jets emerging from various stator geometries are shown in Fig. 5. In all cases, the jets only emerging from a part of the hole close to the leading edge, and behind the jets the circulation loops are formed. This flow pattern is observed in all investigated stators regardless the shape and size of the holes.

However, the characteristics of the jets emerging from the wide and narrow holes are different. In the case of disintegrating head, where the holes are wide, strong jets emerge from the holes and they move radially until they hit the vessel wall where the radial momentum is converted into tangential momentum (Figs. 5(a), 6(a) and 7(a)). In the case of other heads with very narrow holes, the jets decay in just few millimetres away from the holes (as comparison, the stator thickness is 1.625 mm). This is due to higher rate of momentum transfer from the small jets to bulk liquid as they have larger interfacial area (the boundary between the jet and surrounding liquid) than the bigger jets.

Fig. 6(b) and (c) show that the jets emerging from narrow holes moves tangentially in the direction opposite to the rotor as they move away from the holes and decay, i.e. the rotor moves in the clockwise direction while the jets move in the counterclockwise direction, which drives the liquid in the bulk also in the same counterclockwise direction (Fig. 7(b) and (c)). This phenomenon occurs due to the interaction between the jets and the circulation flow behind the jets. The jets emerge from the slotted and square hole head are weak and therefore easier to be diverted by the circulation flow behind the jet. On the other hand, the jets emerge from the disintegrating head are relatively strong and large compared to the circulation flow behind the jet and therefore are not affected.

Fig. 8 shows the time averaged radial velocity distributions (over 90° rotor rotation) of the jets emerging from various stator holes at $r = 15.9$ mm (Fig. 9). Fig. 8 indicates that the fraction of the hole where the jet emerges and circulation takes place is relatively the same for all investigated geometries. The time averaged jet tangential velocity (Fig. 10); however, decreases with increasing hole width, i.e. jets emerging from narrow holes have positive tangential velocity (opposite rotor rotation) and those from wide holes have negative tangential velocity (in the same direction as rotor rotation) as shown previously.

This suggests that the tangential velocity of the jets emerging from the holes is affected by the width-to-depth ratio of the hole. In the narrow hole where the width-to-depth ratio is low, the circulation interacts strongly with the jet and diverts the tangential velocity of the jets into direction opposite to the rotor rotation (Fig. 5(b) and (c)). In the wide hole where the width-to-depth ratio is high, the interaction between jet and circulation is weak and therefore the tangential velocity of the jet is not affected.

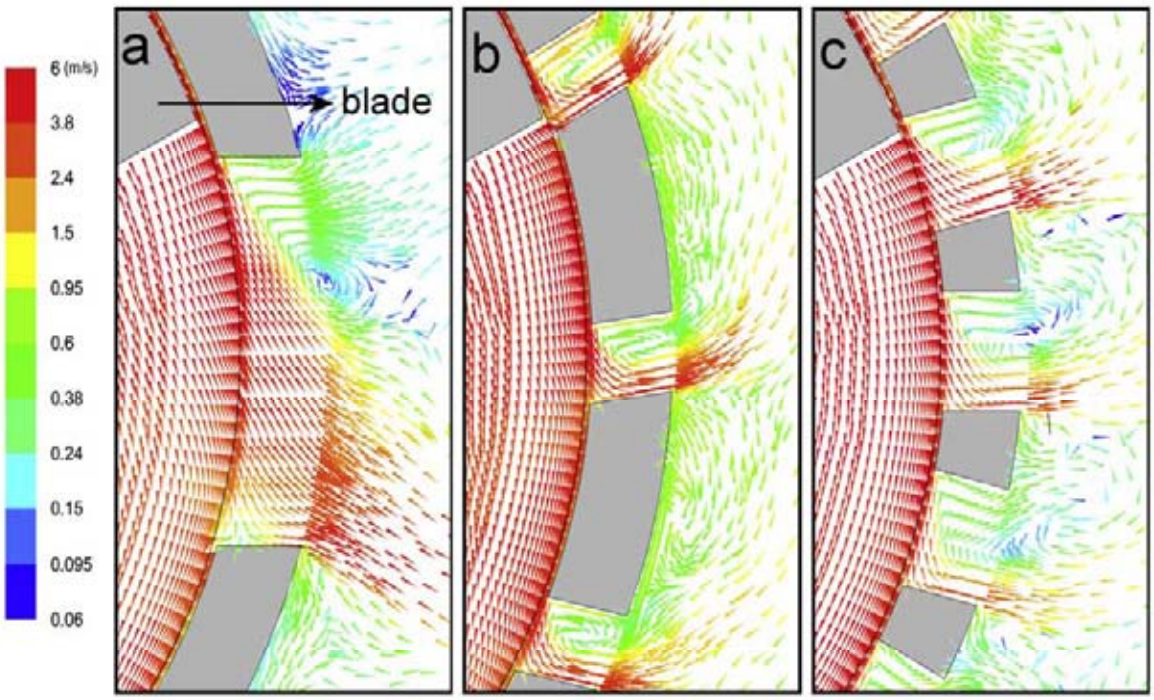


**Fig. 5 – Flow patterns (radial and tangential velocities) of the jets emerging from different stators: (a) disintegrating head, (b) slotted head and (c) square hole head. The velocity vectors for disintegrating, slotted and square hole heads are taken at plane z = −0.8 mm, z = 0, and z = 1.3 mm, respectively.**

### 3.2. *Flowrate, torque and power number*

The velocity of the jet emerging from a particular hole fluctuates at a frequency related to the position of rotor blades relative to that hole (Utomo et al., 2008). Consequently, the total flowrate (the total amount of liquid pumped through stator holes) and total torque also fluctuates as a function of blade position. Figs. 11 and 12 show the deviations of flowrate and torque from their time averaged values as a function of blade position.

The amplitude of flowrate fluctuation is relatively small, only about 2% of the time averaged value for both disintegrating and slotted heads and practically zero for square hole head. The amplitude of torque fluctuation, however, can reach 100% of its average value for slotted head, but only about 30% for disintegrating head and practically zero for square hole head. The period of fluctuation is determined by the arrangement of the holes on the stator. For disintegrating head with six holes, the period of fluctuation is 30° and 22.5° for slotted head with 16 holes. The square holes are arranged into four

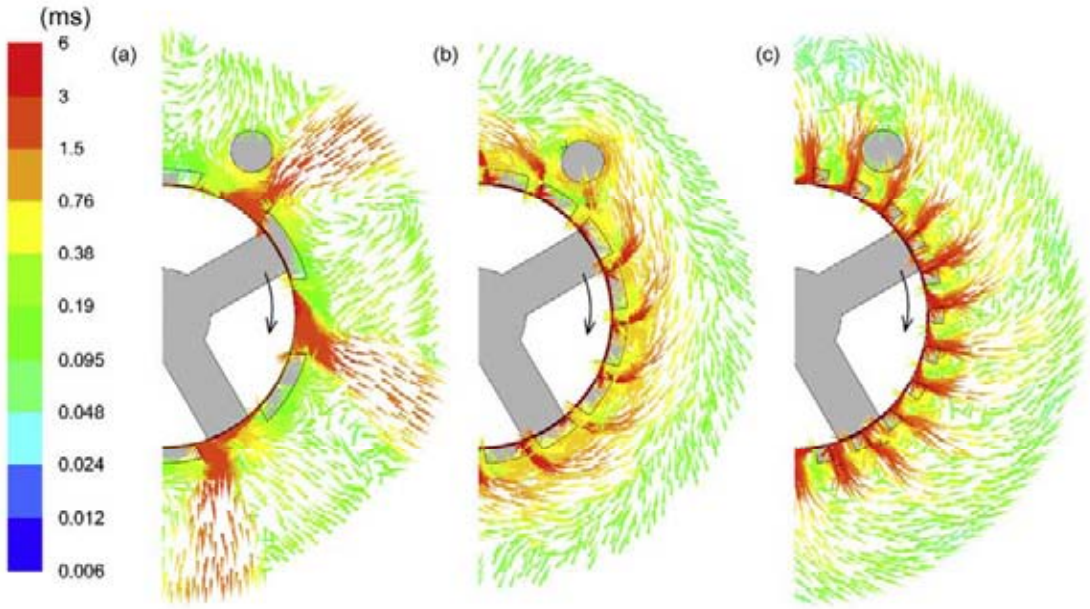


**Fig. 6 – Flow patterns (radial and tangential velocities) around the mixing heads (r = 14.3–30 mm): (a) disintegrating head, (b) slotted head and (c) square hole head. All velocity vectors are taken at the same plane as in Fig. 5.**

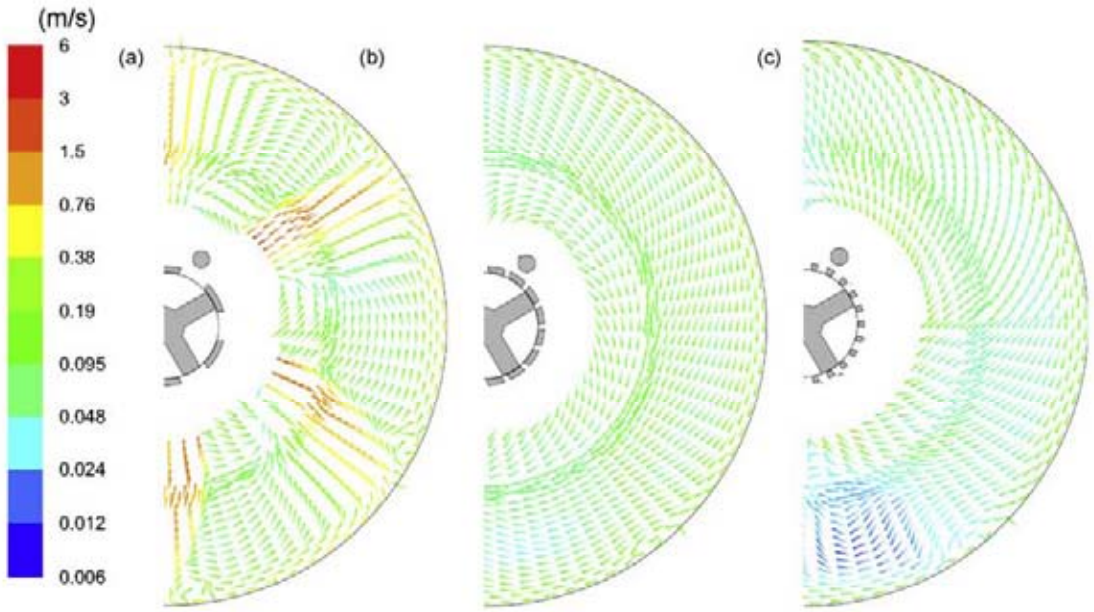


**Fig. 7 – Flow patterns (radial and tangential velocities) in the bulk region ($r$ = 30–75 mm): (a) disintegrating head, (b) slotted head and (c) square hole head. All velocity vectors are taken at the same plane as in Fig. 5.**

rows and the holes on each row overlap with those on the row above and below (Fig. 2(c)). This overlap causes minimum fluctuation of both flowrate and torque.

Table 2 shows the prediction of time averaged total flowrates through the holes and power numbers calculated from time averaged torques for all investigated geometries. The simulation results showed that flowrate generally increases with total hole area (correlation coefficients 0.86). However, the slotted head, which has slightly smaller total hole area but more number of the leading edge than the disintegrating head, delivers more flowrate than the disintegrating head. This may suggest that flowrate is also a function of total surface area of the leading edges since they act as flow directors (Fig. 5).

The predicted power numbers for disintegrating and square hole heads are approximately 10% lower than experimental values (Padron, 2001), while that for slotted head the difference is in the order of 20%. The slotted head has the highest velocity gradient across the hole, 50% higher than the square hole head, therefore more computational cells are necessary to describe the flow patterns of jets and circulation in the hole more accurately. Also the holes on the real object may slightly vary due to manufacturing method whereas the holes on the CFD model are identical. All those factors might contribute to the discrepancy between CFD and experiment.

The discretization scheme may also affect the simulation result. Although Brucato et al. (1998) reported that there is no difference between hybrid upwind and QUICK schemes, Aubin et al. (2004) reported that QUICK scheme gave lower predictions of the power number and flowrate than higher order upwind (in CFX4). QUICK scheme underpredicted the power number but gave good prediction of the circulation number, while higher order upwind gave good prediction of the power number but overpredicted the circulation number.

The simulation also shows that the power number ($Po$) at constant rotor speed is proportional to the flowrate through

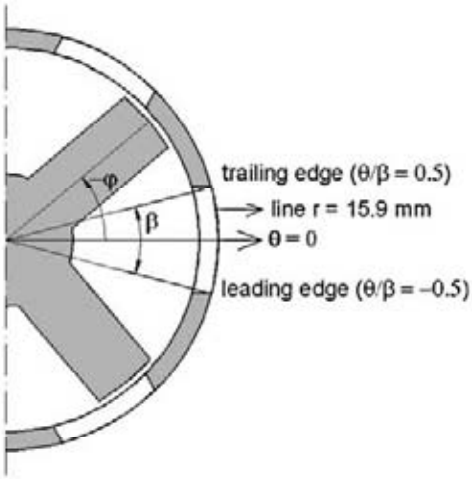


**Fig. 9 – $\beta$ is the angle between the leading and trailing edge while $\varphi$ describing the blade position is defined as the angle between the $\theta$ = 0 and middle of the blade and is positive in clockwise direction (the same as rotor rotation).**

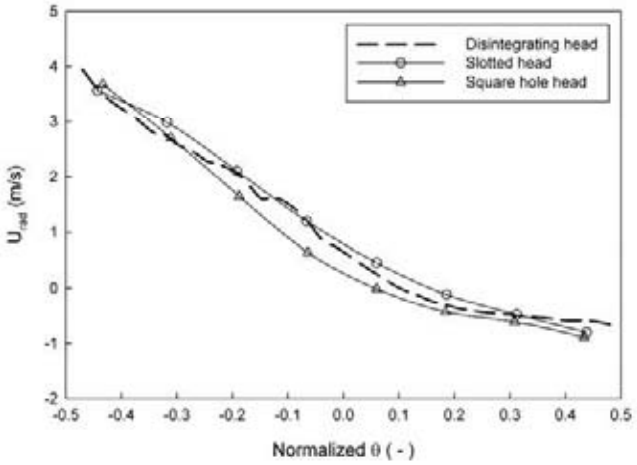


**Fig. 8 – Time averaged jet radial velocity profiles (taken in the middle of the hole over 90° rotor rotation) along line $r$ = 15.9 mm (Fig. 9) for various stator geometries. Normalized $\theta$ is defined in Fig. 9.**

**Table 2 – Flowrates and the power numbers for various stator geometries at 4000 rpm.**

| Stator | Total hole area (mm²) | Flowrate (kg/s) | Po (simulation) | Po (Padron, 2001) | %Difference |
|---|---|---|---|---|---|
| Disintegrating head | 301.44 | 0.268 | 1.53 | 1.7 | −10.0% |
| Slotted head | 276.80 | 0.275 | 1.66 | 2.1 | −20.9% |
| Square hole head | 574.08 | 0.389 | 2.05 | 2.3 | −10.9% |

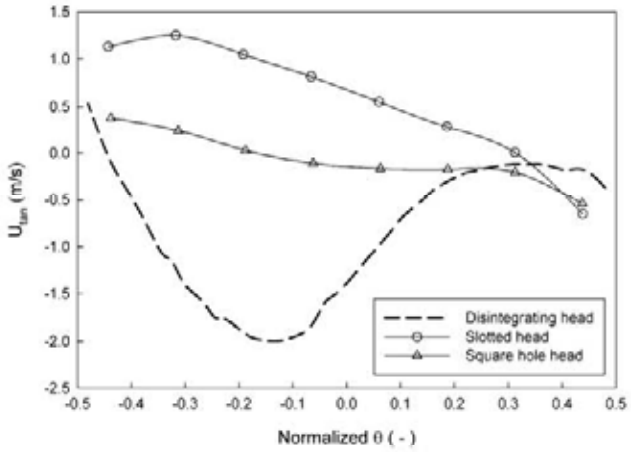


**Fig. 10 – Time averaged jet tangential velocity profiles (taken in the middle of the hole over 90° rotor rotation) along line r = 15.9 mm (Fig. 9) for various stator geometries.**

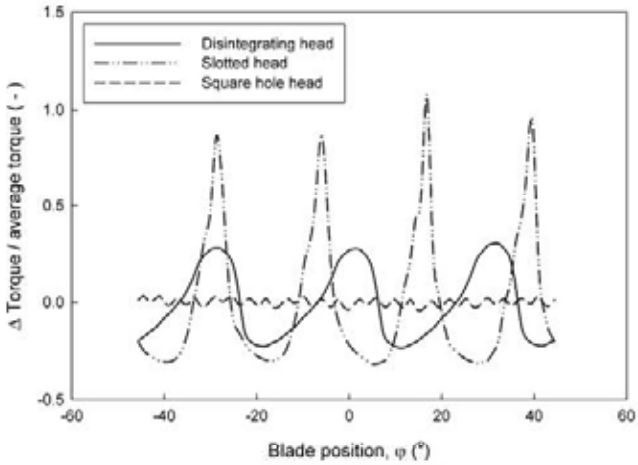


**Fig. 12 – Fluctuations of torques in the disintegrating, slotted and square hole heads as a function of blade position (Fig. 9). Δ is the deviation of torque from its time averaged value.**

the holes (Fig. 13). This is typical for centrifugal pumps and stirred vessels where power is proportional to the product of total kinetic energy and flowrate. The total kinetic energy is proportional to $N^2D^2$ whilst flowrate is proportional to $\rho ND^3$ (Hemrajani and Tatterson, 2004) and therefore

$$P = Po\rho N^3D^5 = (kN^2D^2)(Fl\rho ND^3) \quad (1)$$

where Fl is the flow number and Po is equal to $k$ times Fl. Fig. 14 shows that the total kinetic energy are relatively the same for all heads investigated although they increase slightly with the flowrate. However, the increase of velocity due to flowrate is very small compared to the tip velocity and the total kinetic energy can be assumed constant for various heads and therefore Po depends on Fl or flowrate. Since the flowrate correlates

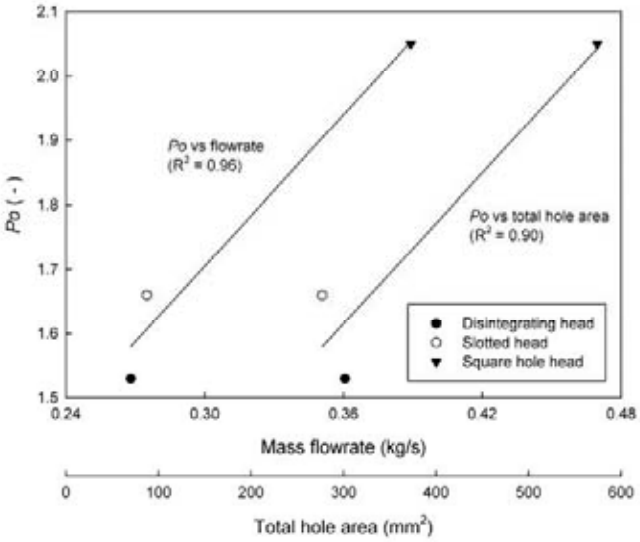


**Fig. 13 – Power number as functions of flowrate and total hole area.**

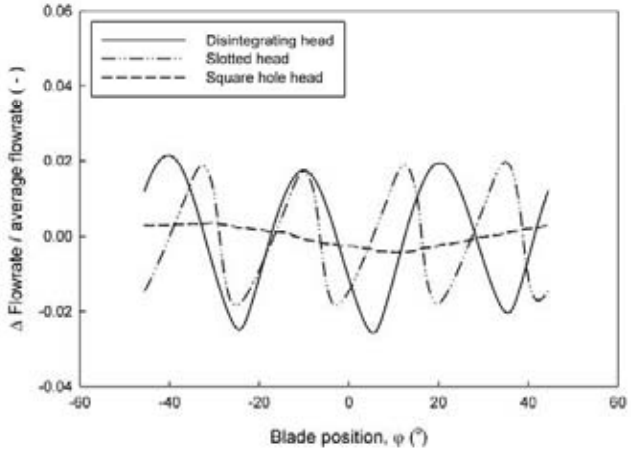


**Fig. 11 – Fluctuations of flowrates in the disintegrating, slotted and square hole heads as a function of blade position (Fig. 9). Δ is the deviation of flowrate from its time averaged value.**

with the total hole area, the power number can be correlated to the total hole area as shown in Fig. 13.

### 3.3. *Energy dissipation rate around the mixing head*

The contours of energy dissipation rate for different stators (Fig. 15) are very similar. Moderate energy dissipation rate occurs in the rotor swept region and jets emerging from the holes while high-energy dissipation rate occurs around the leading and trailing edges due to stagnation in those regions. The energy of the small jets emerging from narrow holes dissipates in the close proximity to the mixing head while that of the large jets emerging from wider holes dissipates over wider

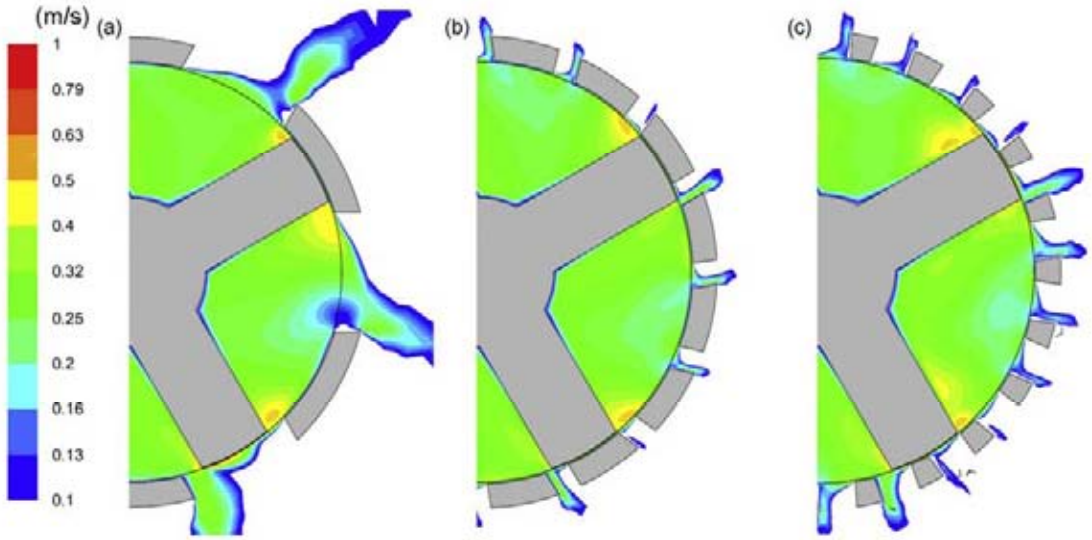


**Fig. 14 – Contours of total kinetic energy (normalized by $U_{tip}^2$) at 4000 rpm: (a) disintegrating head, (b) slotted head and (c) square hole head. All contours are taken at the same plane as in Fig. 5.**

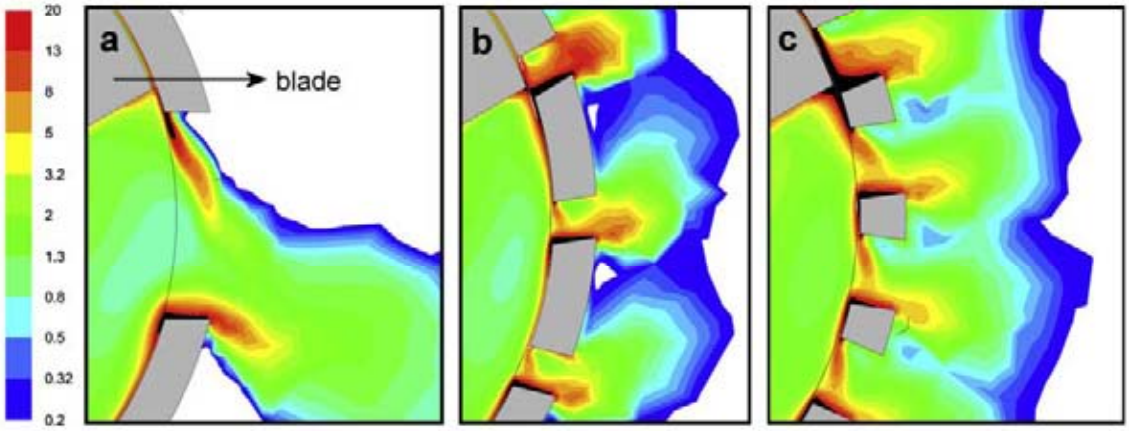


**Fig. 15 – Contours of energy dissipation rate (normalized by $N^3D^2$) at 4000 rpm: (a) disintegrating head, (b) slotted head and (c) square hole head. The black areas represent normalized energy dissipation rate higher than 20. All contours are taken at the same plane as in Fig. 5.**

area. The energy dissipation rate in the rest of the tank is very low and is not shown.

The energy dissipation rate on the leading and trailing edges of the holes which occurs due to stagnation on those points is determined by the fluid velocity before impingement and can be related to the rotor tip speed (*ND*). Similarly, the velocity of emerging jets also depends on the rotor tip speed. Therefore, at constant rotor tip speed, the magnitudes of energy dissipation rate in a particular region (holes or jets) are practically the same. Although the order of magnitude of the energy dissipation rate in the rotor swept volume are also practically the same, the average energy dissipation rate in the rotor swept volume actually increases with the flowrate. Table 3 shows that the amount of energy dissipated in the rotor swept volume in the square hole head is 1.58 higher than the energy dissipated in the disintegrating head and therefore the energy dissipation rate in the rotor swept region in the square hole head is actually 58% higher than that in the disintegrating head.

The simulation also shows that in the narrower holes, the areas of high-energy dissipation rate from the leading and trailing edges merges leading to more uniform distribution of energy dissipation rate across the hole. This might lead to a more uniform drop size during emulsification or more uniform aggregate size during de-agglomeration process.

### 3.4. *Distribution of energy dissipated in the tank*

The predictions of energy dissipated in different regions in the mixer for all investigated stators are summarized in Table 3.

**Table 3 – The amount of energy dissipated in various regions in the vessel.**

| Stator | Rotor swept region (W) | Hole region (W) | Jet region (W) | Rest of the tank (W) | Total (W) |
|---|---|---|---|---|---|
| Disintegrating head | 3.14 (47.1%) | 0.56 (8.4%) | 1.58 (23.7%) | 1.39 (20.8%) | 6.67 |
| Slotted head | 3.73 (54.9%) | 0.99 (14.6%) | 1.73 (25.4%) | 0.35 (5.1%) | 6.80 |
| Square hole head | 4.97 (60.3%) | 0.99 (12.0%) | 2.18 (26.5%) | 0.10 (1.2%) | 8.24 |

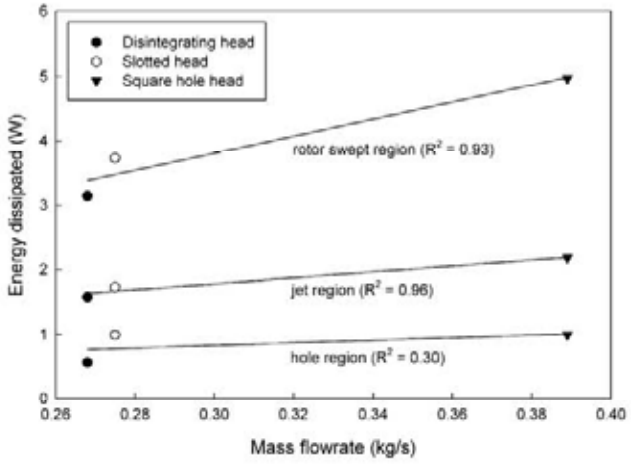


**Fig. 16 – Correlations between the amounts of energy dissipated in the rotor swept volume, hole region, jet region and the flowrate.**

Rotor swept region is defined as the volume inside the stator, hole region is defined as the total volume of all holes and jet region is defined as a torus shaped region around mixing head of the same height as the mixing head, inner radius of 15.9 mm (outer radius of the stator) and outer radius of 30 mm (Pacek et al., 2007). The amount of energy dissipated in a particular region was obtained by integrating the calculated energy dissipation rate over that region.

For all geometries, approximately 50–60% of the total energy is dissipated in the rotor swept region and about 25% of energy is dissipated in the jet region. Obviously, if the boundary of the jet region is moved closer to the mixing head, the fraction of energy dissipated in that region for disintegrating head would be much smaller than those for other geometries. Only small fraction of total energy is dissipated in holes where the highest energy dissipation rate occurs. For disintegrating head, less than 10% of total energy is dissipated in the hole region, while for those with narrower holes about 12–15% of energy dissipated in this region.

The jets emerging from stators with wide holes extend to the bulk region therefore with these stators considerable amount of energy is dissipating in the bulk of the tank. On the other hand, jets emerging from narrow holes dissipate very close to the mixing head and only small amount of energy dissipates in the bulk region. Therefore, stators with wide holes are suitable when bulk mixing is required as to incorporate floating powder into liquid although these heads generate smaller flowrate than those with narrower holes (Table 2).

The simulation results suggest that the energy dissipated in the rotor swept region and jet region is linearly dependent of flowrate through stator holes (correlation coefficients above 0.93, Fig. 16). However energy dissipated in the hole region does not correlate well with the flowrate (correlation coefficient 0.30) because it strongly depends of stagnation area of the leading and trailing edges (correlation coefficient 0.89).

## 4. Conclusions

The effect of stator geometry on the flow pattern and energy dissipation rate in the batch rotor–stator mixer has been studied. The flow pattern in the stator holes was very similar for all shapes and sizes of the holes with jets emerging in the proximity of the leading edges and circulation flow behind the jets. Jets emerging from larger holes extended up to the tank wall, while the jets emerging from smaller holes dissipated close to the mixing head.

Jets emerging from wide holes (large width-to-depth ratio) were not affected by circulation loops behind them and generated bulk circulation in the same direction as the rotor while jets emerging from narrow holes (small width-to-depth ratio) were bended by circulation loops behind them what led to the circulation of bulk liquid against the rotor.

Narrower holes created more uniform energy dissipation rate in the hole region since the high-energy dissipation rate areas from the leading and trailing edges merge what implies stator with narrow holes can be used to produce dispersion with narrow drop size distributions.

The simulation results also showed that the power number was proportional to the flowrate through stator holes while the flowrate correlated with the total hole area. The energy dissipated in the rotor swept region (about 50–60% of the total energy input) and in the jet region (about 25% of the total energy input) depends linearly of the flowrate, while the energy dissipated in the holes correlated better with the total surface area of the leading and trailing edges where the stagnation occurs. However, the accuracy of numerical value of energy dissipation rate is limited by k–$\varepsilon$ model.

## Acknowledgements

The financial supports from Unilever Research and Development Port Sunlight (UK), ORSAS and Department of Chemical Engineering, The University of Birmingham are gratefully acknowledged.

## References

Atiemo-Obeng, V. and Calabrese, R.V., 2004, Rotor–stator mixing devices, in Handbook of Industrial Mixing: Science and Practice, Paul, E.L., Atiemo-Obeng, V., & Kresta, S.M. (eds). (John Wiley & Sons, Inc, Hoboken, NJ, USA)

Aubin, J., Fletcher, D.F. and Xuereb, C., 2004, Modeling turbulent flow in stirred tanks with CFD: the influence of the modeling approach, turbulence model and numerical scheme. Exp Therm Fluid Sci, 28: 431–445.

Bakker, A. and Oshinowo, L.M., 2004, Modelling of turbulence in stirred vessels using large eddy simulation. Chem Eng Res Des, 82: 1169–1178.

Brucato, A., Ciofalo, M., Grisafi, F. and Micale, G., 1998, Numerical prediction of flow fields in baffled stirred vessels: a comparison of alternative modelling approaches. Chem Eng Sci, 53: 3653–3684.

Fluent Inc., (2004). *Fluent's User Guide*. (Fluent Inc).

Hemrajani, R.R. and Tatterson, G.B., 2004, Mechanically stirred vessels, in Handbook of Industrial Mixing: Science and Practice, Paul, E.L., Atiemo-Obeng, V., & Kresta, S.M. (eds). (John Wiley & Sons, Inc, Hoboken, NJ, USA)

Jaworski, Z., Bujalski, W., Otomo, N. and Nienow, A.W., 2000, CFD study of homogenization with dual Rushton turbines—comparison with experimental results. Part I. Initial studies. Chem Eng Res Des, 78: 327–333.

Jaworski, Z. and Zakrzewska, B., 2002, Modelling of the turbulent wall jet generated by a pitched blade turbine impeller: the effect of turbulence model. Chem Eng Res Des, 80: 846–854.

Karbstein, H. and Schubert, H., 1995, Developments in the continuous mechanical production of oil-in-water macro-emulsions. Chem Eng Process, 34: 205–211.

Marshall, E.M. and Bakker, A., 2004, Computational fluid mixing, in Handbook of Industrial Mixing: Science and Practice, Paul, E.L., Atiemo-Obeng, V.A., & Kresta, S.M. (eds). (John Wiley & Sons, Inc, Hoboken, NJ)

Murthy, B.N. and Joshi, J.B., 2008, Assessment of standard k–ε, RSM and LES turbulence models in a baffled stirred vessel agitated by various impeller designs, Chem Eng Sci, 63: 5468–5495.

Myers, K.J., Reeder, M.F., Ryan, D. and Daly, G., 1999, Get fix on high-shear mixing. Chem Eng Prog. 95: 33–42.

Ng, K., Fentiman, N.J., Lee, K.C. and Yianneskis, M., 1998, Assessment of sliding mesh CFD predictions and LDA measurements of the flow in a tank stirred by a Rushton impeller. Chem Eng Res Des, 76: 737–747.

Pacek, A.W., Baker, M. and Utomo, A.T., 2007, Characterisation of Flow Pattern in a Rotor Stator High Shear Mixer, in Proc. 6th European Congress on Chemical Engineering, Gani, R. and Johansen, K.D., Johansen, K.D. (eds) Copenhagen, Denmark,

Padron, G.A., 2001, Measurement and Comparison of Power Draw in Rotor-Stator Mixers. M.Sc. Thesis (University of Maryland, College Park, MD, USA).

Roussinova, V., Kresta, S.M. and Weetman, R., 2003, Low frequency macroinstabilities in a stirred tank: scale-up and prediction based on large eddy simulations. Chem Eng Sci. 58: 2297–2311.

Utomo, A.T., Baker, M. and Pacek, A.W., 2008, Flow pattern, periodicity and energy dissipation in a batch rotor–stator mixer, Chem Eng Res Des, 86: 1397–1409.

Yeoh, S.L., Papadakis, G. and Yianneskis, M., 2004, Numerical simulation of turbulent flow characteristics in a stirred vessel using the LES and RANS approaches with the sliding/deforming mesh methodology. Chem Eng Res Des, 82: 834–848.

# CHAPTER VI

# THE EFFECTS OF HOLE SPACING AND STATOR THICKNESS ON THE FLOW PATTERN AND ENERGY DISSIPATION RATE IN A BATCH ROTOR-STATOR MIXER

## *6.1. Introduction*

In the previous chapter, standard stator geometries supplied by Silverson have been numerically investigated. It has been found that the flow patterns in the holes were practically the same for all investigated stators, however, the directions of emerging jets were affected by the hole width-to-depth ratio. The simulations also showed that stagnations on the hole edges created high local energy dissipation rate in rotor-stator mixer.

In this chapter, other geometries based on the standard slotted head were simulated to investigate the effect of hole shape, hole spacing and hole width-to-depth ratio on the flow pattern, flowrate, torque, power number and energy dissipation rate. The effect of the stator thickness on jet direction at constant width-to-depth ratio was also investigated.

Experimental investigations of bulk flow patterns revealed that slotted and square hole heads produced different flow patterns in the bulk liquid when the

heads were installed in inverted position. This was explained by not complete symmetry of the heads and will be discussed in this section.

## 6.2. CFD simulations

The investigated stators are shown in *Fig. 6.1*. The number of holes, hole dimension and total hole area in each stator are given in *Table 6.1*. The details of three standard stators (disintegrating, slotted and square hole heads) are also given in *Table 6.1* for comparison. In all CFD models, the inner diameter of the stators was 28.55 mm and the rotor-stator gap was 0.175 mm. The thicknesses of thick slotted head (TWSH) and thick disintegrating head (TDH) were 3.2 and 8 mm respectively (holes width-to-depth ratios were equal to one) while the thickness of other stators was 1.625 mm (holes width-to-depth ratios varied from 1 to 4.9).

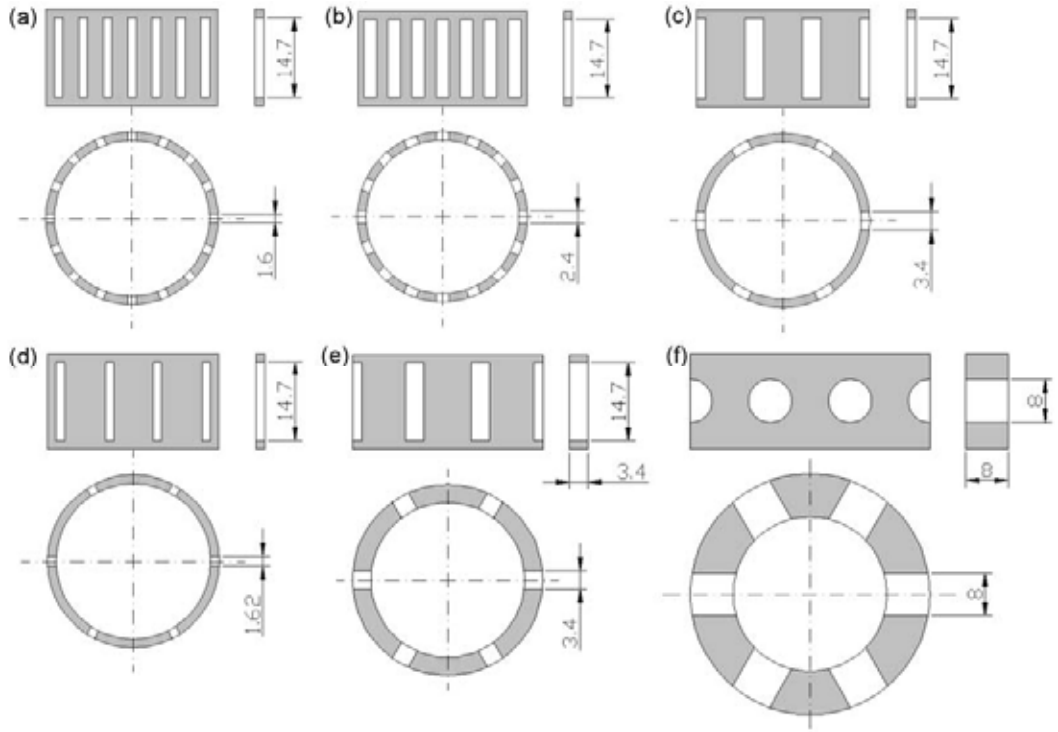


***Fig. 6.1.*** *Modified stator geometries investigated in this work (a) rectangular slotted head (RSH), (b) wide slotted head (WSH), (c) wide slotted head 6 holes (WSH6), (d) rectangular slotted head 6 holes (RSH6), (e) thick wide slotted head 6 holes (TWSH) and (f) thick disintegrating head (TDH).*

***Table 6.1.*** *Summary of stator geometries simulated in this work.*

| Head | Symbol | No. of hole | Dimension (mm) | Area/hole ($mm^2$) | Total hole area ($mm^2$) / % opening |
|---|---|---|---|---|---|
| Disintegrating head | DH | 6 | d = 8 | 50.24 | 301.44 / 22.9% |
| Slotted head | SH | 16 | 1.62 x 11 | 17.30 | 276.80 / 21.0% |
| Square hole head | QH | 92 | 2.6 x 2.4 | 6.24 | 574.08 / 43.6% |
| Rectangular slotted head | RSH | 16 | 1.6 x 14.7 | 23.52 | 376.32 / 28.6% |
| Wide slotted head | WSH | 16 | 2.4 x 14.7 | 35.28 | 564.48 / 42.8% |
| Rectangular slotted head 6 | RSH6 | 6 | 1.62 x 14.7 | 23.81 | 142.86 / 10.8% |
| Wide slotted head 6 | WSH6 | 6 | 3.4 x 14.7 | 49.98 | 299.88 / 22.8% |
| Thick wide slotted head 6 | TWSH | 6 | 3.4 x 14.7 | 49.98 | 299.88 / 22.8% |
| Thick disintegrating head | TDH | 6 | d = 8 | 50.24 | 301.44 / 22.9% |

% opening is calculated based on the inner surface of the stator.

Both RSH and WSH are similar to SH, however, the holes in RSH and WSH have squared edges and perpendicular to the stator surfaces, while those in SH have tapered edges and some degree of inclination relative to the stator surface (see *Fig. 6.4*). WSH6 has the same total hole area as DH but with rectangular shape rather than circular allowing the investigation of the effect of hole shape on the flowrate and power number. RSH6 has the same hole dimension as RSH, but with six holes instead of sixteen which enables the investigation of the effect of hole spacing.

The mixing head was placed symmetrically in the middle of an un-baffled, flat bottom vessel of diameter 150 mm as explained in the previous chapter. All simulations were run at 4000 rpm ($Re$ = 52,000) with water at 20 $^{o}$C as the working fluid. The boundary conditions, discretization schemes and time steps used in here were discussed in details in the previous chapter. The simulations were also run serially in Blue BEAR (Birmingham Environment for Academic Research) cluster.

## 6.3. Fabrications of slotted and square hole heads

Experiments revealed that both SH and QH produced different flow patterns in the bulk liquid when the stators were installed in inverted position. LDA measurements of bulk tangential velocity at "normal" (solid symbol) and inverted (empty symbol) positions are shown in *Fig. 6.2* and *Fig. 6.3* for SH and QH respectively. The "normal" position is defined as the stator position which generates stronger bulk motion against rotor rotation. In case of SH, bulk liquids move against the rotor rotation in both positions but the tangential velocity is larger in "normal" position than in inverted position. In case of QH, bulk liquid moves against rotor rotation only in "normal" position but moves with rotor rotation in inverted position. These results show that SH and QH are not symmetrical. This lack of symmetry was caused by the manufacturing processes of those heads as illustrated in *Fig. 6.4* and *Fig. 6.5* for SH and QH respectively.

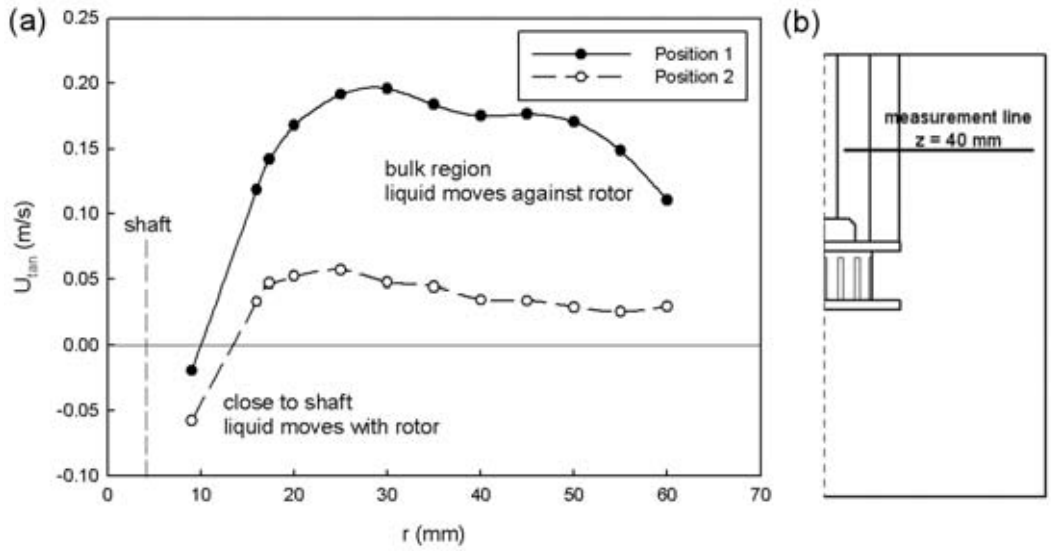


***Fig. 6.2.*** *(a) Comparison of bulk tangential velocity of slotted head (SH) at 4000 rpm when it is installed in normal position (position 1) and in inverted position (position 2), (b) position of the measurement. Rotor rotates in negative $\theta$ direction.*

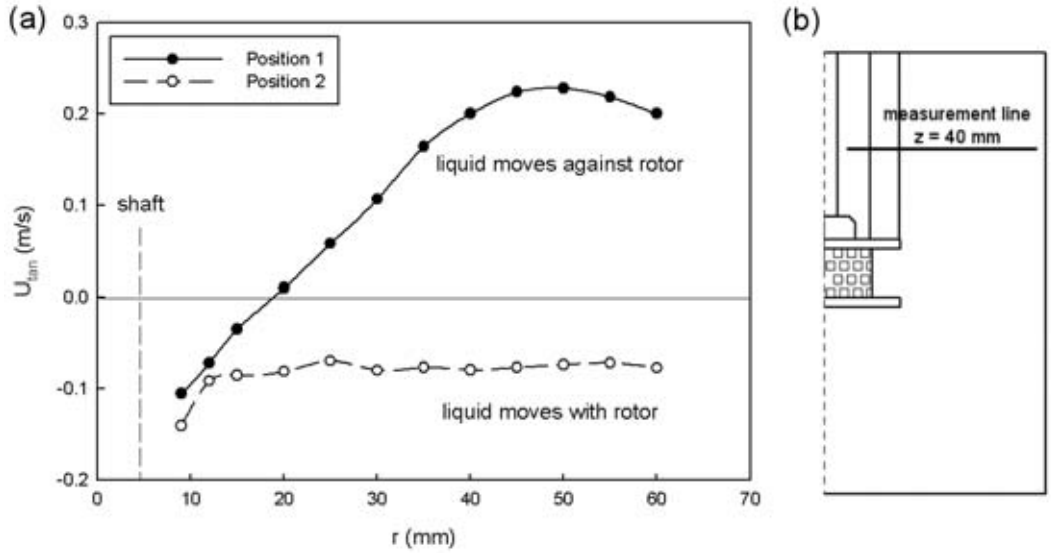


***Fig. 6.3.*** *(a) Comparison of bulk tangential velocity of square hole head (QH) at 4000 rpm when it is installed in normal position (position 1) and in inverted position (position 2), (b) position of the measurement. Rotor rotates in negative $\theta$ direction.*

The SH was manufactured from a pipe and the slots were made by using a circular grinder (*Fig. 6.4*), therefore the slots have tapered ends and trapezoidal cross section of height 11 mm at the inner radius of the stator and 14.7 mm at the outer radius (see Chapter V, *Fig. 2(b)*). During manufacturing process, there seemed to be a small offset between the centers of the pipe and grinder which made the radial axis of the slot deviated from the normal through the slot center by $\pm \alpha$ (*Fig. 6.4(b)* and *(c)*). However, it was difficult to measure the exact $\alpha$ and in this work it was estimated to be $7^o$ (offset = 2 mm). This feature differentiates SH from modified slotted heads (RSH and WSH, *Fig. 6.1(a)* and *(b)*). The holes in the modified slotted heads have rectangular cross section and are perpendicular to the stator surface ($\alpha = 0$). The slotted head simulated previously (see Chapter V) had $\alpha = +7^o$. Otherwise stated, the term slotted head in this chapter refers to the one with $\alpha = +7^o$ (*Fig. 6.4(c)*).

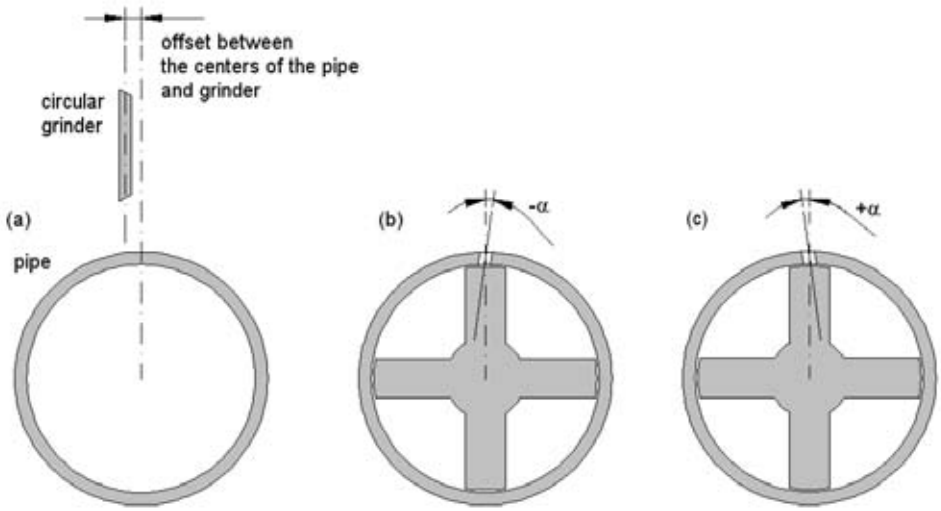


***Fig. 6.4.*** *Manufacturing process of the slotted head (SH). (a) The slot on the slotted head is made by a circular grinder and there is an offset between the centers of the pipe and grinder, (b) the slot axis deviates from the normal by $-\alpha$ and (c) by $+\alpha$ when it is installed in inverted position (private communication with Silverson representative).*

The QH was made from flat plate, punched and rolled into a cylindrical shape. This rolling process deformed the holes, however, it is difficult to estimate the exact shapes of those holes and therefore the holes in the CFD model (*Fig. 6.5(d)*) were perfectly square and perpendicular to the stator surface.

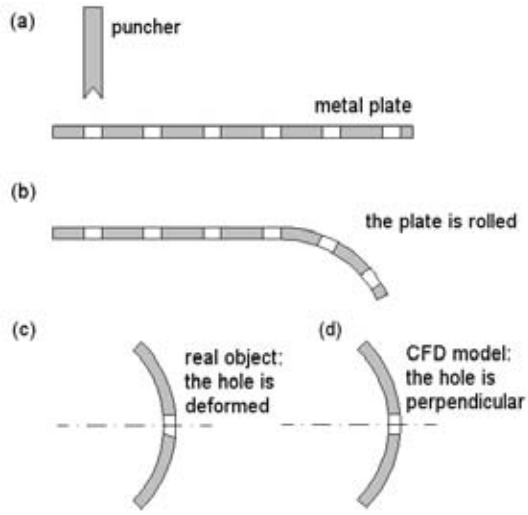


***Fig. 6.5.*** *Manufacturing process of the square hole head (QH). (a) The square hole head is made by punched a flat metal plate and (b) rolled it into cylindrical shape. (c) This rolling process deforms the hole, however (d) the hole in the CFD model is square (private communication with Silverson representative).*

## 6.4. Results and Discussions

### 6.4.1 Flow patterns in the holes and bulk regions

The flow patterns in the holes of various stators are shown in *Fig. 6.6*. The tangentially moving liquid inside stators starts moving in radial direction once it reaches the trailing edges of stator holes. Therefore, shear layers exist between high velocity streams emerging from rotor swept volumes and relatively stagnant liquid in the holes. When the blades do not overlap with the holes, the angle between the shear layer and tangent at the trailing edge in each stators ($\gamma$ in *Fig. 6.6(a)*) varies slightly from 20 to 30$^{o}$. It also depends on the blade positions.

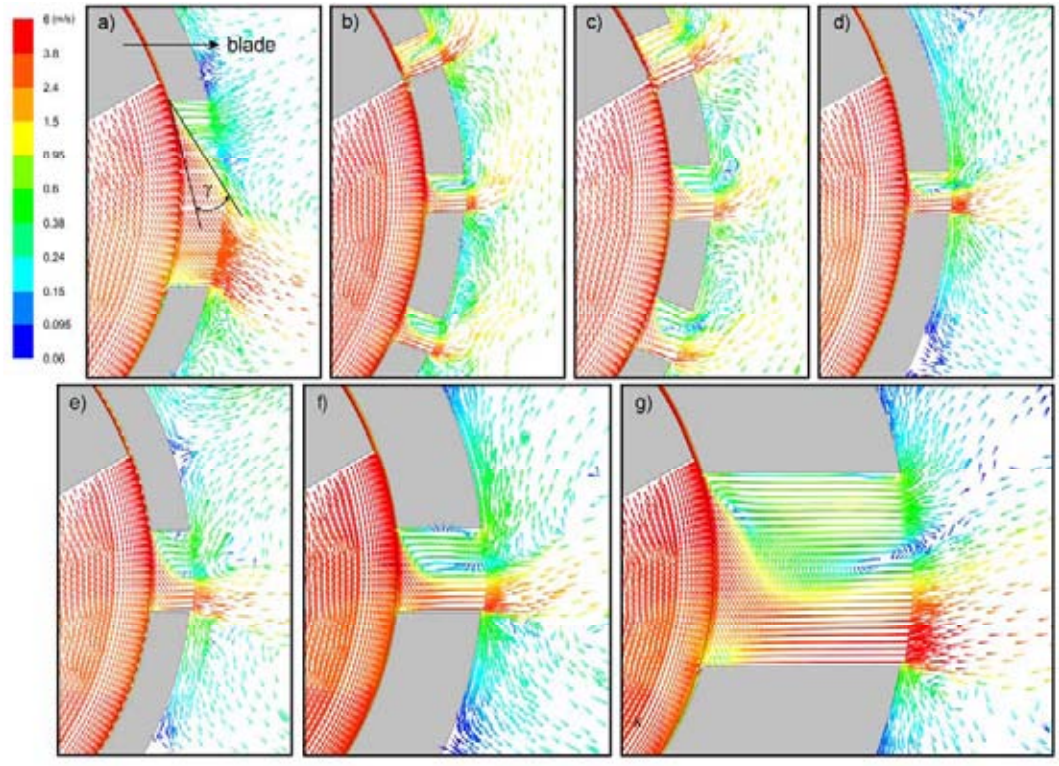


***Fig. 6.6.*** *Flow patterns in the holes of different stators: (a) DH, (b) RSH, (c) WSH, (d) RSH6, (e) WSH6, (f) TWSH and (g) TDH.$\gamma$ represents the angle between the shear layer and tangent at the trailing edge. All velocity vectors are taken at plane z = 0, except for DH at z = -0.8 and QH at z = 1.3 mm.*

These streams of high velocity liquid will eventually hit the leading edges where tangential momentum is converted into radial momentum. For stator with wide holes, such as DH, only part of this stream hits the leading edge and the emerging jet still has some tangential momentum in the same direction as rotor. For stators with narrow holes, the whole streams hit the leading edges and the emerging jets are directed by those edges. However, for thicker stators, i.e. TWSH (*Fig. 6.6(f)*) and TDH (*Fig. 6.6(g)*), the emerging jets are entirely directed by the leading edges and the flow patterns in the holes of those stators are practically the scale-up version of that of RSH6 (*Fig. 6.6(d)*).

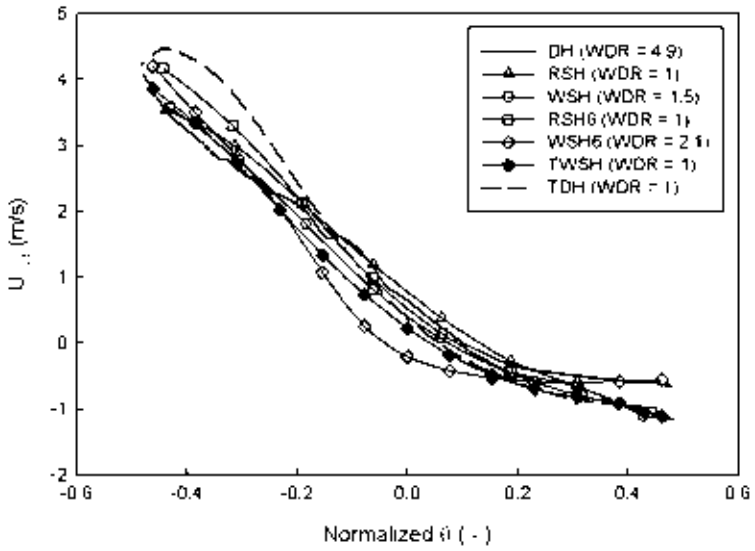


***Fig. 6.7.*** *Jet radial velocity profiles of various stators taken at stators outer surfaces (r = 15.9 mm except for TWSH and TDH at r = 17.475 mm and r = 22.275 mm respectively) and at z = 0 except for DH and TDH at z = -0.8 mm. Normalized θ is defined as θ divided by the angle between the leading and trailing edges, β (see Chapter V, Fig. 9).*

The radial velocity profiles of jets emerging from various stators plotted against normalized θ (see Chapter V, *Fig. 9*) are practically the same as shown in *Fig. 6.7.* The jets tangential velocity profiles (*Fig. 6.8*) of various stators, however, are affected by widh-to-depth ratio (WDR) of the holes. The jet

tangential velocity increases i.e. becomes more positive when hole WDR decreases. TWSH and TDH, which are the thicker versions of WSH6 and DH respectively and hence have lower holes WDR, have higher jet tangential velocity than WSH6 and DH respectively. This confirms the hypothesis made in the previous work. However, *Fig. 6.8* also shows that RSH has higher jet tangential velocity than RSH6 although their hole WDR is the same suggesting that jet tangential velocity is also affected by hole spacing.

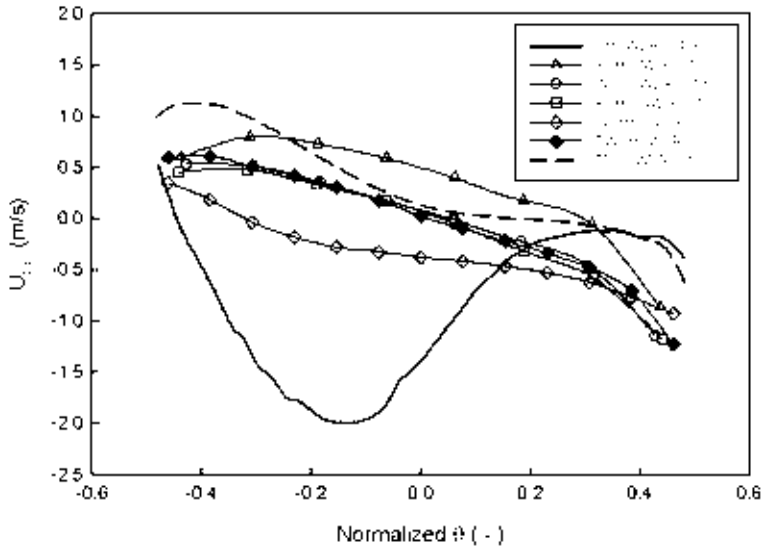


***Fig. 6.8.*** *Jet tangential velocity profiles of various stators taken at stators outer surfaces (r = 15.9 mm except for TWSH and TDH at r = 17.475 mm and r = 22.275 mm respectively) and at z = 0 except for DH and TDH at z = -0.8 mm. Normalized θ is defined as θ divided by the angle between the leading and trailing edges, β (see Chapter V, Fig. 9).*

The bulk flow patterns of various stators are shown in *Fig. 6.9*. The bulk flow patterns of RSH and WSH (*Fig. 6.9(b)* and *(c)* respectively) are very similar to those of SH and QH (see Chapter V, *Fig. 6(b)* and *(c)* respectively). Jets emerging from those stators interact with each other and merge. This interaction increases jet tangential velocity and the emerging jets move tangentially in the counter clockwise direction. Therefore jet tangential velocity of RSH is higher

than that of RSH6 although the holes in both stators have the same WDR. The jets decay in the proximity of the mixing heads and induce body rotation in the bulk region similar to that in an unbaffled vessel.

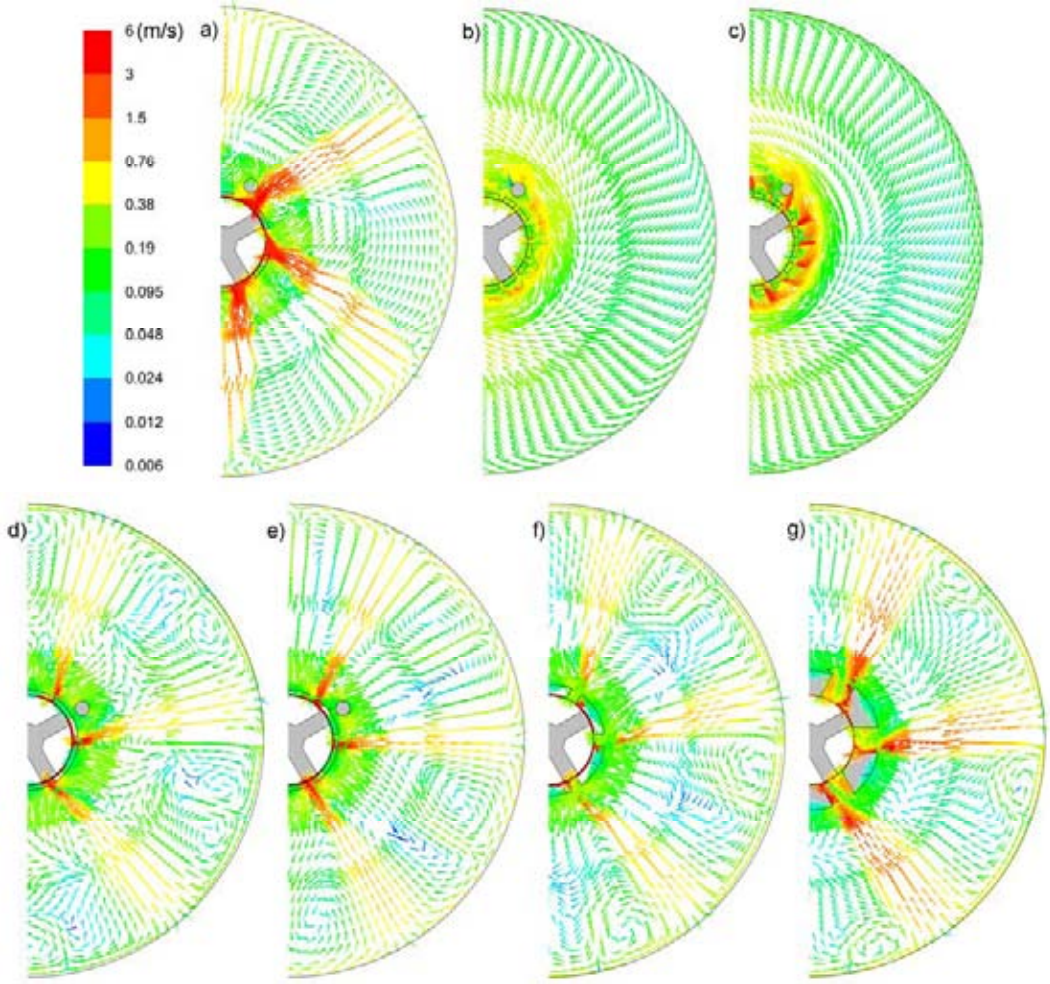


***Fig. 6.9.*** *Flow patterns in the proximity of the mixing heads and in the bulk regions (radial and tangential velocities) of (a)DH, (b) RSH, (c) WSH, (d) RSH6, (e) WSH6, (f) TWSH and (g) TDH. All velocity vectors are taken at plane z = 0 except for DH and TDH at plane z = -0.8 mm.*

In the previous chapter, it was thought that jets emerging from SH and QH decay quickly in the proximity of the mixing heads because smaller jets have larger interfacial area (the boundary between the jet and surrounding liquid) and therefore exchange momentum more quickly with the surrounding fluids than the bigger jets emerging from DH. However, results discussed above suggest that jets

emerging from stators with close hole spacing decay quickly in the proximity of the mixing head because they tend to merge and move in tangential direction.

The jets emerging from stators with six holes tend to behave like free jets due to larger spacing between holes (*Fig. 6.9(a), (d), (e), (f)* and *(g)*). They tend to move radially and are able to reach tank wall where their radial momentum is converted into tangential momentum creating small circulations in the bulk regions. The effect of hole WDR on the bulk flow can be observed by comparing the flow in DH (*Fig. 6.9(a)*) and TDH (*Fig. 6.9(g)*). In DH, jets move in clockwise direction after hitting on the tank wall, while in TDH, jets move in counter clockwise direction after hitting on the tank wall. This difference is more obvious in the horizontal planes above and below the mixing head as shown in *Fig. 6.10(a)* and *(b)* for TDH and *Fig. 7(a)* and *(b)* in Chapter IV for DH.

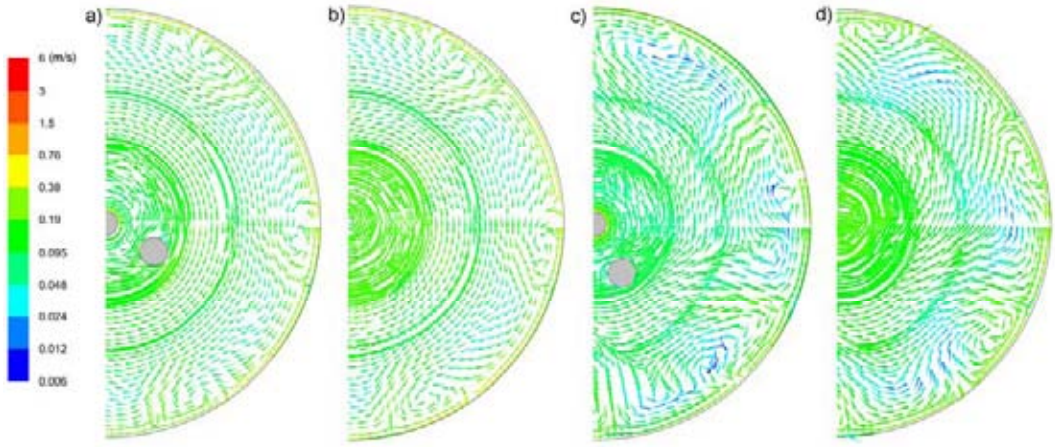


***Fig. 6.10.*** *Flow patterns of (a) TDH at plane z = 0.04 m (above the mixing head), (b) TDH at plane z = -0.04 m (below the mixing head), (c) RSH6 at plane z = 0.04 m (above the mixing head) and (d) RSH6 at plane z = -0.04 m (below the mixing head).*

However, the direction of bulk flow, i.e. whether it is in clockwise or counter clockwise, is not only determined by jet tangential velocity. Jets emerging from RSH6 have positive tangential velocity, i.e. they move in counter clockwise

direction (*Fig. 6.8*) and they create a chaotic flow pattern in the bulk region at a horizontal plane across the middle of the mixing head (*Fig. 6.9(d)*). But at horizontal planes above and below the mixing head (*Fig. 6.10(c)* and *(d)*), bulk liquid moves in clockwise direction. This is because the bulk flow is also driven by rotor through bottom opening (see Chapter V, *Fig. 1(a)*) to move in the same direction as rotor (clockwise direction). Therefore, the bulk flow is determined by jets emerging from the holes and direct action of rotor. Jets emerging from TDH are much larger than those emerging from RSH6 and therefore they can overcome the flow induced by the rotor. Similarly, jets emerging from RSH with sixteen holes can also overcome the flow induced by the rotor but jets emerging from RSH6 with six holes can not.

### 6.4.2 The effect of hole orientation

As discussed previously, the hole orientation in SH deviated from the normal trough its center by $\alpha$. Due to the difficulty to measure the exact deviation angle ($\alpha$), it was estimated to be $7^o$ in CFD model. Therefore, the holes in SH have $\alpha = +7^o$ in "normal" position, but they have $\alpha = -7^o$ in inverted position. The simulation results for SH with $\alpha = +7^o$ have been shown in previous section (see Chapter V, *Fig. 5(b), Fig. 6(b) and Fig. 7(b)*). In this section, the simulation results for SH with $\alpha = -7^o$ will be compared with those for SH with $\alpha = +7^o$ and RSH whose holes have $\alpha = 0$.

The flow patterns in the holes of SH, $\alpha = -7^o$, RSH and SH, $\alpha = +7^o$ are compared in *Fig. 6.11*. The general flow pattern in the hole, i.e. jet emerges in the

proximity of the leading edges and circulation flow occurs behind the jets, is still the same regardless of hole orientations. The jet radial velocity profile across the hole is practically not affected by the hole orientation (*Fig. 6.12*), however, the jet tangential velocity profile is greatly affected by hole orientation (*Fig. 6.13*).

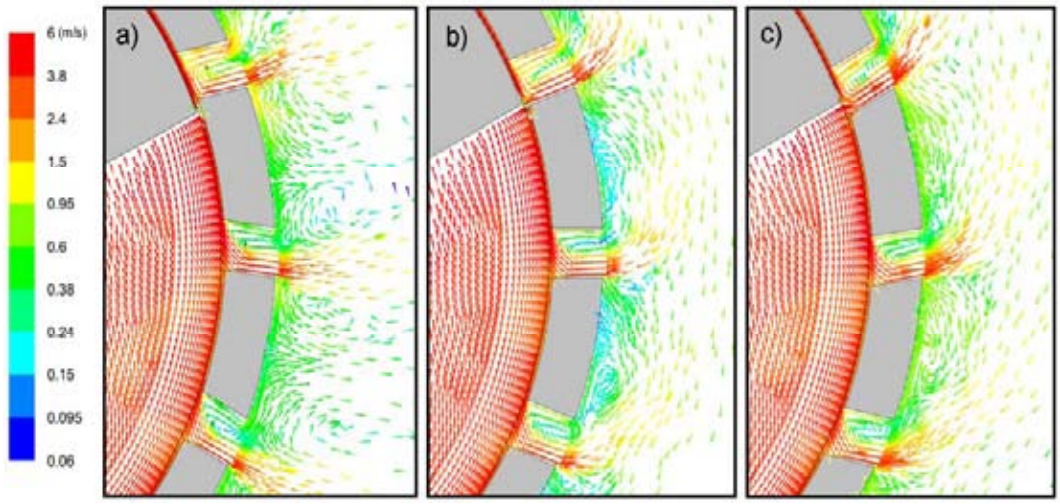


***Fig. 6.11.*** *Flow patterns in the holes of (a) SH, $\alpha = -7^o$, (b) RSH, $\alpha = 0$ and (c) SH, $\alpha = +7^o$. The velocity vectors are taken at plane z = 0.*

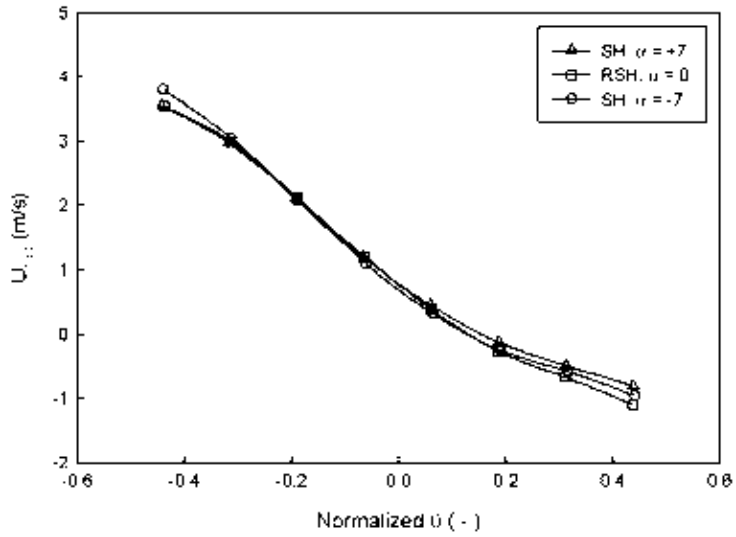


***Fig. 6.12.*** *Effect of hole orientation on time averaged jet radial velocity profiles. The velocity profiles are measured along line r = 15.9 mm (see Chapter V, Fig. 9) and z = 0.*

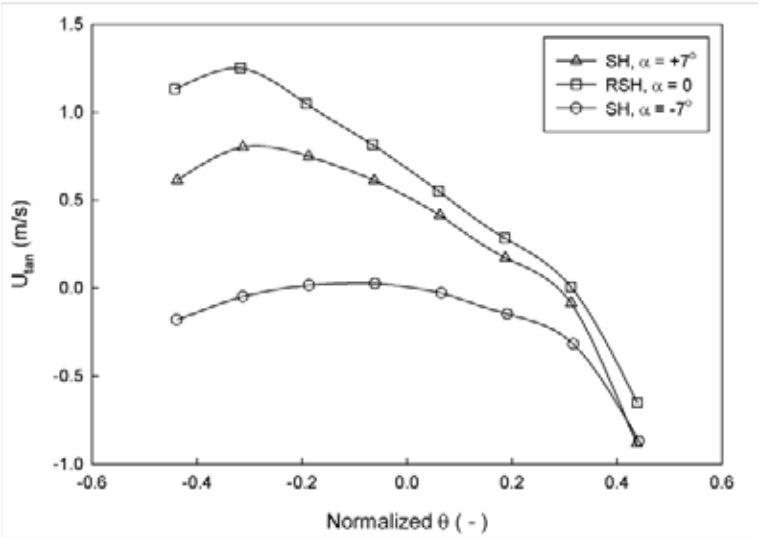


***Fig. 6.13.*** *Effect of hole orientation on time averaged jet tangential velocity profiles. The velocity profiles are measured along line r = 15.9 mm (see Chapter V, Fig. 9) and z = 0.*

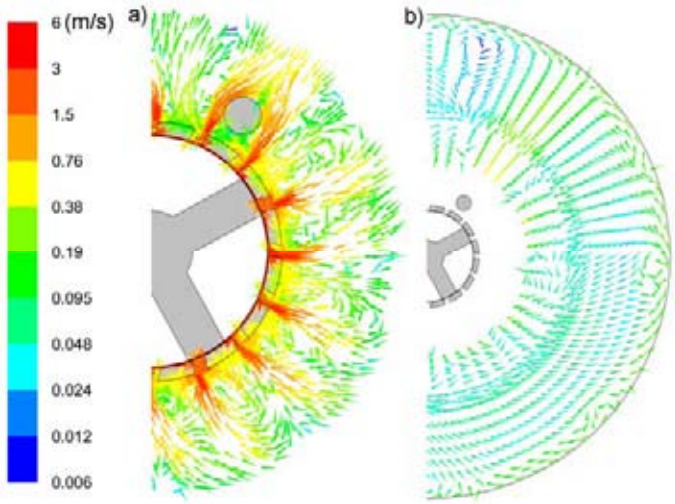


***Fig. 6.14.*** *Flow patterns (a) around the mixing head and (b) in the bulk region of SH, $\alpha = -7^o$. The velocity vectors are taken at plane z = 0.*

The holes in SH ($\alpha = -7^o$ and $\alpha = +7^o$) and RSH have small WDR therefore jets emerging from those holes are directed by the leading edges. Jets emerging from RSH ($\alpha = 0$) have positive tangential velocity. The hole with positive $\alpha$ (SH, $\alpha = +7^o$) increases jet tangential velocity while that with negative $\alpha$ (SH, $\alpha = -7^o$) decreases jet tangential velocity. Jets emerging from SH, $\alpha = +7^o$

and RSH move tangentially in the counter clockwise direction, while those emerging from SH, $\alpha = -7^o$ move radially. Therefore the bulk tangential velocity of SH, $\alpha = -7^o$ is lower than that of SH, $\alpha = +7^o$.

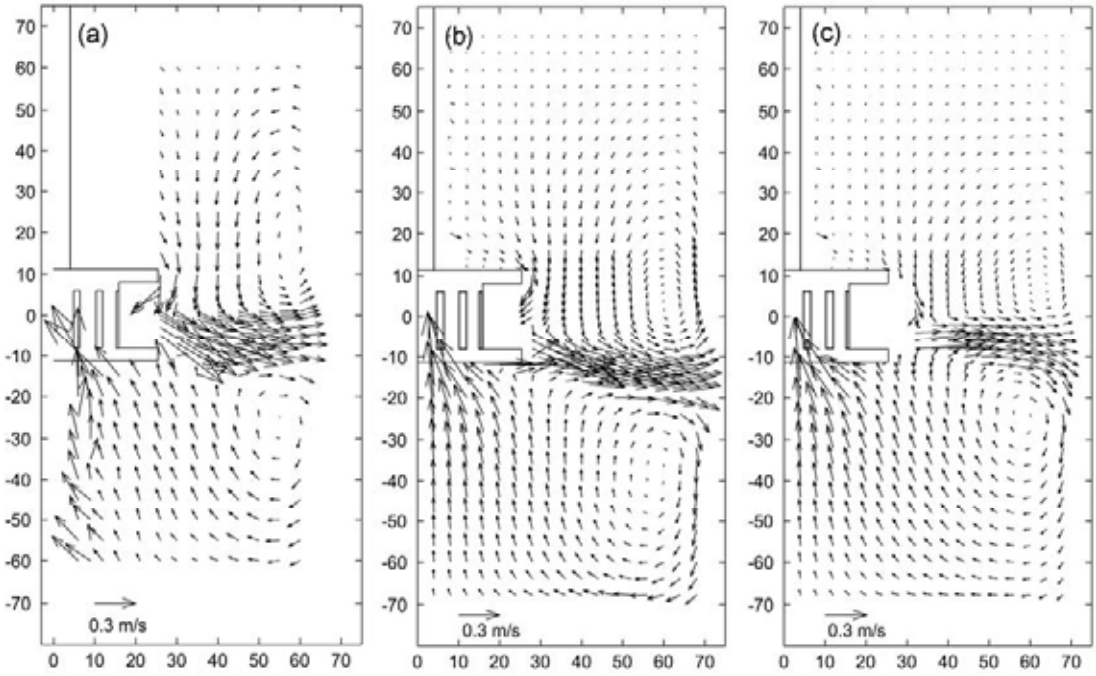


***Fig. 6.15.*** *Axial-radial velocity profiles (in planes $\theta = 0$) of (a) SH ( positive $\alpha$, LDA data), (b) SH ($\alpha = +7^o$, CFD) and (c) RSH ( $\alpha = 0$, CFD). Dimensions in mm.*

The comparison of axial-radial velocity profiles in a vertical plane across $\theta = 0$ between LDA measurement and CFD prediction are shown in *Fig. 6.15(a)* and *(b)* respectively. In the vertical plane, jets emerging from the mixing head move towards tank wall in a curve line, i.e. they go downward and then slightly upward. When they hit tank wall, they create circulation loops in bulk region above and below the mixing head. This pattern is well predicted by CFD, but the jet position is slightly lower than that measured by LDA. This is may be due to the difference between CFD model and real stator. *Fig. 6.15(c)* shows the

predicted flow pattern of RSH where the holes have $\alpha = 0$. Jets move toward tank wall in a straight line rather than in a curve line.

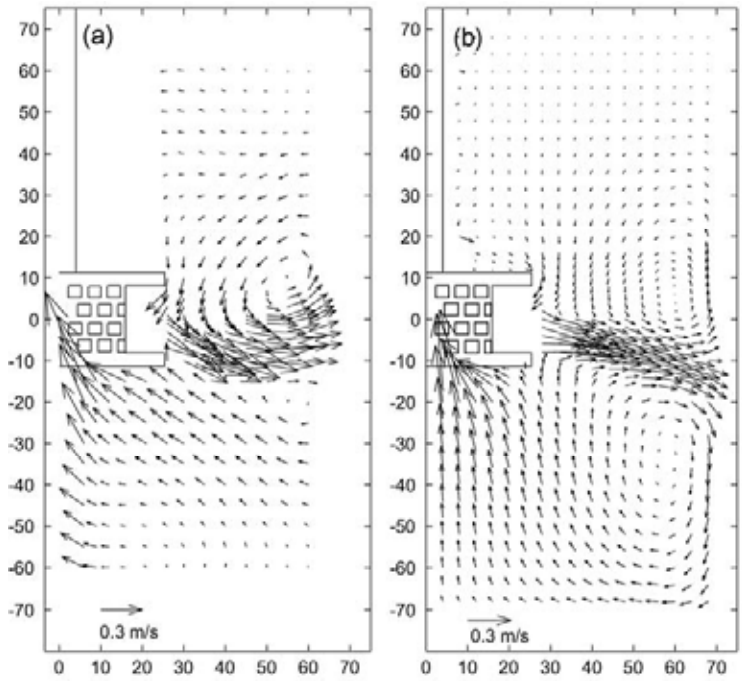


***Fig. 6.16.*** *Axial-radial velocity profiles (in planes $\theta = 0$) of (a) QH (LDA data, "normal" position, positive $\alpha$) and (b) QH (CFD, $\alpha = 0$ CFD). Dimensions in mm.*

*Fig. 6.16(a)* and *(b)* show the axial-radial velocity profiles of QH measured by LDA and predicted by CFD. The holes of real stator have positive $\alpha$ while those of CFD model are perpendicular to the stator surface ($\alpha = 0$). The jets emerging from the real stator move in a curved line while those emerging from CFD model move in the straight line with negative slope. This difference might be because the real stator generates stronger tangential movement in the bulk region since its holes have positive $\alpha$ orientation.

### 6.4.3 Torque and flowrate

The total flowrates and torques of various stators fluctuate as a function of blade position as shown in *Fig. 6.17* and *Fig. 6.18* respectively. The periods of torque and flowrate fluctuations are $30^{o}$ and $22.5^{o}$ for stators with six holes and sixteen holes respectively. The amplitudes of flowrate fluctuations of DH, TDH and RSH are about 2% of their time averaged values, while those of WSH and TWSH can reach up to 4% of their time averaged values. The amplitudes of torque fluctuations of RSH, WSH6, TWSH, where the holes are narrower than the blade, can vary from about 80% to more than 100% from their time averaged values, while those of DH and TDH, where the holes are wider than the blade, are only about 30% from their time averaged values. The positions of the blades in various stators relative to the holes when the torques are maximum are shown in *Fig. 6.19*.

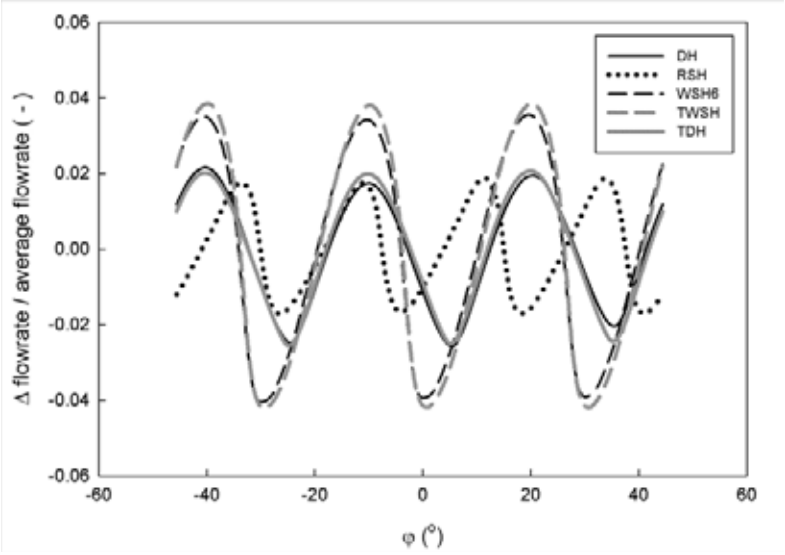


***Fig. 6.17.*** *Fluctuations of flowrates of various stators as a function of blade position (φ). Δ flowrate is the deviation of flowrate from its time averaged value.*

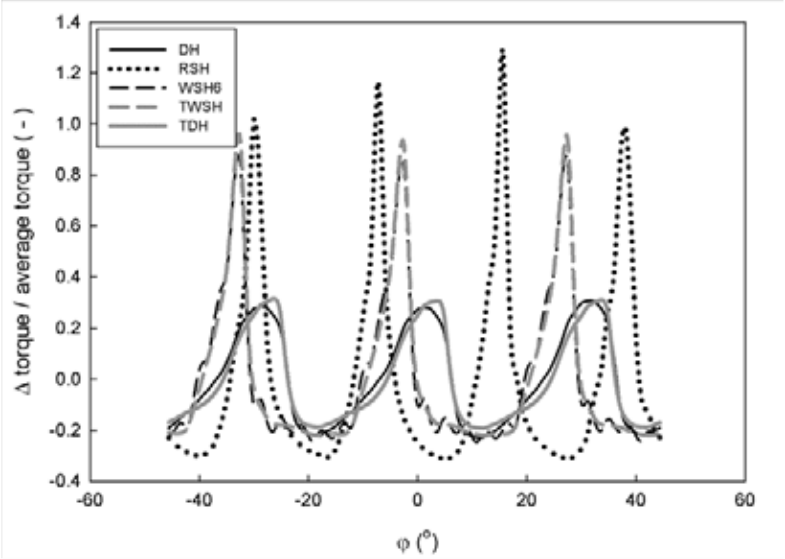


***Fig. 6.18.*** *Fluctuations of torques of various stators as a function of blade position (φ). Δ torque is the deviation of torque from its time averaged value.*

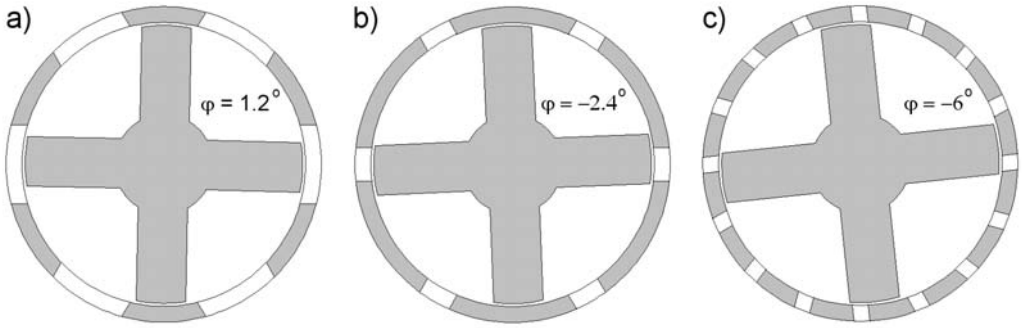


***Fig. 6.19.*** *Positions of the blades relative to the holes when the torques are maximum in (a) DH, (b) RWH6 and (c) RSH.*

The prediction of time averaged total flowrates and power numbers calculated from time averaged torques for all investigated stators are shown in *Table 6.2*. The simulations show that there is practically no effect of hole orientation (SH, $\alpha = +7^o$ and SH, $\alpha = -7^o$) on the flowrate and power number. The effect of hole shape on the flowrate and power number can be observed on DH where the holes are circular and WSH6 where the holes are rectangular. The simulations predict that DH has about 7% higher flowrate than WSH6, but the

power number of WSH6 is about 4% higher than that of DH. Therefore, the simulation shows that the effects of hole shape on the flowrate and power number are very small. These differences could be because the holes in DH are fully covered by the rotor blade, while those in WSH6 are not (*Fig. 6.20*).

***Table 6.2.*** *Flowrates and the power numbers for various stator geometries at 4000 rpm*

| Stator | Total hole area ($mm^2$) | % opening | Flowrate (kg/s) | *Po* (simulation) |
|---|---|---|---|---|
| DH | 301.44 | 22.9% | 0.268 | 1.53 |
| SH $\alpha = +7^o$ | 276.80 | 21.0% | 0.275 | 1.66 |
| SH, $\alpha = -7^o$ | 276.80 | 21.0% | 0.276 | 1.64 |
| QH | 574.08 | 43.6% | 0.389 | 2.05 |
| RSH | 376.32 | 28.6% | 0.358 | 1.96 |
| WSH | 564.48 | 42.8% | 0.408 | 2.13 |
| RSH6 | 142.86 | 10.8% | 0.158 | 1.32 |
| WSH6 | 299.88 | 22.8% | 0.251 | 1.60 |
| TWSH | 299.88 | 22.8% | 0.256 | 1.57 |
| TDH | 301.44 | 22.9% | 0.265 | 1.66 |

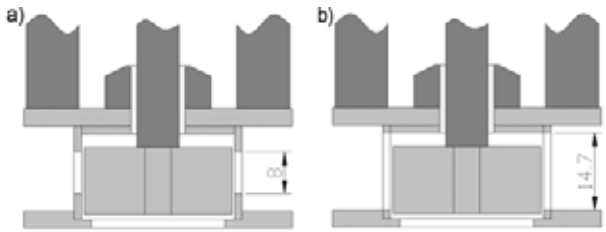


***Fig. 6.20.*** *Position of the rotor relative to the holes in (a) the holes are fully covered by passing blade in DH and (b) the holes are only partially covered by passing blade in WSH6.*

The simulations also predict that the effects of stator thickness on the flowrate and power number are very small. TWSH with stator thickness twice of WSH6 has practically the same flowrate and power number as WSH6. TDH with stator thickness five times of DH has practically the same flowrate as DH but about 10% higher power number than DH (*Table 6.2*). Therefore, it can be concluded that stator thickness has negligible effects on the flowrate and power number.

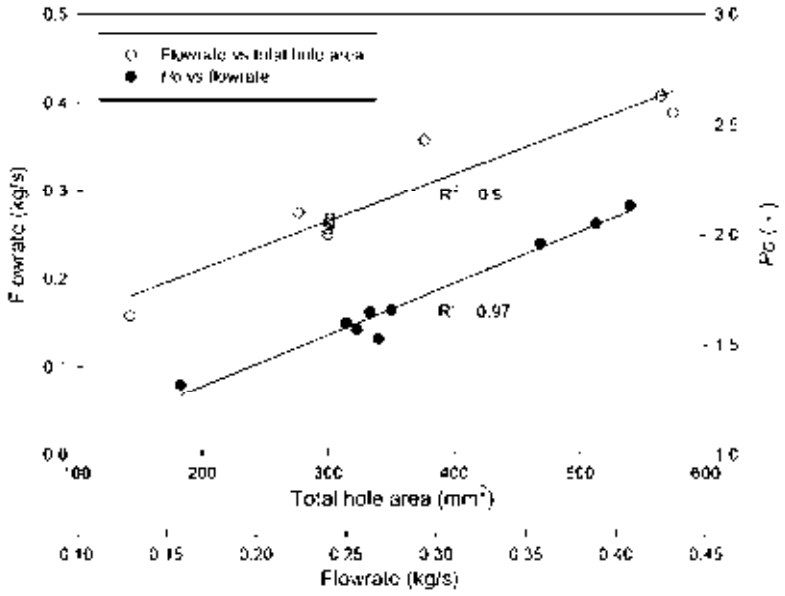


***Fig. 6.21.*** *Correlation of flowrate against total opening area and the power number against flowrate of all stators investigated.*

The total hole areas of stators investigated in this work vary from 10% (RSH6) to more than 40% (QH and WSH) and simulation results still show that flowrate strongly correlate with total hole area and the power number strongly correlate with flowrate (*Fig. 6.21*). These results confirm and extend the results reported in Chapter V.

### 6.4.4 Energy dissipation rate and distribution of energy

*Fig. 6.22* compares the contours of energy dissipation rate of SH, $\alpha = +7^{o}$, RSH and SH, $\alpha = -7^{o}$. The magnitude of energy dissipation rate in the holes of those stators is practically the same and it is not affected by hole orientation. *Fig. 6.23* compares the contours of energy dissipation rate of DH and TDH, while *Fig. 6.24* compares those of RSH6, WSH6 and TWSH. The simulations show that increasing the thickness of leading edges does not increase the magnitude of

energy dissipation rate in the hole nor does it create larger region with high energy dissipation rate in the proximity of the leading edge. It only slightly alters the shape of region with high energy dissipation rate. The contour of energy dissipation rate in the hole, especially the regions with high energy dissipation rate, of TWSH is more similar to that of WSH6 than to RSH6 although the holes in both stators have the same WDR (*Fig. 6.24*).

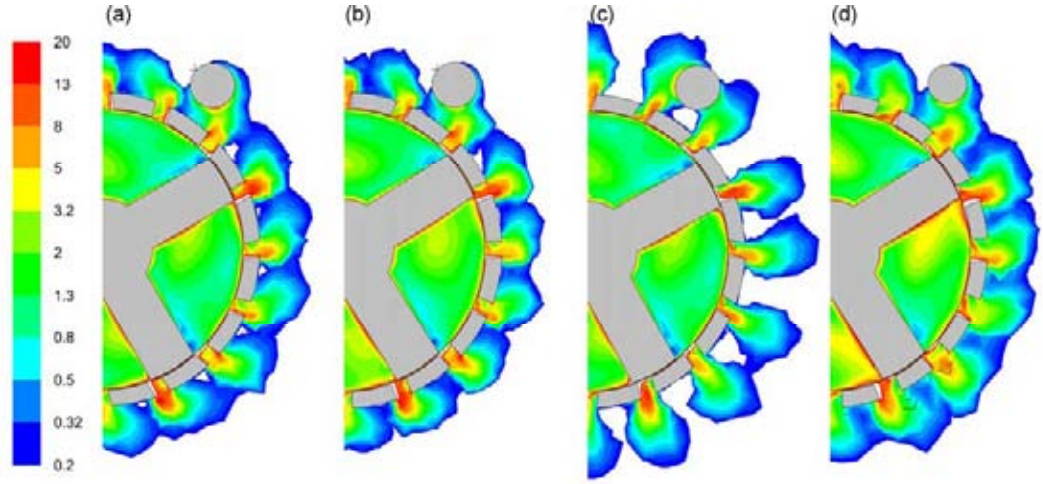


***Fig. 6.22.*** *Contours of energy dissipation rate (normalized by $N^3D^2$) of (a) SH, $\alpha = +7^o$, (b) RSH (a = 0), (c) SH, $\alpha = -7^o$ and (d) WSH.*

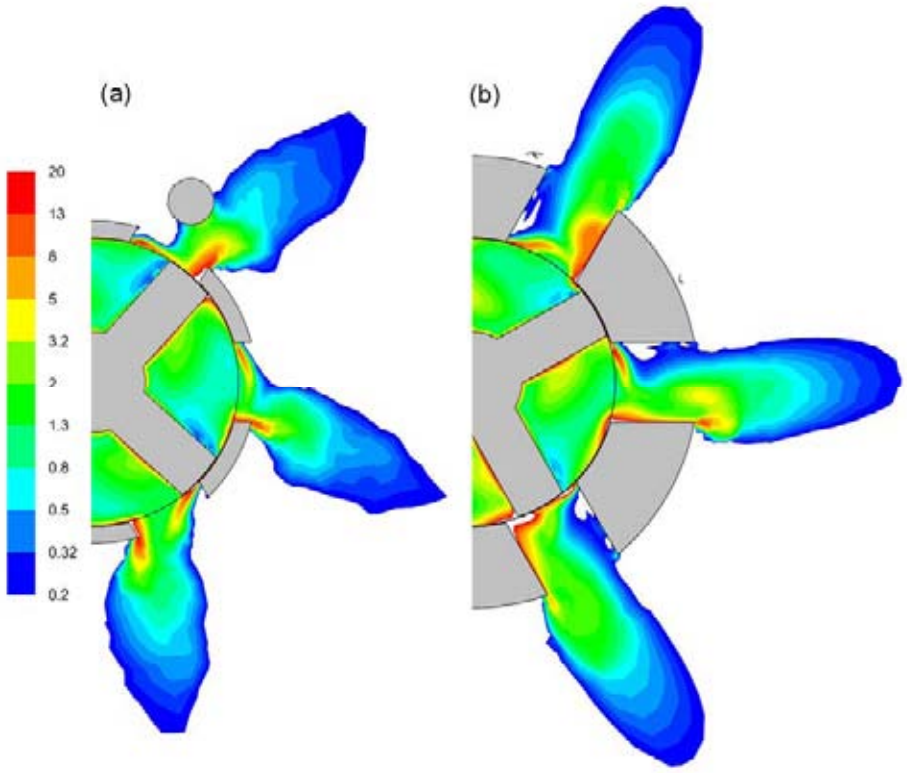


***Fig. 6.23.*** *Contours of energy dissipation rate (normalized by $N^3D^2$) of (a) DH and (b) TDH.*

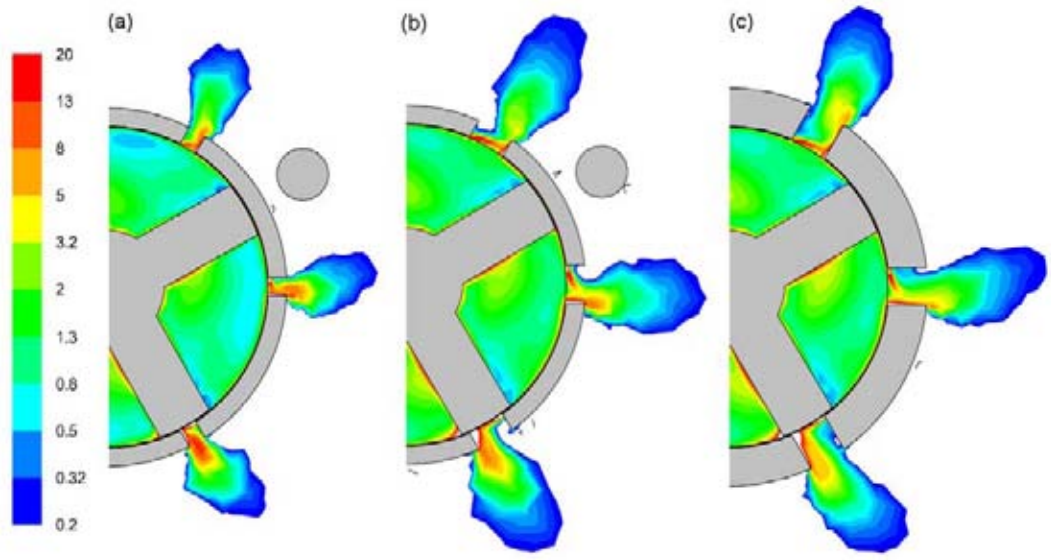


***Fig. 6.24.*** *Contours of energy dissipation rate (normalized by $N^3D^2$) of (a) RSH6, (b) WSH6 and (c) TWSH.*

*Table 6.3* shows that the amount of energy dissipated in the hole region of TDH is only 2.4 times larger than that of DH although the thickness of TDH is five times thicker than that of DH. Similarly, increasing the thickness of WSH6 by a factor of two (TWSH) only increases the amount of energy dissipated in the hole by about 60%. Therefore the average energy dissipation rate per unit mass in the hole regions of thicker stators is lower than that in standard thickness stators.

***Table 6.3.*** *Distribution of energy dissipated in the vessel.*

| Stator | Rotor swept region (W) / (%) | Hole region (W) / (%) | Jet region (W) / (%) | Rest of the tank (W) / (%) | Total (W) |
|---|---|---|---|---|---|
| DH | 3.14 (47.1) | 0.56 ( 8.4) | 1.58 (23.7) | 1.39 (20.8) | 6.67 |
| SH | 3.73 (54.9) | 0.99 (14.6) | 1.73 (25.4) | 0.35 ( 5.1) | 6.80 |
| QH | 4.97 (60.3) | 0.99 (12.0) | 2.18 (26.5) | 0.10 ( 1.2) | 8.24 |
| RSH | 4.68 (57.4) | 1.27 (15.6) | 2.08 (25.5) | 0.13 ( 1.6) | 8.16 |
| WSH | 5.30 (58.4) | 1.37 (15.1) | 2.27 (25.0) | 0.14 ( 1.5) | 9.08 |
| RSH6 | 2.90 (53.6) | 0.41 ( 7.7) | 1.13 (20.8) | 0.97 (17.9) | 5.41 |
| WSH6 | 3.55 (51.7) | 0.66 ( 9.6) | 1.59 (23.1) | 1.07 (15.6) | 6.87 |
| TWSH | 3.61 (53.1) | 1.04 (15.3) | 1.37 (20.1) | 0.96 (14.1) | 6.79 |
| TDH | 3.74 (50.4) | 1.37 (18.5) | 0.73 ( 9.9) | 1.58 (21.3) | 7.42 |

The amount of energy dissipated in a particular region was calculated by integrating the energy dissipation rate over that region. The definition of each region is shown in *Chapter IV, Fig. 25*.

*Table 6.3* shows that stators with small hole spacing (SH, QH, RSH, WSH) dissipate small fraction of energy in the bulk regions while for those with large hole spacing dissipate greater fraction of energy in the bulk regions. This is in agreement with the prediction of velocity profiles of jets emerging from those stators (*Fig. 6.9*). Jets emerging from stators with small hole spacing tend to move tangentially in the proximity of the mixing head, while those emerging from stators with large hole spacing move radially as free jets. On the other hand, the fractions of energy dissipated in the rotor swept regions of stators with small hole spacing are slightly larger (about to 60%) than those of stators with large hole spacing (about 50%). *Table 6.3* also shows that for standard thickness stator,

stators with small hole spacing dissipate larger fraction of energy in the hole regions (above 10%) than those with large hole spacing. This is because stator with small hole spacing have more hole edges where stagnations occur.

## 6.5. Conclusions

The simulations showed that the directions of jets emerging from stator holes were affected by hole width-to-depth ratio, hole orientation and hole spacing. For batch operation, rotor stator mixer is often combined with other impeller to enhance bulk mixing (Myers et al., 1999). Although the flow pattern generated by such combination will be very complex and other studies are required to determine whether the impeller should move with or against the jets emerging from stator holes to enhance bulk mixing, this study suggested that the jets emerging from stator holes were affected by those aforementioned parameters.

However, the flowrates and power numbers were practically not affected by hole width-to-depth ratio, hole orientation and hole spacing. The flowrate correlated strongly with the total hole area whilst the power number strongly correlated with the flowrate. These behaviors have been investigated for stators with total hole areas from 10 to 40% of stator inner surface area.

The contours of energy dissipation rate in the holes and jets of thick stator were more similar to those of standard thickness stator with the same hole width than those with the same hole width-to-depth ratio. This suggests that hole width should be kept constant if scale up procedure is based on the constant tip speed

and constant gap width (Atiemo-Obeng and Calabrese, 2004). However, previous study (Utomo et al., 2008) showed that energy dissipation rate scaled with $N^3$ suggesting that scale-up procedure should be based on constant $N^3D^2$ in the turbulent flow regime. Therefore, further simulations with larger rotor diameter need to be carried out to investigate which scale-up procedure is better (based on constant tip speed, ND, or constant energy dissipation rate, $N^3D^2$) and whether the hole width should be kept constant or scaled-up accordingly.

Stators with close hole spacing dissipated slightly higher fractions of energy in the rotor swept volume and hole regions than stators with large hole spacing. However, stators with large hole spacing dissipated higher fraction of energy in the bulk regions than those with close hole spacing suggesting that stators with large hole spacing can provide better bulk agitation than those with small hole spacing. Therefore, the intensity of movement in the bulk region depends on the hole spacing rather than hole size.

# CHAPTER VII

# CONCLUSIONS AND FUTURE WORKS

## *7.1. Conclusions*

### 7.1.1 Turbulence model

- A relatively simple standard k-ε turbulence model can predict the flow in a rotor-stator mixer with a relatively complex geometry. The agreements between CFD predictions and LDA measurements of velocity profiles in the bulk regions and those of the jets emerging from stator holes were reasonably good.
- The prediction of energy dissipation rate is limited by Reynolds decomposition which underlying the RANS (Reynolds Averaged Navier Stokes) turbulence models. The integrals of energy dissipation rates for different stators over the whole tanks were about 30 – 50% lower than theoretical power input ($Po\rho N^3D^5$).
- The prediction of distribution of energy, however, is in reasonably good agreement with the experimental result. The kinetic energy balance based on LDA data showed that about 70% of energy supplied by the rotor was dissipated in the proximity of the mixing head, while CFD predicted that about 60% of energy was dissipated in the same control volume.

### 7.1.2 The effect of stator geometry on the velocity profile

- The flow pattern in the hole was affected by blade passing, however, there was general flow pattern in the hole regardless of hole shape and dimension. Jet

emerged in the proximity of the leading edge and it induced circulation flow behind it.

- The time averaged jet radial and tangential velocities were proportional to rotor speed.
- Time averaged jet radial velocity profiles of various stators with different hole shapes and dimensions were very similar when they were plotted against normalized $\theta$ (tangential coordinate). However, time averaged jet tangential velocity profiles were affected by hole width-to-depth ratio, hole orientation and hole spacing.
- Jets emerging from holes with large width-to-depth ratio had negative tangential velocity, i.e. moved in the same direction as rotor while those emerging from holes with small width-to-depth ratio had positive tangential velocity, i.e. moved against the rotor.
- Jets emerging from stators with small hole spacing tended to merge due to close distance between them and moved tangentially while those emerging from stators with large hole spacing behaved like free jets and moved radially.

### 7.1.3 The effect of stator geometry on flowrate and torque

- The flowrates and torques with all stators, except square hole stator, fluctuated as a function of blade position relative to the stator holes. Those with square hole stator were relatively constant due to overlapping structure of hole arrangement.
- The time averaged flowrate through stator holes was proportional to rotor speed.

- The time averaged flowrates and power numbers calculated from the time averaged torques were not affected by stator thickness or hole width-to-depth ratio, hole orientation and hole spacing.
- At constant rotor speed, the time averaged flowrate well correlated with the stator total hole area while the power number well correlated with the time averaged flowrate. This behavior was observed for stators with opening areas from 10 to 40% of stator inner surface.

### 7.1.4 The effect of stator geometry on energy dissipation rate

- High energy dissipation rate occurred in the regions around the leading and trailing edges due to stagnation in those regions. However, the maximum energy dissipation rate only occurred periodically when the tip of the blade was in close proximity or was overlapping with the leading edges.
- The contours of energy dissipation rate at different rotor speeds were practically the same when normalized with $N^3D^2$. The kinetic energy balance based on LDA data showed that the energy dissipated in the proximity of the mixing head scaled with $N^3$.
- Stators with narrow hole had more uniform energy dissipation rate profiles across the holes than those with wide holes suggesting that stators with narrow holes can produce a more uniform drop size during emulsification.
- The contour of energy dissipation rate was not significantly affected by stator thickness. The contours of energy dissipation rate in the holes with the same width were similar whilst those with the same hole width-to-depth ratio were different.

- For all stators investigated, most of energy supplied by the rotor was dissipated in the rotor swept region. Stators with small hole spacing dissipated more energy in the rotor swept volume and hole region than those with large hole spacing. However, stator with large hole spacing dissipated more energy in the bulk region suggesting that they were more suitable for bulk agitation than those with small hole spacing.

## 7.2. Recommended future works

- Scale-up

  Rotor-stator mixers are frequently used to produce emulsion and scale-up procedure may vary in different flow regime. In the turbulent regime, Karbstein and Schubert (1995) and Calabrese et al. (2000) have shown that drop broke up due to turbulent eddies. This study has shown that energy dissipation rate scaled with $N^3$. However, further study in larger scale is needed to investigate how the energy dissipation rate will change when this mixer is scaled-up based on constant energy dissipation rate per unit volume ($N^3D^2$) or constant tip speed (ND). Furthermore, whether hole dimension and stator thickness should be kept constant or scaled-up accordingly also need to be investigated.

- The shape of rotor blade

  Khopkar et al. (2007) found that the power constant ($K_p = Po/Re$) in laminar flow of a rotor-stator mixer with curved blade was 2.5 times smaller than that with straight blade. However, the effects of blade shape on the velocity profile,

pumping capacity and energy dissipation rate have not yet been investigated and CFD is a suitable tool to optimize the design of rotor and stator.

- Flow pattern in the laminar and transition regimes

  During emulsification, the viscosity of emulsion increases with the volume fraction of dispersed phase and the decrease of drops size. Therefore the flow in a batch rotor-stator mixer may change from fully turbulent at the beginning of emulsification process to laminar at the end of the process. The flow pattern of emerging jets may be different in the different flow regime and therefore the flow pattern in the laminar and transition regimes need to be investigated and compared with that in the fully turbulent flow regime.

- Particle tracking

  Particle tracking may give information of how droplets travel and are distributed in bulk liquid. The simulations of particle tracking with different ratios of rotor diameter to tank diameter (D/T) can determine the optimum D/T of a batch rotor-stator mixer.

# NOMENCLATURE

## CHAPTER I

| | |
|---|---|
| $D$ | rotor diameter (m) |
| $d_{max}$ | maximum drop diameter (μm) |
| $Fr$ | Froude number ($N^2D/g$) |
| $g$ | earth gravity ($m^2/s$) |
| $k_0$ | constant ( - ) |
| $k_1$ | constant ( - ) |
| $N$ | rotor speed (1/s) |
| $M$ | mass flowrate (kg/s) |
| $P$ | power (W) |
| $P_F$ | power due to flow (W) |
| $P_M$ | power dissipated per unit mass (W/kg) |
| $P_L$ | power loss (W) |
| $Po$ | power number ($P/\rho N^3D^5$) |
| $P_T$ | power due to torque (W) |
| $Re$ | Reynolds number ($\rho ND^2/\mu$) |

*Greek letters*

| | |
|---|---|
| $\delta$ | gap spacing (m) |
| $\rho$ | density ($kg/m^3$) |

## CHAPTER II

| | |
|---|---|
| $C$ | Impeller clearance (m) |
| $C_D$ | constant in one-equation model ( - ) |
| $C_S$ | Smagorinsky coefficient ( - ) |
| $C_\mu$ | constant in standard k-ε model ( - ) |
| $C_{\varepsilon 1}$ | constant in standard k-ε model ( - ) |
| $C_{\varepsilon 2}$ | constant in standard k-ε model ( - ) |
| $D$ | impeller diameter (m) |
| $H$ | tank height (m) |
| $k$ | turbulent kinetic energy per unit mass ($m^2/s^2$) |
| $\ell$ | integral scale (m) |
| $\ell_m$ | mixing length (m) |
| $N$ | impeller speed (1/s) |
| $p$ | instantaneous pressure (Pa) |
| $p'$ | fluctuating component of pressure (Pa) |
| $P$ | time averaged pressure (Pa) |
| $Re_\ell$ | the Reynolds number based on integral scale ($\rho U_i \ell/\mu$) |
| $s_{ij}$ | strain rate based on instantaneous velocity ($m/s^2$) |

$S_{ij}$ strain rate based on time averaged velocity ($m/s^2$)
$\tilde{S}_{ij}$ strain rate based on resolved velocity ($m/s^2$)
$t$ time (s)
$T$ tank diameter (m)
$u_i$ instantaneous velocity in i direction (m/s)
$Ui$ time or ensemble average velocity in i direction (m/s)
$\tilde{u}_i$ filtered velocity in i direction (m/s)
**u** velocity vectors (m/s)
$u_\tau$ friction velocity (m/s)
$u_i'$ fluctuating component in i direction (m/s)
$u_i^R$ residual velocity in i direction (m/s)
$V$ velocity scale (m/s)
$y$ normal distance from wall (m)
$y^+$ normalized $y$ ($yu_\tau/\nu$)

*Greek letters*
$\Delta$ filter width (m)
$\varepsilon$ turbulent energy dissipation rate per unit mass ($m^2/s^3$)
$\eta$ Kolmogorov microscale (m)
$\kappa$ von Karman constant
$\lambda$ Taylor microscale (m)
$\mu$ viscosity (kg/m s)
$\nu$ kinematic viscosity ($m^2/s$)
$\nu_t$ turbulent kinematic viscosity ($m^2/s$)
$\nu_R$ residual kinematic viscosity ($m^2/s$)
$\rho$ density ($kg/m^3$)
$\sigma_k$ constant in standard k-e model ( - )
$\sigma_\varepsilon$ constant in standard k-e model ( - )
$\tau_{ij}$ shear stress (kg/m s)
$\tau_{ij}'$ Reynolds shear stress (kg/m s)
$\tau_{ij}^R$ residual shear stress (kg/m s)

## CHAPTER III

$A$ constant ( - )
$B$ constant ( - )
$C_{i(0\text{-}3)}$ constant ( - )
$d_f$ fringe spacing (m)
$d_0$ beam diameter at its waist (m)
$D_L$ initial beam diameter (m)
$E$ beam expansion ( - )
$E$ Wheatstone bridge voltage (V)
$f_D$ Doppler frequency (1/s)
$f_s$ frequency shift (1/s)

| | |
|---|---|
| $F$ | lens focal distance (m) |
| $h$ | hot wire pitch coefficient ( - ) |
| $k$ | hot wire yaw coefficient ( - ) |
| $L_{IA}$ | length of interrogation area (pixel) |
| $M$ | image magnification (pixel/m) |
| $N_f$ | number of fringe in measurement volume ( - ) |
| $R$ | wavefront radius (m) |
| $u_B$ | binormal velocity component relative to hot wire coordinate (m/s) |
| $u_e$ | effective instantaneous velocity component (m/s) |
| $u_i$ | velocity of particle i (in LDA) (m/s) |
| $u_N$ | normal velocity component relative to hot wire coordinate (m/s) |
| $u_T$ | tangential velocity component relative to hot wire coordinate (m/s) |
| $u_p$ | velocity component perpendicular to fringes (in LDA) (m/s) |
| $U$ | velocity in x direction (in PIV) (m/s) |
| $U_{max}$ | maximum velocity (in PIV) (m/s) |
| $\boldsymbol{V}$ | velocity vector (in HWA) (m/s) |
| $V$ | velocity in y direction (in PIV) (m/s) |

*Greek letters*

| | |
|---|---|
| $\delta_x$ | height of LDA measurement volume (m) |
| $\delta_y$ | width of LDA measurement volume (m) |
| $\delta_z$ | length of LDA measurement volume (m) |
| $\Delta x$ | displacement in x direction (m) |
| $\Delta y$ | displacement in y direction (m) |
| $\Delta t$ | time between double pulse (s) |
| $\lambda$ | wavelength (m) |
| $\rho$ | density (kg/m$^3$) |
| $\theta$ | intersection angle between two beams ($^o$) |

**CHAPTER VI**

| | |
|---|---|
| $D$ | rotor diameter (m) |
| $N$ | rotor speed (1/s) |
| $P$ | power (W) |
| $r$ | radial direction (mm) |
| $Po$ | the power number ($P/(\rho N^3 D^5)$) |
| $U_{rad}$ | radial velocity (m/s) |
| $U_{tan}$ | tangential velocity (m/s) |
| $z$ | axial coordinate (mm) |

*Greek*

| | |
|---|---|
| $\alpha$ | hole orientation ($^o$) |
| $\beta$ | the angle between the leading and trailing edges ($^o$) |
| $\gamma$ | the angle between jet shear layer and tangent at trailing edge ($^o$) |

$\Delta$ the deviation of flowrate or torque from its time averaged value (kg/s) or (N m)
$\varphi$ blade position relative to θ = 0 (°)
$\rho$ density (kg/m$^3$)
$\theta$ tangential coordinate (°)

## APPENDIX A

$A_{ij}$ surface area of the section ij (m$^2$)
$D$ rotor diameter (m)
$D$ diameter of boundaries 2 and 3 of the control volume (m)
$E_{in}$ amount of energy input into the control volume (W)
$E_{diss}$ amount of energy dissipated in the control volume (W)
$E_{out}$ amount of energy out of the control volume (W)
$E_{rotor}$ amount of energy supplied by rotor (W)
$h$ height of boundary 2 of the control volume (m)
$N$ rotor speed (1/s)
$P$ power (W)
$Po$ the power number ($P/(\rho N^3 D^5)$)
$Q_i$ flowrate through boundary i (kg/s)
$r$ radial coordinate (m)
$r_i$ radius of section ij (m)
$U_r$ ensemble averaged radial velocity (m/s)
$U_z$ ensemble averaged axial velocity (m/s)
$U_\theta$ ensemble averaged tangential velocity (m/s)
$\overline{u_r'}$ rms of fluctuating component of radial velocity (m/s)
$\overline{u_z'}$ rms of fluctuating component of axial velocity (m/s)
$\overline{u_\theta'}$ rms of fluctuating component of tangential velocity (m/s)
Z axial coordinate (m)

*Greek letters*

$\rho$ density (kg/m$^3$)
$\theta$ tangential coordinate (°)

## APPENDIX B

$r$ radial coordinate (m)
$U_r$ radial velocity (m/s)
$U_z$ axial velocity (m/s)
$U_\theta$ tangential velocity (m/s)
$Z$ axial coordinate (m)

*Greek letters*

$\theta$ tangential coordinate (°)

**APPENDIX C**

| | |
|---|---|
| $r$ | radial coordinate (m) |
| $Q_3$ | flowrate through boundary 3 of the control volume (kg/s) |
| $U_{rad}$ | radial velocity (m/s) |
| $U_{rji}$ | radial velocity of section ji (m/s) |
| $Z$ | axial coordinate (m) |

*Greek letters*

| | |
|---|---|
| $\Delta y$ | section width in boundary 3 of slotted or square hole head (m) |
| $\Delta z$ | section height in boundary 3 of slotted or square hole head (m) |
| $\theta$ | tangential coordinate ($^o$) |

# REFERENCES


1. Adrian, R. J. and Yao, C. S., 1987. "Power spectra of fluid velocities measured by laser Doppler velocimetry", *Exp. Fluids*, **5**: 17-28.

2. Albrecht, H. E., Bprys, M., Bamaschke, N., and Tropea, C., 2003. "*Laser Doppler and Phase Doppler Measurement Techniques"*, Springer-Verlag, Berlin, Germany.

3. Alcamo, R., Micale, G., Grisafi, F., Brucato, A., and Ciofalo, M., 2005. "Large-eddy simulation of turbulent flow in an unbaffled stirred tank driven by a Rushton turbine", *Chem. Eng. Sci.*, **60**: 2303-2316.

4. Atiemo-Obeng, V. A. and Calabrese, R. V., 2004. "Rotor-stator mixing devices" in *Handbook of Industrial Mixing: Science and Practice*, Paul, E. L., Atiemo-Obeng, V. A., and Kresta, S. M., eds., John Wiley & Sons, Inc., Hoboken, New Jersey, USA.

5. Aubin, J., Fletcher, D. F., and Xuereb, C., 2004. "Modeling turbulent flow in stirred tanks with CFD: the influence of the modeling approach, turbulence model and numerical scheme", *Exp. Therm. Fluid Sci.*, **28**: 431-445.

6. Bakker, A. and Oshinowo, L. M., 2004. "Modelling of Turbulence in Stirred Vessels Using Large Eddy Simulation", *Chem. Eng. Res. Des.*, **82**: 1169-1178.

7. Baldyga, Jerzy and Bourne, John R., 1999. "*Turbulent Mixing and Chemical Reactions"*, John Wiley & Sons, Chichester, UK.

8. Baldyga, Jerzy, Kowalski, A. J., Cooke, M., and Jasinsky, M., 2007. "Investigation of micromixing in the rotar-stator mixer", in *Proc.XIX Conference of Chemical and Processing Engineering*, Rzeszow, Poland.

9. Baldyga, J., Makowski, L., Orciuch, W., Sauter, C., and Schuchmann, H. P., 2008. "Deagglomeration processes in high-shear devices", *Chem. Eng. Res. Des.*, **86**: 1369-1381.

10. Bourne, J. R. and Studer, M., 1992. "Fast reactions in rotor-stator mixers of different size", *Chem. Eng. Process.*, **31**: 285-296.

11. Brucato, A., Ciofalo, M., Grisafi, F., and Micale, G., 1998. "Numerical prediction of flow fields in baffled stirred vessels: a comparison of alternative modelling approaches", *Chem. Eng. Sci.*, **53**: 3653-3684.

12. Bruun, H. H., 1995. "*Hot-Wire Anemometry: Principles and Signal Analysis"*, Oxford University Press, Oxford, UK.

13. Bujalski, J. M., Jaworski, Z., Bujalski, W., and Nienow, A. W., 2002. "The influence of the addition position of a tracer on CFD simulated mixing times in a vessel agitated by a Rushton turbine", *Trans. IChemE. , Part A*, **80**: 824-831.

14. Calabrese, R. V., Francis, M. K., Kevala, K. R., Mishra, V. P., Padron, G. A., and Phongikaroon, S., 2002. "Fluid dynamics and emulsification in high shear mixers", in *3rd World Congress on Emulsions*, Lyon, France.

15. Cooke, M., Naughton, J., and Kowalski, A. J., 2008. "A simple measurement method for determining the constants for the prediction of turbulent power in a Silverson MS 150/250 in-line rotor-stator mixer", in *6th International Symposium on Mixing Industrial Process Industries (ISMIP VI)*, Niagara on the Lake, Niagara Falls, Ontario, Canada.

16. Davidson, P. A., 2004. "*Turbulence : An Introduction for Scientists and Engineers"*, Oxford University Press, Oxford, UK.

17. Davies, J. T., 1987. "A physical interpretation of drop sizes in homogenizers and agitated tanks, including the dispersion of viscous oils", *Chem. Eng. Sci.*, **42**: 1671-1676.

18. Deglon, D. A. and Meyer, C. J., 2006. "CFD modelling of stirred tanks: Numerical considerations", *Minerals Engineering*, **19**: 1059-1068.

19. Delafosse, A., Line, A., Morchain, J., and Guiraud, P., 2008. "LES and URANS simulations of hydrodynamics in mixing tank: comparison to PIV experiments", *Chem. Eng. Res. Des.*, **86**: 1322-1330.

20. Derksen, J., 2001. "Assessment of Large Eddy Simulations for agitated flows", *Chem. Eng. Res. Des.*, **79**: 824-830.

21. Derksen, J. J. and van den Akker, H. E. A., 1999. "Large eddy simulation on flow driven by a Rushton turbine", *AIChE J.*, **45**: 209-221.

22. Doucet, L., Ascanio, G., and Tanguy, P. A., 2005. "Hydrodynamics characterization of rotor-stator mixer with viscous fluids", *Chem. Eng. Res. Des.*, **83**: 1186-1195.

23. Durst, F., Melling, A., and Whitelaw, J. H., 1981. "*Principles and Practice of Laser-Doppler Anemometry"*, Academic Press, London, UK.

24. Dyster, K. N., Koutsakos, E., Jaworski, Z., and Nienow, A. W., 1993. "An LDA study of the radial discharge velocities generated by a Rushton turbine: Newtonian fluids, Re > 5", *Trans. IChemE. , Part A*, **71**: 11-23.

25. Eggels, J. G. M. and Sommers, J. A., 1995. "Numerical simulation of free convective flow using the lattice-Boltzman scheme", *Int. J. Heat and Fluid Flow*, **16**: 357-364.

26. Escudie, R. and Line, A., 2003. "Experimental analysis of hydrodynamics in a radially agitated tank", *AIChE J.*, **49**: 585-603.

27. Fields, J.,1999."Styrene ethylene buthylene styrene (SEBS) copolymer rubber modified asphalt mixture",US Patent No. 5973037.

28. Fluent Inc., 2004. *Fluent's User Guide, Release 6.2.*

29. Gabriele, A., Nienow, A. W., and Simmons, M. J. H., 2009. "Use of angle resolved PIV to estimate local specific energy dissipation rates for up- and down-pumping pitched blade agitators in a stirred tank", *Chem. Eng. Sci.*, **64**: 126-143.

30. George, W. K., Beuther, P. D., and Shabbir, A., 1989. "Polynomial calibrations for hot wires in thermally varying flows", *Exp. Thermal and Fluid Sci.*, **2**: 230-235.

31. Germano, M., Piomelli, U., Moin, P., and Cabot, W. H., 1991. "A dynamic subgrid-scale eddy viscosity model", *Phys. Fluid A*, **3**: 1760-1765.

32. Gimbun, J., Rielly, C. D., and Nagy, Z. K., 2009. "Modelling of mass transfer in gas-liquid stirred tanks agitated by Rushton turbine and CD-6 impeller: A scale-up study", *Chem. Eng. Res. Des.*, **87**: 437-451.

33. Hallback, M., Johansson, A. V., and Burden, A. D., 1995. "The basic of turbulence modelling" in *Turbulence and Transition Modelling*, Hallback, M., Henningson, D. S., Johansson, A. V., and Alfredsson, P. H., eds., Kluwer Academic Publisher, Dordrecht, The Netherlands.

34. Hemrajani, R. R. and Tatterson, G. B., 2004. "Mechanically stirred vessels" in *Handbook of Industrial Mixing: Science and Practice*, Paul, E. L., Atiemo-Obeng, V. A., and Kresta, S. M., eds., John Wiley & Sons, Inc., Hoboken, New Jersey, USA.

35. Hinze, J. O., 1976. "*Turbulence"*, McGraw-Hill, New York, USA.

36. http://www.chemineer.com (last accessed on 8 June 2009).

37. http://www.dantecdynamics.com (last accessed on 8 June 2009).

38. http://www.highshearmixers.com (last accessed on 8 June 2009).

39. http://www.ikausa.com (last accessed on 8 June 2009).

40. http://www.nambis.de (last accessed on 8 June 2009).

41. http://www.silverson.com (last accessed on 8 June 2009).

42. http://www.ystral.de (last accessed on 8 June 2009).

43. http://www.vmi.fr (last accessed on 8 June 2009).

44. http://www.siefer-trigonal.de (last accessed on 8 June 2009).

45. Jaworski, Z., Bujalski, W., Otomo, N., and Nienow, A. W., 2000. "CFD study of homogenization with dual Rushton turbines--comparison with experimental results: Part I: Initial studies", *Chem. Eng. Res. Des.*, **78**: 327-333.

46. Jaworski, Z., Wyszynski, M. L., Dyster, K. N., Mishra, V. P., and Nienow, A. W., 1998. "A study of an up- and down-pumping wide blade hydrofoid impeller: Part II. CFD analysis", *Can. J. Chem. Eng.*, **76**: 866-876.

47. Jaworski, Z. and Zakrzewska, B., 2002. "Modelling of the Turbulent Wall Jet Generated by a Pitched Blade Turbine Impeller: The Effect of Turbulence Model", *Chem. Eng. Res. Des.*, **80**: 846-854.

48. Karbstein, H. and Schubert, H., 1995. "Developments in the continuous mechanical production of oil-in-water macro-emulsions", *Chem. Eng. Process.*, **34**: 205-211.

49. Khopkar, A. R., Fradette, L., and Tanguy, P. A., 2007. "Hydrodynamics of a Dual Shaft Mixer with Newtonian and Non-Newtonian Fluids", *Chem. Eng. Res. Des.*, **85**: 863-871.

50. Kim, W. W. and Menon, S., 1997. "Application of the localized dynamic subgrid-scale model to turbulen wall-bounded flows", Technical Report AIAA-97-0210, American Institute of Aeronautics and Astronautics, 35th Aerospace Science Meeting, Reno.

51. King, L. V., 1914. "On the convection of heat from small cylinders in a stream of fluid: Determination of the convection constants of small platinum wires with applications to hot-wire anemometry", *Phil. Trans. Roy. Soc.*, **A214**: 373-432.

52. Kowalski, A. J., 2009. "An expression for the power consumption of in-line rotor-stator devices", *Chem. Eng. Process.*, **48**: 581-585.

53. Launder, B. E., Reece, G. J., and Rodi, W., 1975. "Progress in the development of a Reynolds-stress turbulence closure", *J. Fluid Mech.*, **68**: 537-566.

54. Lavezzo, V., Verzicco, R., and Soldati, A., 2009. "Ekman pumping and intermittent particle resuspension in a stirred tank reactor", *Chem. Eng. Res. Des.*, **87**: 557-564.

55. Li, Y. H., Wu, C. Y., Chen, B. C., and Chao, Y. C., 2008. "Measurements of a high-luminosity flame structure by a shuttered PIV system", *Meas. Sci. Technol.*, **19**: 1-11.

56. Lilly, D. K., 1966. "On the application of the eddy viscosity concept in the inertial subrange of turbulence", NCAR Manuscript 123.

57. Loebbert, G. and Sharangpani, A. S. G., 2000. "Pigment dispersions" in *Kirk-Othmer Encyclopedia of Chemical Technology (online version)*, John Wiley & Sons, Inc.

58. Marshall, E. M. and Bakker, A., 2004. "Computational fluid mixing" in *Handbook of Industrial Mixing: Science and Practice*, Paul, E. L., Atiemo-Obeng, V. A., and Kresta, S. M., eds., John Wiley & Sons, Inc., Hoboken, New Jersey, USA.

59. Mathieu, J. and Scott, J., 2000. "*An Introduction to Turbulent Flow"*, Cambridge University Press, Cambridge, UK.

60. Mayo, Jr. W. T., Shay, M. T., and Riter, S., 1974. "Digital estimation of turbulence power spectra from burst counter LDV data", in *Proc. of the 2nd Intl. Workshop on Laser Velocimetry*, Purdue University, West Lafayette, Indiana.

61. Mishra, V. P., Dyster, K. N., Jaworski, Z., Nienow, A. W., and McKemmie, J., 1998. "A study of an up and a down pumping wide blade hydrofoil impeller: Part1. LDA measurement", *Can. J. Chem. Eng.*, **76**: 577-588.

62. Moin, P. and Kim, J., 1982. "Numerical investigation of turbulent channel flow", *J. Fluid Mech.*, 341-377.

63. Montante, G., Lee, K. C., Brucato, A., and Yianneskis, M., 2001. "Numerical simulations of the dependency of flow pattern on impeller clearance in stirred vessels", *Chem. Eng. Sci.*, **56**: 3751-3770.

64. Murthy, B. N. and Joshi, J. B., 2008. "Assessment of standard k-ε, RSM and LES turbulence models in a baffled stirred vessel agitated by various impeller designs", *Chem. Eng. Sci.*, **63**: 5468-5495.

65. Myers, J. K., Reeder, M. F., and Ryan, D., 2001. "Power draw of a high-shear homogenizer", *Can. J. Chem. Eng.*, **79**: 94-99.

66. Myers, K. J., Reeder, M. F., Ryan, D., and Daly, G., 1999. "Get a fix on high-shear mixing", *Chem. Eng. Prog.*, **95**: 33-42.

67. Ng, K., Fentiman, N. J., Lee, K. C., and Yianneskis, M., 1998. "Assessment of Sliding Mesh CFD Predictions and LDA Measurements of the Flow in a Tank Stirred by a Rushton Impeller", *Chem. Eng. Res. Des.*, **76**: 737-747.

68. Ng, K. and Yianneskis, M., 2000. "Observations on the distribution of energy dissipation in stirred vessels", *Chem. Eng. Res. Des.*, **78**: 334-341.

69. Nobach, H., 2002. "Local time estimation for the slotted correlation function of randomly sampled LDA data", *Exp. Fluids*, **32**: 337-345.

70. Pacek, A. W., Baker, M., and Utomo, A. T., 2007a. "Characterisation of flow pattern in a rotor stator high shear mixer", in *6th European Congress on Chemical Engineering*, Gani, R. and Johansen, K. D., eds., Copenhagen, Denmark.

71. Pacek, A. W., Ding, P., and Utomo, A. T., 2007b. "Effect of energy density, pH and temperature on de-aggregation in nano-particles/water suspensions in high shear mixer", *Pow. Tech.*, **173**: 203-210.

72. Padron, G. A., 2001. "Measurement and Comparison of Power Draw in Batch Rotor-Stator Mixers", M.Sc. Thesis, University of Maryland, College Park, MD, USA.

73. Papadopoulos, G. and Arik, E. B., 2004. "Experimental Method, Part B: Fundamental Flow Measurement" in *Handbook of Industrial Mixing: Science and Practice*, Paul, E. L., Atiemo-Obeng, V., and Kresta, S. M., eds., John Wiley & Sons, Inc., Hoboken, New Jersey, USA.

74. Patankar, S. V., 1980. "*Numerical Heat Transfer and Fluid Flow*", Hemisphere Publishing Corp., USA.

75. Roussinova, V., Kresta, S. M., and Weetman, R., 2003. "Low frequency macroinstabilities in a stirred tank: scale-up and prediction based on large eddy simulations", *Chem. Eng. Sci.*, **58**: 2297-2311.

76. Schubert, H., 1997. "Advances in the mechanical production of food emulsions" in *Engineering and Food*, Jowitt, R., eds., Sheffield Academic Press, Sheffield, UK.

77. Shekkar, S. and Jayanti, S., 2002. "CFD study of power and mixing time for paddle mixing in unbaffled vessels", *Chem. Eng. Res. Des.*, **80**: 482-498.

78. Sheng, J., Meng, H., and Fox, R. O., 2000. "A large eddy PIV method for turbulence dissipation rate estimation", *Chem. Eng. Sci.*, **55**: 4423-4434.

79. Speziale, C. G., Sarkar, S., and Gatski, T. B., 1991. "Modelling the pressure strain correlation of turbulence", *J. Fluid Mech.*, **227**: 245-272.

80. Tummers, M. J. and Passchier, D. M., 1996. "Spectral estimation using a variable window and the slotting technique with local normalization", *Meas. Sci. Technol.*, **7**: 1541-1546.

81. TSI, Inc., (1988). *Instruction Manual Model 550 Signal Processor*.

82. TSI, Inc., (1988). *Instruction Manual Model 9800 Series Fiberoptic Probes*.

83. Utomo, A. T., Baker, M., and Pacek, A. W., 2008. "Flow pattern, periodicity and energy dissipation in a batch rotor-stator mixer", *Chem. Eng. Res. Des.*, **86**: 1397-1409.

84. Versteeg, H. K. and Malalasekera, W., 1995. "*Introduction to Computational Fluid Dynamics : The Finite Volume Method"*, Longman Scientific & Technical, Harlow, Essex, UK.

85. Walstra, P., 1993. "Principles of emulsion formation", *Chem. Eng. Sci.*, **48**: 333-349.

86. Wu, H. and Patterson, G. K., 1989. "Laser-Doppler measurements of turbulent-flow parameters in a stirred mixer", *Chem. Eng. Sci.*, **44**: 2207-2221.

87. Xie, L., Rielly, C. D., Eagles, W., and Ozcan-Taskin, G., 2007. "Dispersion of Nano-Particle Clusters Using Mixed Flow and High Shear Impellers in Stirred Tanks", *Chem. Eng. Res. Des.*, **85**: 676-684.

88. Yeoh, S. L., Papadakis, G., and Yianneskis, M., 2004. "Numerical simulation of turbulent flow characteristics in a stirred vessel using the LES and RANS approaches with the sliding/deforming mesh methodology", *Chem. Eng. Res. Des.*, **82**: 834-848.

89. Yoshizawa, A., 1991. "Eddy-viscosity-type subgrid-scale model with a variable Smagorinsky coefficient and its relationship with one-equation model in large eddy simulation", *Phys. Fluid A*, **3**: 2007-2009.

90. Zhou, G. and Kresta, S. M., 1996. "Distribution of energy between convective and turbulent flow for three frequently used impellers", *Trans. IChemE. , Part A*, **74**: 379-389.

# APPENDIX A

# MEASUREMENT OF JET VELOCITY, REPRODUCIBILITY OF LDA DATA AND MASS AND ENERGY BALANCES IN DISINTEGRATING HEAD

## *A.1. Measurement of jet velocity profile*

To measure radial velocity profile of the jet emerging from the disintegrating head, the LDA measurement volume was placed in a fixed position, i.e. in point x in *Fig. A.1* which is located at z = -0.8 mm (the horizontal centerline of the hole), r = 16.2 mm (0.3 mm off the stator) and $\theta = 0$.

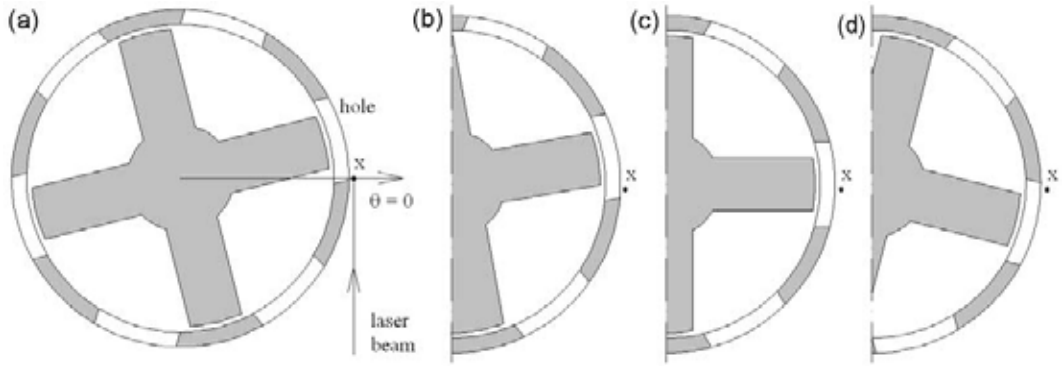


***Fig. A.1.*** *Measurement of jet radial velocity in disintegrating head. (a) The LDA measurement volume is placed in a fixed position, point x (z = -0.8mm, r = 16.2 mm, $\theta = 0$), and the mixing head is turned in the clockwise direction, i.e. from (a) – (d) every 2.34°.*

The mixing head was then turned in clockwise direction every 2.34° from the leading edge to the trailing edge. To do this, a measuring tape (with an accuracy of 1 mm) was attached to the location cup above the mixing head where the coupling between the rotor shaft and motor took place. The perimeter of this cup was 307 mm and therefore 1 mm of the measuring tape was equal to 1.17°. To

measure the tangential velocity profile, the measurement volume was placed at the same radial and axial positions, but at $\theta = -90^o$ (point y in *Fig. A.2*).

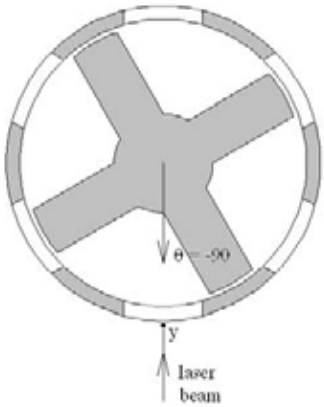


***Fig. A.2.*** *Measurement of jet tangential velocity in disintegrating head. LDA measurement volume is placed at point y (z = -0.8mm, r = 16.2 mm, $\theta = -90^o$) and then the mixing head is turned in the clockwise direction every 2.34$^o$.*

## *A.2. Reproducibility of LDA data*

To assess the reproducibility of LDA data, radial velocity was measured twice in two different experiments. Measurements were taken along line AB in *Fig. A.3(a)* and the number of data collected in each point was about 20,000. *Fig. A.3(b)* and *Fig. A.4* show good reproducibility of LDA measurements for both mean and fluctuating component of radial velocities respectively. The standard deviations of the differences between two measurements are 2.5% and 1.3% of the rotor tip velocity for mean velocity and fluctuating component respectively. The radial velocity along line AB is the radial velocity of the jet emerging from the stator hole and therefore the flow in this region not only has high velocity but also high velocity gradient and high turbulence intensity. These results also show that the technique used to measure jet radial velocity as described in section A.1. gives reproducible results.

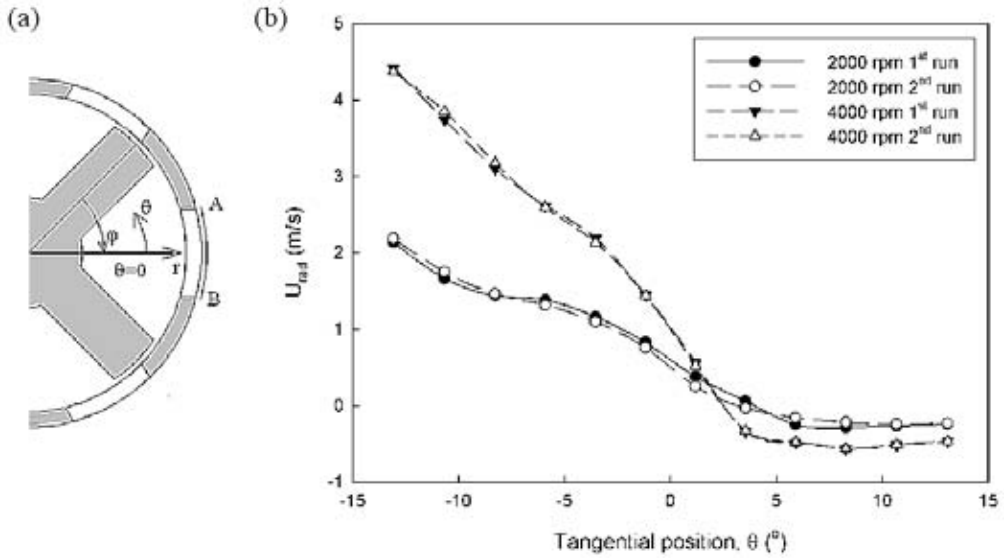


***Fig. A.3.*** *(a) Position of line AB where measurements were carried out and (b) comparison of mean (ensemble average) radial velocity along line AB between measurements.*

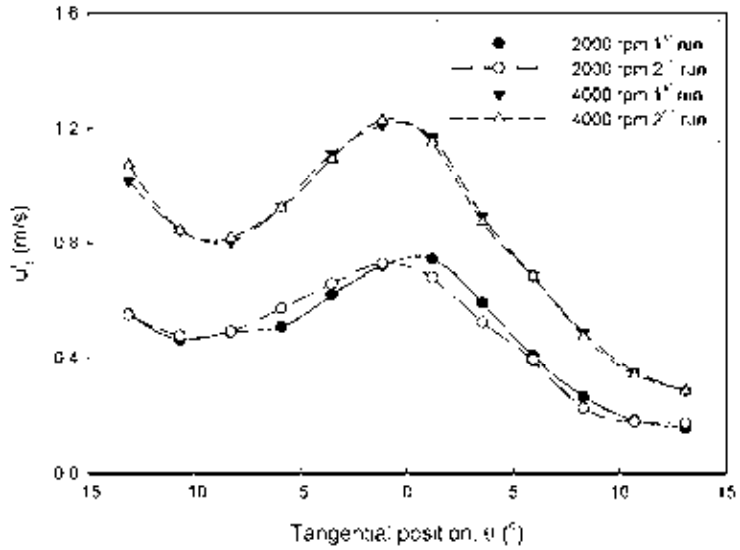


***Fig. A.4.*** *Comparison of fluctuating component (root mean square) of radial velocity along line AB (Fig. A.3(a)) between measurements.*

## *A.3. Mass balance*

The consistency of LDA measurements were also assessed by using mass balance. The control volume used to carry out mass and energy balances in disintegrating head is shown in *Fig. A.5*. The control volume has three boundaries,

i.e. boundary 1 is a horizontal circle, located 4 mm below the stator lower plate, boundary 2 is a vertical cylindrical surface located between boundary 1 and stator lower plate and boundary 3 is six vertical circles coinciding with the holes. Due to the presence of the pin heads on the stator lower plate (see Chapter I, *Fig. 1.3*) boundaries 1 and 2 are not axially symmetrical. Therefore, each boundary was discretised into grid cells and the velocity component perpendicular to each boundary is measured in the center of each cell.

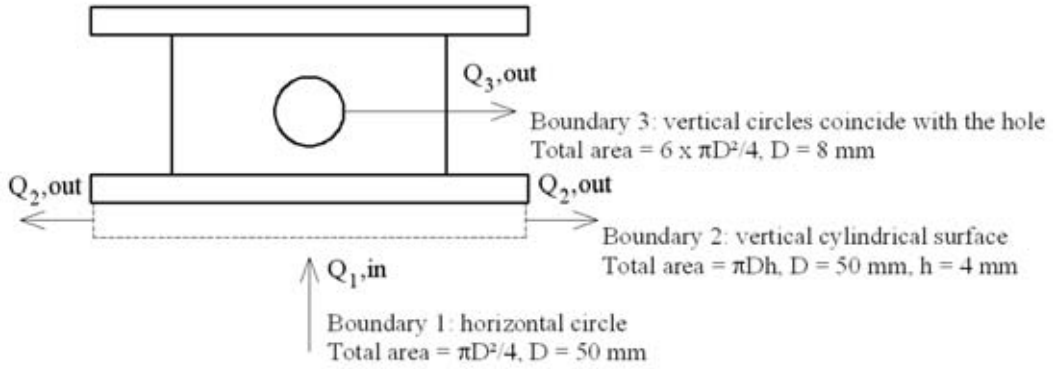


***Fig. A.5.*** *Control volume around mixing head for mass and energy balances and the definition of each boundary. Mass or energy flux into the control volume is taken as positive.*

Boundary 1 was discretised into two different modes. In the first mode (*Fig. A.6(a)*), boundary 1 was discretised into small squares and the axial velocity component was measured in the center of each square. The flowrate through boundary 1, $Q_1$, was calculated as

$$Q_1 = \rho \sum_{i=1}^{n} \sum_{j=1}^{m} A_{ji} U_{z\,ji} \qquad \textbf{A-1}$$

where $A_{ji}$ is the area of cell $ji$ and $U_{zji}$ is the axial velocity component through cell $ji$. For mass balance where only axial velocity component is required to calculate the flowrate, this method is simple and straight forward, however, it is very

difficult to measure tangential and radial velocity components required for energy balance.

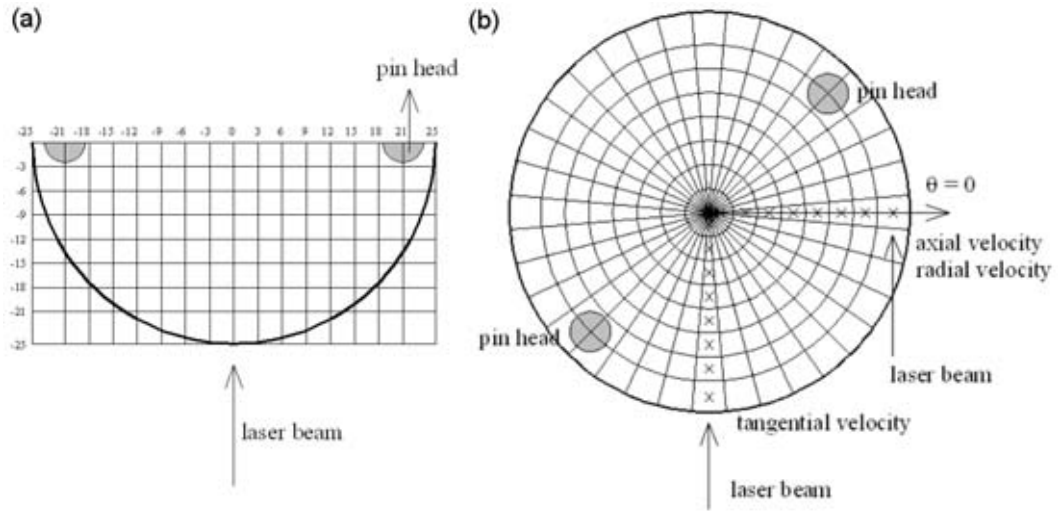


***Fig. A.6.*** *(a)Discretisation of boundary 1 into small squares (3 x 3 mm), (b) discretisation of boundary 1 into small circular cells (8 cells in the radial direction and 36 cells in the tangential direction). The "x" indicates the measurement positions.*

In the second mode (*Fig. A.6(b)*), boundary 1 was discretised into small circular sections. The axial and radial velocity components were measured at θ = 0, while the tangential velocity component was measured at θ = -90°. To take the effect of pin heads into account, the mixing head was rotated every 10° over 360°, similar to the technique used to measure jet radial velocity profile. The axial and radial velocity components were measured at θ = 0 while the tangential velocity component was measured at θ = 90°. The flowrate through boundary 1, $Q_1$, was calculated as

$$Q_1 = \rho \sum_{i=1}^{n} \sum_{j=1}^{m} \frac{\pi (r_i^2 - r_{i-1}^2)}{m} U_{z\,ji} = \rho \sum_{i=1}^{n} \left( \pi (r_i^2 - r_{i-1}^2) \times \frac{1}{m} \sum_{j=1}^{m} U_{z\,ji} \right) = \rho \pi \sum_{i=1}^{n} (r_i^2 - r_{i-1}^2) U_{ziave} \quad \textbf{A-2}$$

where $n$ and $m$ are the number of discretised elements in the radial and tangential directions respectively and $U_{ziave}$ is the average of axial velocity at radius $r_i$ over 360°.

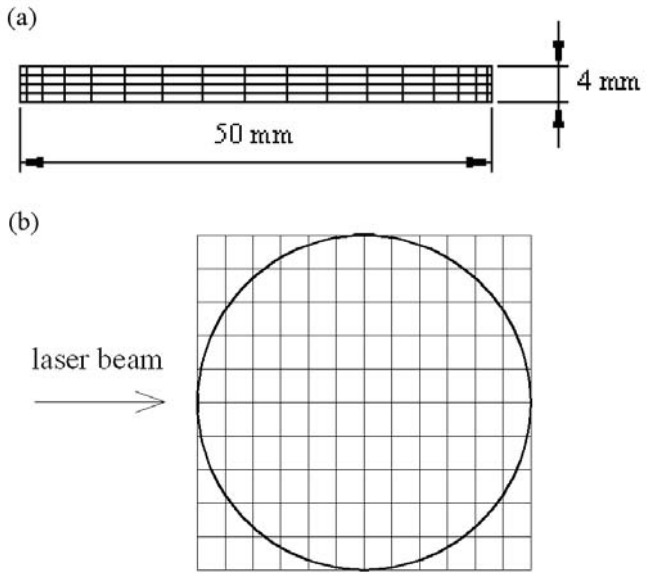


***Fig. A.7.*** *(a) Boundary 2 is discretised into 4 sections in the axial direction and also 36 sections in the tangential direction; (b) boundary 3 is discretised into small squares (0.67 x 0.8 mm).*

The discretisation of boundary 2 is shown in *Fig. A.7(a)*. The radial and axial velocity components were measured at θ = 0 while the tangential velocity component was measured at θ = -90° similar to that in boundary 1 (*Fig. A.7(b)*). The mixing head was also turned every 10° to take the effect of pin head into account. The flowrate through boundary 2, $Q_2$, was calculated as

$$Q_2 = \rho \sum_{i=1}^{n} \sum_{j=1}^{m} \frac{\pi D h}{m} U_{r\,ji} = \rho \pi D h \sum_{i=1}^{n} \left( \frac{1}{m} \sum_{j=1}^{m} U_{r\,ji} \right) = \rho \pi D h \sum_{i=1}^{n} U_{r\,iave} \qquad \textbf{A-3}$$

where $D$ is the diameter of the boundary 2, $h$ is the height of each segment and $U_{riave}$ is the average radial velocity in segment $i$ over 360°.

Boundary 3 was discretised into small squares as shown in *Fig. A.7(b)*. The radial velocity was measured with the same technique as shown in *Fig. A.1* but at different axial positions. The flowrate through boundary 3, $Q_3$, was calculated as

$$Q_3 = \rho \sum_{i=1}^{n} \sum_{j=1}^{m} A_{ji} U_{r\,ji} \qquad \textbf{A-4}$$

where $A_{ji}$ is the area of each segment and $U_{r\,ji}$ is the radial velocity in each segment. The $A_{ji}$ was calculated based on flat surface which is slightly smaller (less than 1%) than the area based on cylindrical surface.

The mass balance was calculated at 2000 and 4000 rpm and the results are summarized in *Table A.1*. The flowrate through boundary 1 at 2000 rpm first run was calculated by using eq. A-1, while those at 2000 rpm second run and at 4000 rpm were calculated using eq. A-2. The difference between inflow and outflow does not exceed 5%, which is a typical error band for a mass balance calculation based on LDA data (Wu and Patterson, 1989, Zhou and Kresta, 1996). The difference of flowrate through each boundary between first and second runs at 2000 rpm is also less than 5%.

***Table A.1.*** *The summary of mass balance.*

| | **2000 rpm 1st run** | **2000 rpm 2nd run** | **4000 rpm** |
|---|---|---|---|
| **Boundary 1** | 0.270 kg/s [(a)] | 0.259 kg/s [(b)] | 0.600 kg/s |
| **Boundary 2** | -0.110 kg/s | -0.108 kg/s | -0.250 kg/s |
| **Boundary 3** | -0.158 kg/s | -0.162 kg/s | -0.320 kg/s |
| **Difference (%)** | 0.005 kg/s (1.9 %) | -0.011 kg/s (4.1 %) | -0.030 kg/s (5%) |

## A.4. Energy balance

The amount of energy dissipated inside the control volume, $E_{diss}$, was calculated from the energy balance. In a stirred tank, the energy balance is usually calculated based on kinetic energy term only ignoring the pressure and potential energy terms (Wu and Patterson, 1989;Zhou and Kresta, 1996). Hence, the energy balance can be written as follows

$$E_{diss} = \sum E_{in} - \sum E_{out} = E_{rotor} + E_{K1} + E_{K2} + E_{K3} \qquad \textbf{A-5}$$

where $E_{rotor}$ is the energy transferred to the fluid by rotor and $E_{K1}$, $E_{K2}$ and $E_{K3}$ are the total kinetic energy fluxes through boundary 1,2 and 3 respectively. According to Padron (2001), the power delivered by the rotor in the rotor-stator mixer can be calculated by using the same formula as the power transferred by the impeller in the stirred tank. Hence

$$E_{rotor} = Po\rho N^{3} D^{5} \qquad \textbf{A-6}$$

where $Po$ is the rotor power number which is equal to 1.7 for the disintegrating head (Padron, 2001).

According to Wu and Patterson (1989), the kinetic energy fluxes in the axial ($KE_z$) and radial ($KE_r$) directions are

$$KE_z = \frac{\rho}{2} U_z (U_z^{\,2} + U_r^{\,2} + U_\theta^{\,2} + 3\overline{u_z'}^{\,2} + \overline{u_r'}^{\,2} + \overline{u_\theta'}^{\,2})\, dA \qquad \textbf{A-7}$$

$$KE_r = \frac{\rho}{2} U_r (U_z^{\,2} + U_r^{\,2} + U_\theta^{\,2} + \overline{u_z'}^{\,2} + 3\overline{u_r'}^{\,2} + \overline{u_\theta'}^{\,2})\, dA \qquad \textbf{A-8}$$

where $\Delta A$ is the discretised area. Hence, the kinetic energy flux through boundary 1 – 3 ($E_{K1} - E_{K3}$) can be calculated as follows

$$E_{K1} = \frac{\rho}{2}\sum_{i=1}^{n}\sum_{j=1}^{m}\frac{\pi(r_i^2 - r_{i-1}^2)}{m}KE_{z\,ji} = \frac{\rho\pi}{2}\sum_{i=1}^{n}(r_i^2 - r_{i-1}^2)KE_{ziave} \qquad \textbf{A-9}$$

$$E_{K2} = \frac{\rho}{2}\sum_{i=1}^{n}\sum_{j=1}^{m}\frac{\pi Dh}{m}KE_{r\,ji} = \frac{\rho\pi Dh}{2}\sum_{i=1}^{n}KE_{riave} \qquad \textbf{A-10}$$

$$E_{K3} = \frac{\rho}{2}\sum_{i=1}^{n}\sum_{j=1}^{m}A_{ij}KE_{r\,ji} \qquad \textbf{A-11}$$

where $KE_{ziave}$ and $KE_{riave}$ in *eq. A-9* and *eq. A-10* are the average $KE_z$ at radius $r_i$ over 360$^o$ (*Fig. A.6 (b)*) and the average $KE_r$ at segment $i$ over 360$^o$ (*Fig. A.7(a)*) respectively.

The energy balance was calculated at 2000 and 4000 rpm and the results are summarized in *Table A.2*. The energy balance indicates that about 70% of energy dissipated inside the control volume and the amount of energy dissipated scales with $N^3$.

***Table A.2.*** *Energy balance around the rotor stator head at 2000 and 4000 RPM*

| | **2000 RPM** | **4000 RPM** |
|---|---|---|
| $E_{rotor}$ | 1.123 W | 8.98 W |
| $E_{K1}$ | 0.063 W | 0.713 W |
| $E_{K2}$ | -0.015 W | -0.188 W |
| $E_{K3}$ | -0.383 W | -3.029 W |
| $E_{diss}$ | 0.787 W | 6.479 W |
| % energy dissipated/energy input | 70.16 % | 72.15 % |
| Average energy dissipation/unit mass ($\bar{\varepsilon}$) in the conrol volume | 48.9 $m^2/s^3$ | 402.2 $m^2/s^3$ |

# APPENDIX B

## EFFECT OF TURBULENCE MODEL ON THE ACCURACY OF CFD PREDICTION

Two turbulence models were investigated, i.e. standard k-ε model and Reynolds stress model (RSM). The simulations were carried out at 2000 rpm with unrefined geometry (see Chapter IV, *Fig. 4*). In each simulation, one rotor rotation was divided into 30 time steps and the results were analyzed after 20 rotor rotations. The standard k-ε model was run with enhanced wall treatment, second order QUICK differencing scheme for spatial discretization and second order implicit time advancing scheme. The RSM was run with standard wall function, first order upwind differencing scheme and first order implicit time advancing scheme. Higher order discretization scheme made RSM unstable probably due to highly stretched cells in the gap region. In both turbulence models, the pressure and momentum equations were coupled using SIMPLE algorithm.

The comparisons between the two turbulence models are shown in *Fig. B.1* - *Fig. B.4*. In general, the predictions of standard k-ε models are practically the same as those of RSM although RSM requires larger computational resources. In each time step, 20 – 25 iterations were required by standard k-ε model to make the solution to converge with residuals below $10^{-3}$, corresponding to real time about 13 minutes. For RSM, more than 40 iterations per time step were required

corresponding to real time of 35 minutes. Therefore, only standard k-ε model is used in this work.

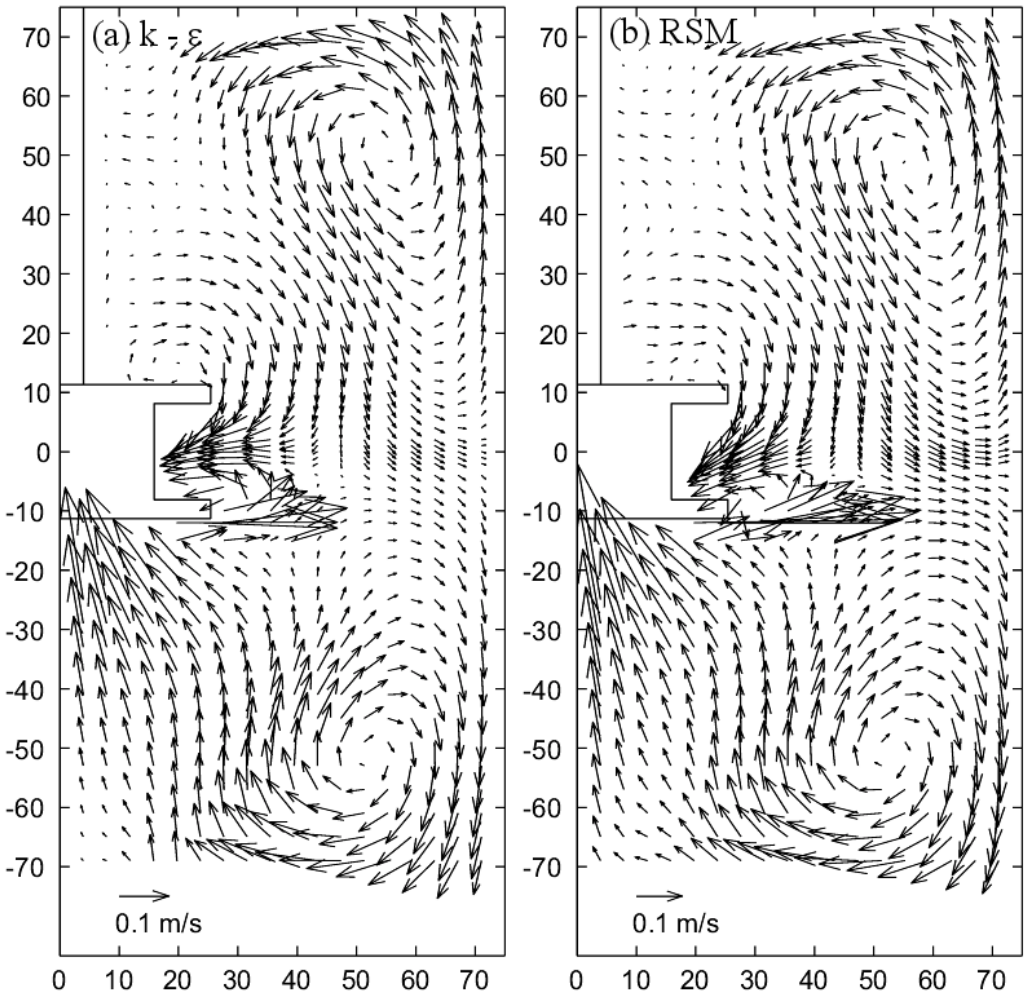


***Fig. B.1.*** *Bulk flow pattern in the axial-radial plane predicted by (a) standard k-ε model and (b) RSM.*

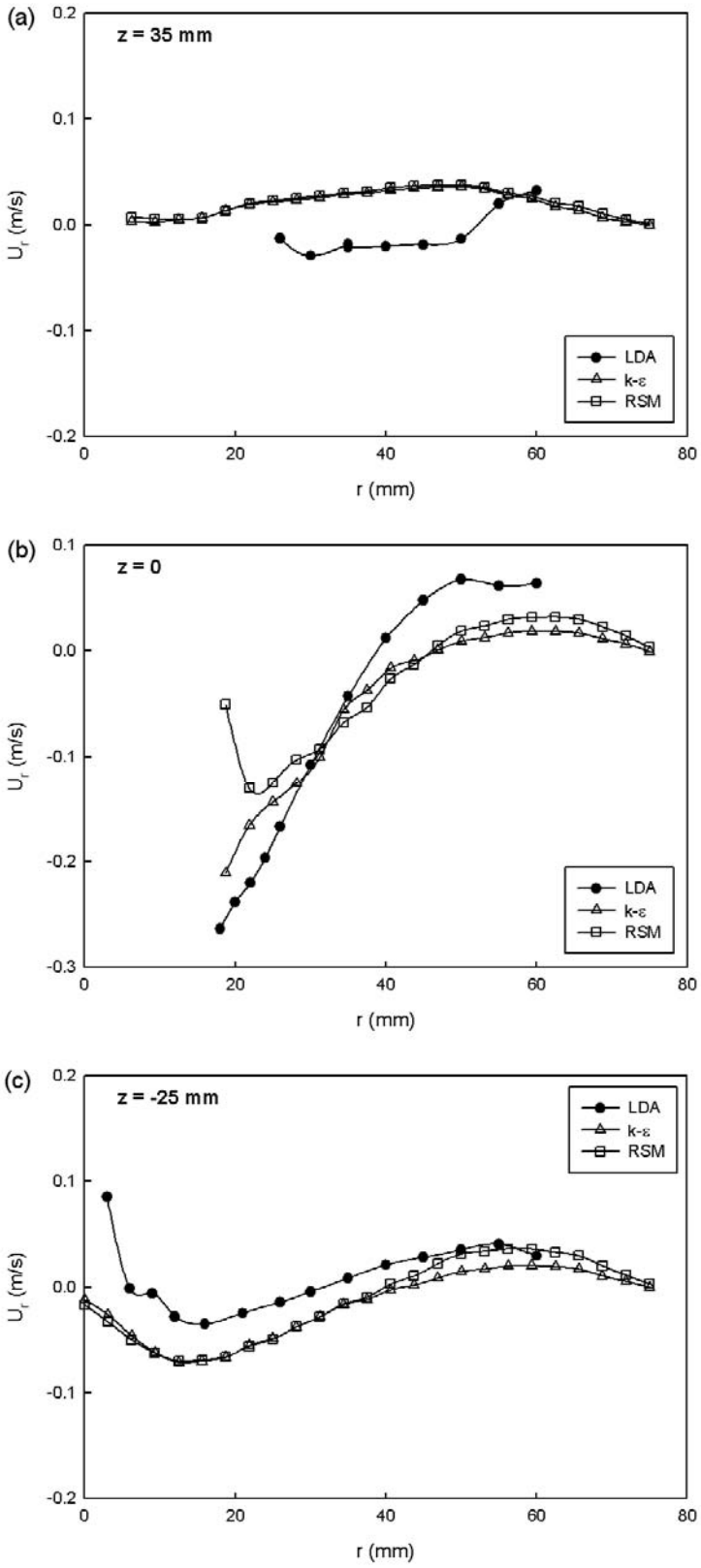


***Fig. B.2.*** *Quantitative comparison of radial velocity between standard k-ε and RSM at various axial positions: (a) z = 35 mm, (b) z = 0 and (c) z = -25 mm.*

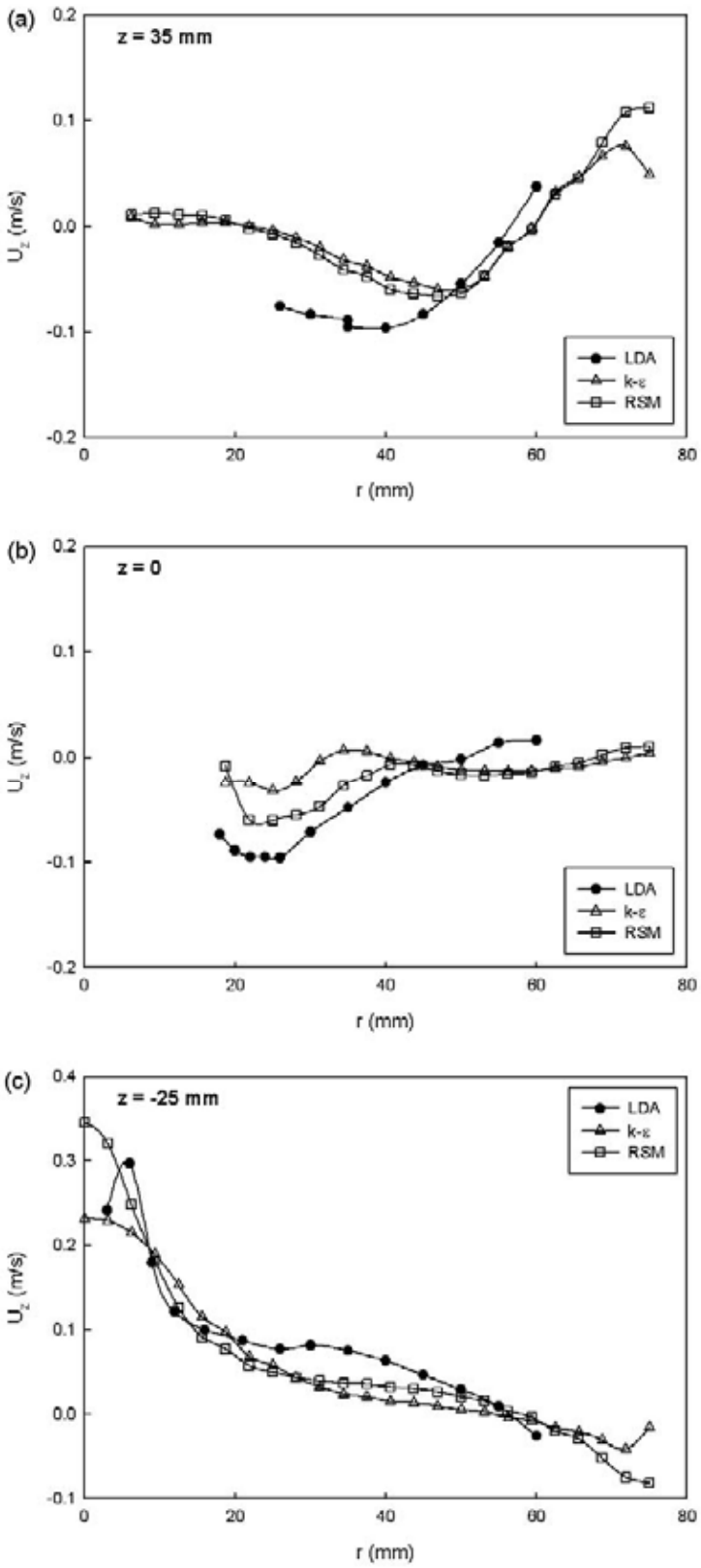


***Fig. B.3.*** *Quantitative comparison of axial velocity between standard k-ε and RSM at various axial positions: (a) z = 35 mm, (b) z = 0 and (c) z = -25 mm.*

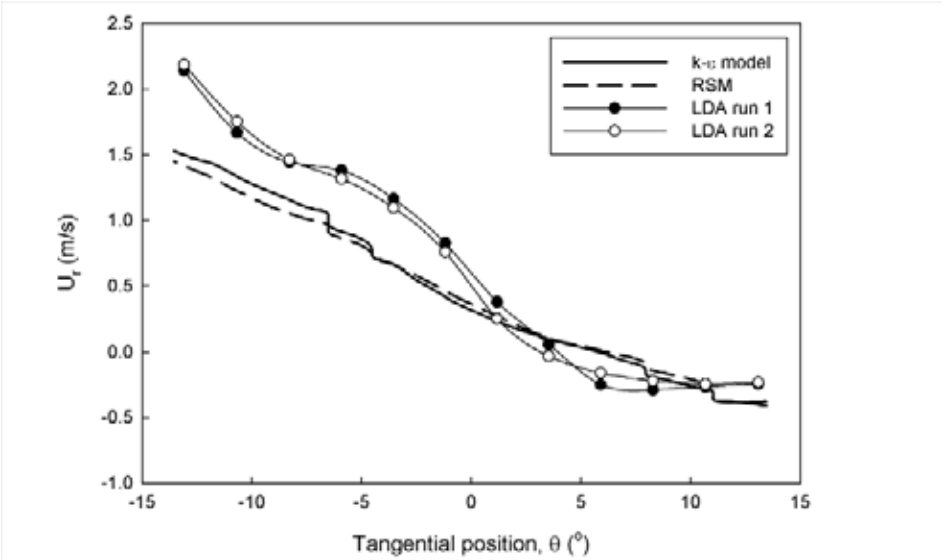


***Fig. B.4.*** *Comparison of time averaged radial velocity along line AB (Fig. A.3 (b)) predicted by standard k-ε model and RSM at 2000 rpm.*

# APPENDIX C

## MASS BALANCE OF SLOTTED AND SQUARE HOLE HEADS AND VALIDATION OF CFD SIMULATIONS

The objectives of this appendix are to validate CFD predictions (flowrates and jet radial velocities) of slotted head (SH) and square hole head (QH) against LDA measurements and to explain why the predicted power number of SH was 20% lower than the experimental value, while those of disintegrating head (DH) and QH were only 10% lower (see Chapter V, *Table 2*). The LDA measurements were carried out at 2000 rpm instead of 4000 rpm due to a problem in LDA filter to read the data at 4000 rpm. Therefore, the CFD simulations were also carried out at 2000 rpm.

The discrepancy between predicted and measured power numbers of SH could be due to discretization scheme (QUICK or second order upwind), grid resolution in the gap and holes or discrepancy between CFD model and real object (see Chapter V). Therefore, in this chapter, two different discretization schemes, QUICK and second order upwind, are compared. A new CFD model of SH with 12 cells across the hole instead of 8 and 8 cells in the gap instead of 5 (see Chapter V, *Fig. 3*) was also employed to investigate the effect of grid resolution. This new CFD model of SH consisted of about 1.3 millions cells inside the mixing head and about 1.2 million cells in the rest of the tank.

## C.1. Mass balance

The mass balances of SH and QH were calculated by using the same control volume as that of the disintegrating head (see *Fig. A.5*). However, in this case, the flowrate going into the mixing head (i.e. the sum of flowrates through boundaries 1 and 2) and flowrate going out of the mixing head (i.e. the flowrate trough stator holes or boundary 3) were calculated separately due to the difficulty to calculate the flowrate through narrow holes (boundary 3).

The flowrates through boundaries 1 and 2 of SH and QH were calculated by using *eq. A-1* and *A-3* respectively. The results from three standard mixing heads are compared in *Table C.1*. QH has the highest pumping capacity since it has the largest opening area, while DH (disintegrating head) and SH have practically the same pumping capacity since the opening area only differs by 10%. However, the amount of liquid flowing toward the mixing head (flowrate trough boundary 1), is the highest in DH which is in agreement with experimental observation and CFD prediction that DH generates the strongest bulk circulation. But most of this liquid exits through boundary 2 instead of going into the mixing head due to limited pumping capacity of DH. For SH and QH, only small amounts of fluid exits through boundary 2 and most of fluid flowing through boundary 1 goes into the mixing head.

***Table C.1.*** *Flowrate through boundaries 1 & 2 and net flowrate going into the mixing heads at 2000 rpm calculated from LDA data.*

| Stator | Opening area ($mm^2$) | Flowrate through Boundary 1 (kg/s) | Flowrate through Boundary 2 (kg/s) | Flowrate going into mixing head (kg/s) |
|---|---|---|---|---|
| DH | 301 | 0.265 | -0.109 | 0.156 |
| SH | 276 | 0.189 | -0.036 | 0.153 |
| QH | 574 | 0.205 | -0.002 | 0.203 |

Flowrate going into mixing head is obtained by summing up flowrates through boundaries 1 and 2 (see *Fig. A.5*). Flowrate goes into the control volume is positive. DH is disintegrating head.

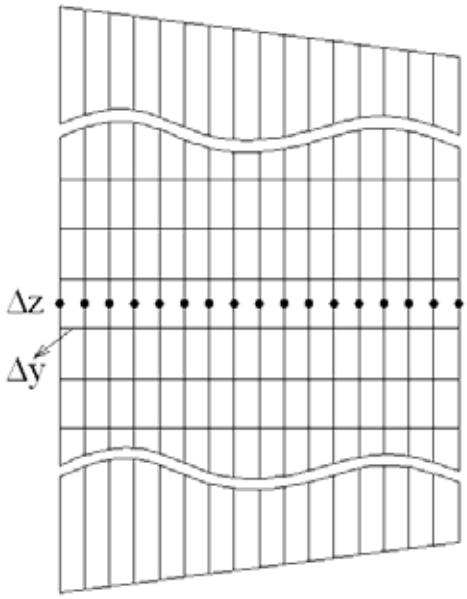


***Fig. C.1.*** *Discretization of hole in the slotted head. The dots indicate where the measurement carried out. The figure is not scaled.*

Boundary 3 in SH was discretised into rectangular cells of dimension 0.1 x 0.8 mm while that in QH was discretised into rectangular cells of dimension 0.1 x 0.4 mm. The velocity was measured at the edges of each section instead of in the middle (*Fig. C.1*). The flowrate is then calculated as

$$Q_3 = \rho \iint U_{rji}\, dydz = \rho \sum_{i=1}^{n} \Delta z \int U_{rji}\, dy \qquad \text{C-1}$$

where $n$ is the number of section in axial direction and $\Delta z$ is the section height. The integral term was calculated by using trapezoidal rule.

The velocity profile of jet emerging from SH is shown in *Fig. C.2(a)*. The velocity profile was measured along a straight line CD located about 0.4 mm off the stator (*Fig. C.2(b)*). However, it is difficult to locate the position of the leading edge precisely, i.e. whether it is at point A, B, C or D, due to small distance between points (0.1 mm). Unfortunately, the flowrate calculated by using eq. C-1

is sensitive to the position of the leading edge as shown in *Table C.2*. By comparing the flowrate going out of the mixing head (boundary 3) with that going into the mixing head, it was found that the closest agreement between the two can be obtained if point C, i.e. the point where the jet radial velocity is the highest, was taken as the leading edge. This approach is also valid for QH as shown in *Table C.3*.

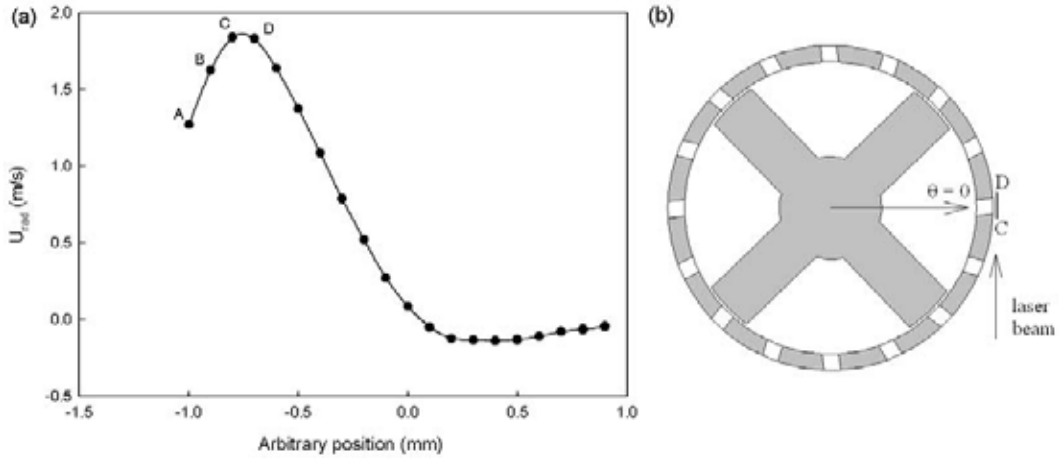


***Fig. C.2.*** *(a) Radial velocity profile of jet emerging from SH (2000 rpm), (b) the velocity profile was measured along line CD about 0.4 mm off the stator. The distance between each point is 0.1 mm.*

***Table C.2.*** *Comparison between flowrate through boundary 3 and flowrate going into the mixing head (SH, 2000 rpm).*

| Starting point | Flowrate through boundary 3 (kg/s) | Net flowrate through boundaries 1 &2 (kg/s) | % imbalance |
|---|---|---|---|
| B | -0.174 | 0.153 | -13.7% |
| C | -0.139 | 0.153 | 9.1% |
| D | -0.103 | 0.153 | 32.7% |

Point C is the point where jet radial velocity is the highest, points B and D are points before and after point B respectively (*Fig. C.2(a)*). Flowrates goes into control volume is taken as positive.

***Table C.3.*** *Comparison between flowrate through boundary 3 and flowrate going into the mixing head (QH, 2000 rpm).*

| Starting point | Flowrate through boundary 3 (kg/s) | Net flowrate through boundaries 1 &2 (kg/s) | % imbalance |
|---|---|---|---|
| B | -0.234 | 0.203 | -15.3% |
| C | -0.197 | 0.203 | 3.0% |
| D | -0.160 | 0.203 | 21.2% |

The definitions of points B, C and D are the same as those in *Table C.2*.

## C.2. Validation of CFD predictions

The new CFD model of SH consisted of about 1.3 millions cells inside the mixing head and about 1.2 million cells in the rest of the tank. This model was run parallelly in a single node (4 cores per node) of the Birmingham Environment for Academic Research (BlueBEAR) cluster using Fluent 12 beta version. QUICK discretization scheme, second order implicit time advancement scheme and enhanced wall treatment were used in this new model. All simulations of SH were run at 2000 rpm with 120 time steps per rotor rotation for 50 rotor rotations since only the flow pattern around the mixing head is of interest. For DH and QH, the simulations were the same as those described in Chapter V but at 2000 rpm. The simulation results are shown in *Table C.4*.

***Table C.4.*** *Predicted flowrates and power numbers of various stator at 2000 rpm*

| Stator | Flowrate (kg/s) | Power number |
|---|---|---|
| DH (QUICK) | 0.135 (-13.5%) | 0.156 (-10.0%) |
| SH (QUICK) | 0.133 (-13.0%) | 0.167 (-20.5%) |
| SH (Second order Upwind) | 0.133 (-13.0%) | 0.167 (-20.5%) |
| SH (gap 8) | 0.133 (-13.0%) | 0.167 (-20.5%) |
| QH (QUICK) | 0.194 (-4.5%) | 0.203 (-11.7%) |

*Table C.4* shows that the predicted flowrate and power number of SH are practically the same regardless of discretisation scheme and grid resolution. This shows that the grids used in Chapter V are fine enough since further grid refinement gives practically the same result. The predicted flowrate of DH and SH at 2000 rpm are about 13% lower than the experimental values, while that of QH is only 4.5% lower than the experimental value. The predicted power numbers of DH and QH at 2000 rpm are about 10% lower than the experimental values, but

that of SH is about 20% lower than the experimental value. This is practically the same as the simulation results at 4000 rpm shown in *Table 2* in Chapter V.

The fact that predicted flowrate of QH only differs by 4.5% from measured one while those of DH and SH differ up to 13% from measured ones may indicate that CFD models of QH have larger total hole area than the actual stator. As shown in *Fig. 6.5* that QH was made from rolled plate. This rolling action deforms the shape of the hole so that the hole width at the outer suface is larger than that at the inner surface. The CFD model of QH, however, was designed by using the hole width at the outer surface since it was not possible to measure the hole width at the inner surface. The CFD model of QH also assumed that the holes were perpendicular so that the total opening area (based on the inner surface) of the CFD model should be larger than that of the actual stator. Based on the error of CFD prediction of flowrates (4.5% for QH and 13% for DH and SH), the total opening area in the CFD model may be 10% larger than that in actual stator.

*Fig. 6.21* shows that predicted power number correlates strongly with the total opening area of the stator. Therefore, if the CFD model of QH had the same total opening area as the actual stator, the discrepancy between predicted and experimental power numbers may be also about 20%. This may indicate that the accuracy of CFD prediction of torque or power number decreases with increasing number of leading edges since the stagnations on those edges may not be properly taken into account by the turbulence model. CFD prediction of flowrate, however, may not be strongly affected by the number of leading edges.

*Fig. C.3(a)* shows the comparison between predicted and measured jet radial velocity profiles of SH along line CD (*Fig. C.3(a)* inset) located 0.4 mm off the stator outer surface, i.e. line CD is located at r = 16.3 mm and z =0. In general the agreement between simulation and measurement is very good except that the simulation underpredicts radial velocity near the leading edge. However, predicted jet radial velocity along line AB (r = 15.9 mm and z = 0) agrees better with the measured one taken along line CD (*Fig. C.3(b)*). *Fig. C.3(a)* and *(b)* also show that there is no effect of cells number in the hole and gap on the accuracy of CFD prediction.

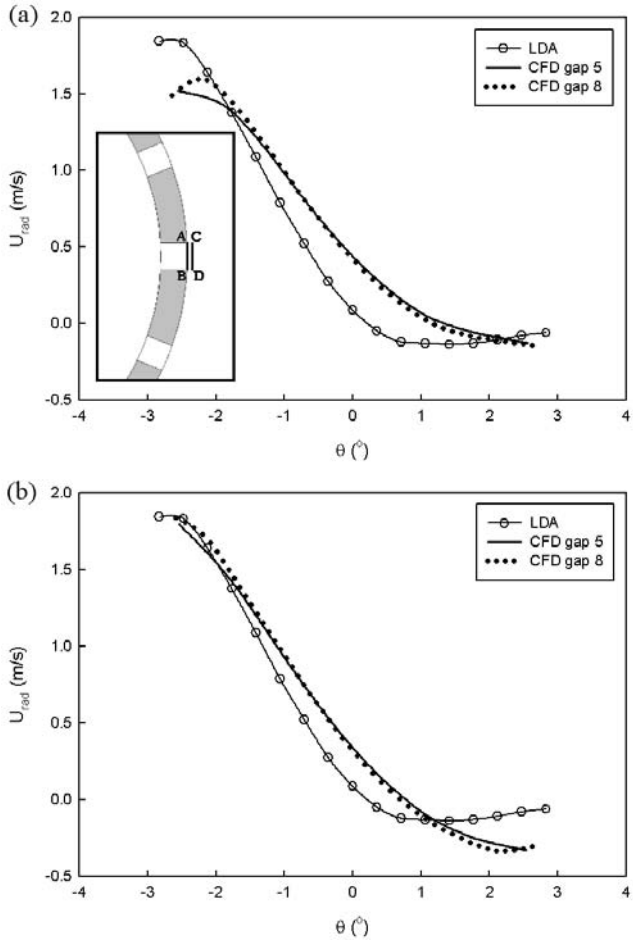


***Fig. C.3.*** *(a) Comparison between predicted and measured jet velocity profiles of SH along line CD (r = 16.3 mm, z = 0, see inset) and (b) comparison between predicted (along line AB located at r = 15.9 mm, z =0, see inset) and measured (along line CD) jet radial velocity profiles of SH.*

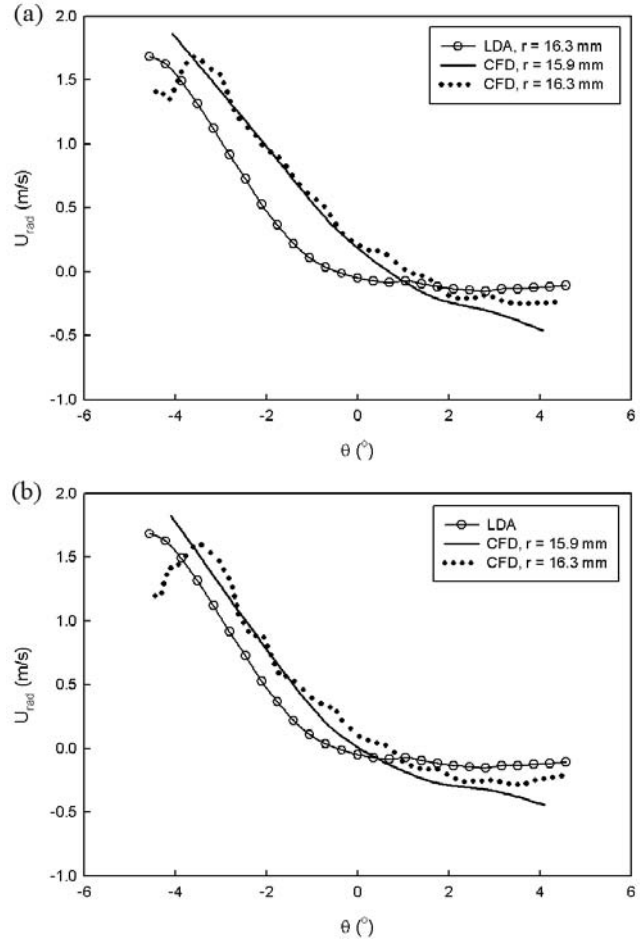


***Fig. C.4.*** *Comparison between predicted and measured jet radial velocity of QH (a) in the middle of the second row (z = 1.2 mm) and (b) in the middle of third row (z = -2.8 mm).*

*Fig. C.4(a)* and *(b)* show the comparison between measured (taken at r = 16.3 mm) and predicted (taken at r = 15.9 mm and r = 16.3 mm) jet radial velocity profiles of QH in the middle of second and third row respectively. The agreements between CFD predictions and LDA measurements are very good although the velocity profiles predicted by CFD are somehow shifted slightly to the right hand side of the measured ones. *Fig. C.3* and *Fig. C.4* show that predicted radial velocities near the leading edge at line r = 16.3 mm are significantly lower (about 20%) than those at line r = 15.9 mm although both lines are only 0.4 mm away from each other. At this point, there is no justification can be made whether the jet

in the proximity of the leading edge has such high velocity gradient or it is just the effect of wall function since this phenomena only occur near the leading edge.

# APPENDIX D

## POSTER PRESENTED IN

## THE EUROPEAN CONGRESS OF CHEMICAL ENGINEERING (ECCE) 6

## COPENHAGEN, 16 – 21 SEPTEMBER 2007

# CHARACTERISATION OF FLOW PATTERN IN A ROTOR STATOR HIGH SHEAR MIXER

Andrzej Pacek*, Michael Baker and Adi Utomo
Chemical Engineering, University of Birmingham, Edgbaston, Birmingham, B15 2TT, UK
*Email: A.W.Pacek@bham.ac.uk

## INTRODUCTION

Batch rotor stator mixers have been widely used in industries to blend miscible liquids of different viscosities, to disperse fine particles into viscous liquid and to make emulsions of immiscible liquids. However, there is practically no literature information on the flow pattern and the energy dissipation rate distribution in such mixers. In this study, a full 3D computational fluid dynamics (CFD) simulation verified by laser Doppler anemometry (LDA) measurements was employed to investigate the bulk flow and the distribution of energy dissipation rate in such mixers. That enables the identification of the most intense mixing/dispersion regions in the batch rotor stator mixer and more accurate scaling-up.

## EXPERIMENTAL

The flow pattern and the energy dissipation rate were studied in a Silverson fitted with a standard disintegrating head (shown in Fig. 1 (b)). The rotor diameter was 28.2 mm and the gap width was 0.175 mm. The rotor speed was varied from 2000 to 4000 rpm ($Re$ = 26,000 – 52,000) with water as working fluid. The simulations were carried out in Fluent 6.2 using k-ε turbulence model.

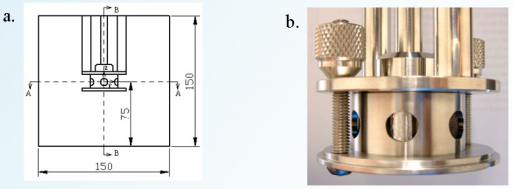


**Fig. 1.** (a) Position of mixing head (dimensions in mm), (b) Silverson mixing head

## RESULTS AND DISCUSSIONS

The flow field in the mixer can be divided into very intensive jet and circulation regions

### FLOW PATTERN IN THE BULK

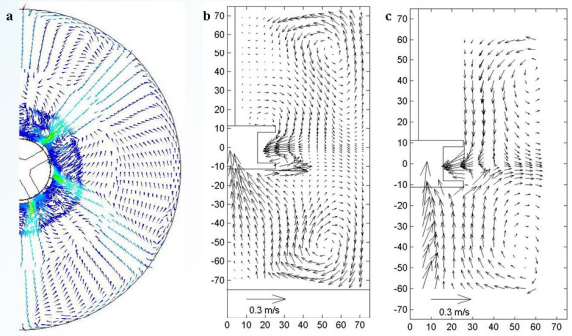


**Fig. 2.** (a) Velocity vectors at section A-A Fig. 1(a) (CFD, plotted by using constant length vectors); (b) velocity vectors at section B-B Fig. 1(a) (CFD); (c) velocity vectors at section B-B Fig. 1(a) (LDA)

### JET VELOCITY PROFILE

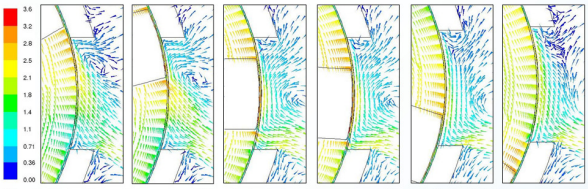

**Fig. 3.** Velocity profiles around the stator hole at various positions of rotor blade.

The maximum velocity of the jet occurs when the blade approaches the leading edge of the hole, just before they overlap (Fig. 3) which means that the jet has a periodic nature. Behind the jet circulation occurs.

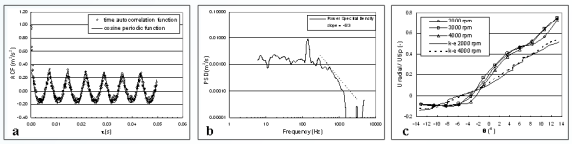


**Fig. 4.** (a) Time autocorrelation (ACF) and (b) power spectral density (PSD) of LDA data taken at the leading edge of the hole (2000 rpm); (c) normalized time-averaged radial velocity of the jet (simulations and measurements).

The time autocorrelation of the LDA data (Fig. 4(a)) also shows periodic nature of the jet. The power spectral density (Fig. 4(b)) indicates that LDA data have a dominant frequency at 137 Hz, practically the same as blade passing frequency which is 133.3 Hz at 2000 rpm.

Measured (LDA) and calculated (CFD) jet radial velocities at various rotor speeds are compared in Fig. 4(c). The maximum velocity occurs at the leading edge of the stator hole (θ = 14°). The graph also shows that the radial velocity of the jet is proportional to the rotor tip speed as the normalized radial velocity falls into one line.

### ENERGY DISSIPATION RATE

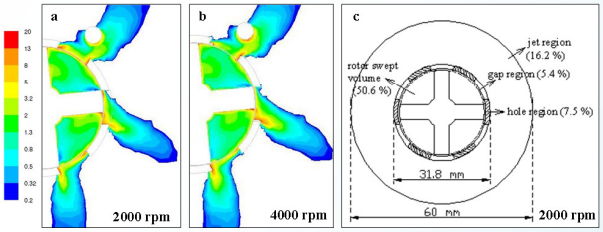


**Fig. 5.** The contours of normalized energy dissipation rate ($\varepsilon/N^3D^2$) at (a) 2000 rpm and (b) 4000 rpm; (c) the distribution of energy dissipation rate (2000 rpm) predicted by CFD.

The contours of normalized energy dissipation rate ($\varepsilon/N^3D^2$) at 2000 and 4000 rpm predicted by CFD show very similar pattern suggesting that ε is proportional to $N^3$ (Fig. 5(a) and (b)).

The simulation also shows that most of energy (50%) is dissipated in the rotor swept volume (Fig. 5(c)). However, the highest energy dissipation rate occurs in the hole when the rotor blade approaches the leading edge (Fig. 6).

The energy balance based on LDA measurements showed that approximately 70% of energy was dissipated inside the mixing head which took into account the energy dissipated in the rotor swept volume, gap and hole regions.

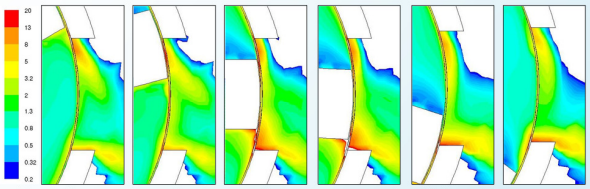

**Fig. 6.** Contour of normalized energy dissipation rate at various blade positions

## CONCLUSIONS

- ❑ The radial velocity of the jet and the energy dissipation rate are proportional to N and $N^3$ respectively.
- ❑ Approximately 70% of the energy is dissipated inside the mixing head.
- ❑ The maximum energy dissipation rate occurs when the rotor blade approaches the leading edge of the stator hole.

## ACKNOWLEDGEMENTS

The financial supports from Unilever Research and Development Port Sunlight (UK), ORSAS and Department of Chemical Engineering, The University of Birmingham are gratefully acknowledged.

UNIVERSITY OF BIRMINGHAM

Unilever